



PHYSIK DEPARTMENT
INSTITUT FÜR EXPERIMENTALPHYSIK E21

OUT-OF-PILE EXAMINATION
OF THE HIGH DENSITY U-Mo/AL
DISPERSION FUEL

NICO WIESCHALLA

Vollständiger Abdruck der von der Fakultät für Physik der Technischen Universität München zur Erlangung des akademischen Grades eines Doktors der Naturwissenschaften genehmigten Dissertation.

Vorsitzender: Univ. - Prof. Dr. M. Kleber

Prüfer der Dissertation: 1. Univ. - Prof. Dr. P. Böni
2. Univ. - Prof. Dr. W. Petry

Die Dissertation wurde am 22. November 2006 bei der Technischen Universität München eingereicht und durch die Fakultät für Physik am 24. November 2006 angenommen.

Circle of life

In 1954, the first nuclear power reactor in the world started operation in Obninsk (Russia). In those first days of the nuclear technology, the fuel used was a well protected secret. It later became public that it was an alloy of uranium and molybdenum in a cladding of stainless steel. Since this kind of fuel had many advantages, other famous reactors of the first “nuclear” generation also used it. For instance the Fermi reactor near Detroit, the Dounreay fast reactor and various pulsed reactors [1].

Nowadays - five decades later - ceramic fuels dominate in nuclear power plants, particularly oxide fuels. For example, as of August 1990, 375 of the 413 power reactors worldwide are fueled with sintered pellets of UO_2 [2]. All oxide fuels together account for 97.9% of the electricity generated by nuclear reactors.

One might assume that the time of the metallic UMo fuel would be over. But in the year 1996 a worldwide rediscovery of the advantages of UMo took place, qualifying it as a very high density fuel for research and test reactors [4]. For this purpose U-Mo powder was dispersed in an aluminum matrix.

In spite of the good performance under in-pile irradiation conditions of the fuel itself, it interacts heavily with the surrounding aluminum matrix. An interdiffusion layer around the UMo particles has been observed after in-pile irradiation. This interdiffusion layer is disadvantageous, because post irradiation examination revealed cracks between the matrix and the interdiffusion layer. These cracks could lead to a break away swelling of the fuel plate. Therefore a detailed knowledge of the properties and build up of the interdiffusion layer is of great interest.

This work shows for the first time how such an interdiffusion layer can be created out of pile - avoiding the disadvantage of neutron activation of the specimen. Furthermore this interaction layer will be characterised, and in conclusion an explanation for the cracks discovered during in-pile irradiation will be provided.

Contents

Introduction	I
List of symbols and abbreviations	V
1 Motivation	1
2 Theory and simulations	9
2.1 Fission and fission fragments	9
2.2 Swift heavy ions in matter	12
2.3 Simulations of U-Mo/Al in-pile irradiation	20
3 Irradiation experiment	27
3.1 Specimen preparation	27
3.2 Heavy ion accelerator and irradiation device	29
3.3 Irradiation conditions	32
4 Post irradiation examination	33
4.1 Optical microscopy	34
4.2 Scanning electron microscopy with EDX	36
4.3 X-ray diffraction measurements	40
5 Discussion	51
5.1 Comparison of heavy ion to in-pile irradiation	51
5.2 Cause and prediction of the interdiffusion layer	57
5.3 Limits of heavy ion irradiation	62
6 Summary	65
7 Outlook	67
7.1 Outlook for heavy ion irradiation	67
7.2 Outlook for a fuel for conversion of the FRM II	67
A Heavy ion bombarded U₃Si	71
B Simulations for the FRM II irradiation test	73
C Maxim data for the U-10wt%Mo/Al specimen	77

Acknowledgment	79
Own publications and patent	81
Bibliography	82

List of symbols and abbreviations

Abbreviation/ Symbol	Explanation	Unit
a	lattice constant	Å
a ₀	Bohr radius	m
A	nuclear number	
AS	shutdown rod (German: Abschaltstab)	
B _e (r,t)	energy deposit in the electron system	J
BOL	begin of life	
c	speed of light	m · s ⁻¹
c _{1,2}	constants	
C	concentration	particle · cm ⁻³
C _m	heat capacity	J · g ⁻¹ · K ⁻¹
C _e	heat capacity of the electrons	J · g ⁻¹ · K ⁻¹
C _l	heat capacity of the lattice	J · g ⁻¹ · K ⁻¹
CEA	Commissariat à l'Energie Atomique	
d	diameter (distribution of)	m
D	diffusion coefficient	m ² · s ⁻¹
D _e	thermal diffusivity	cm ² · s ⁻¹
DESY	Deutsches-Elektronen-Synchrotron	
e	elementary charge	C
E	energy	J or eV
E _B	binding energy	eV
EDX	energy dispersive X-ray analysis	
EFPD	effective full power days	d
E _m	elastic modulus	
E _D	displacement energy	eV
E _F	fission energy	eV
E _{FF}	energy of fission fragments	eV
E _{kin}	kinetic energy	eV
EOL	end of life	
EPR	European Pressurized water Reactor	
E _r	recoil energy	eV
ḟ	fission rate in the fuel particle	fission · s ⁻¹ · cm ⁻³
FD	fission density	cm ⁻³

Abbreviation/ Symbol	Explanation	Unit
FEM	finite element method	
FF	fission fragment	
FFD	fuel fission density	cm^{-3}
FRM II	Forschungsneutronenquelle Heinz Maier-Leibnitz (neutron source)	
FWHM	full width at half maximum	
$g(\Delta T)$	coupling constant (depends on ΔT)	
g_l	lattice factor	
H_M	activation energy of migration	eV
HEU	high enriched uranium	
HQ	hot source (German: Heiße Quelle)	
IBID	ion beam induced plastic deformation	
I	current	A
j	particle flux	$\text{particle} \cdot \text{cm}^{-2} \cdot \text{s}^{-1}$
IDL	interdiffusion layer	
k_B	Boltzmann-constant	$\text{J} \cdot \text{K}^{-1}$
KQ	cold source (German: Kalte Quelle)	
LEU	low enriched uranium	
m	mass	kg
m_{ff}	mass of a fission fragment	kg
MEU	medium enriched uranium	
n	neutron	
n_e	electron density	$\text{e} \cdot \text{cm}^{-3}$
n_l	lattice nuclei density	$\text{nuclei} \cdot \text{cm}^{-3}$
OM	optical microscopy	
P_{th}	thermal power	MW
P_{el}	electrical power	MW
PIE	post irradiation examination	
q	heat production	W
q'	linear heat rate	$\text{W} \cdot \text{cm}^{-1}$
q''	heat flux	$\text{W} \cdot \text{cm}^{-2}$
q_i	mean level of ionisation	
r	radius	m
RERTR	reduced enrichment for research and test reactors	
RRFM	research reactor fuel management	
S_e	electronic stopping power	$\text{MeV} \cdot \text{mm}^{-1}$
S_n	nuclear stopping power	$\text{MeV} \cdot \text{mm}^{-1}$
SEM	scanning electron microscopy	
SHI	swift heavy ion	
t	time	s
T	temperature	K
T_e	temperature of the electrons	K

Abbreviation/ Symbol	Explanation	Unit
THTR	thorium pebble bet reactor (German: Thorium Hoch Temperatur Reaktor)	
T_l	temperature of the lattice	K
TRIM	transport of ions in matter	
TUM	University of Technology Munich (German: Technische Universität München)	
u	mass unit	kg
v	velocity	$\text{m} \cdot \text{s}^{-1}$
V	diameter conversion factor	
V_{acc}	Voltage of the accelerator	V
$V_{pre-acc}$	Voltage of the pre-accelerator	V
V_C	Coulomb-barrier	MeV
VHGR	volumetric heat generation rate	$\text{W} \cdot \text{cm}^{-3}$
x	length	m
y	variable	
XRD	X-ray diffraction	
Z	atomic number	
α	irradiation angle	°
π	mathematical constant	
ϵ_0	dielectric constant	$\text{F} \cdot \text{m}^{-1}$
Φ	flux	$\text{s}^{-1} \cdot \text{cm}^{-2}$
λ	thermal conductivity	$\text{W} \cdot \text{m}^{-1} \cdot \text{K}^{-1}$
λ_e	thermal conductivity (electrons)	$\text{W} \cdot \text{m}^{-1} \cdot \text{K}^{-1}$
λ_l	thermal conductivity (lattice)	$\text{W} \cdot \text{m}^{-1} \cdot \text{K}^{-1}$
ν	average number of neutrons released per fission	
ν_0	vibration frequency	s^{-1}
τ	mean free path length of electrons	m
ϑ	angle (diffraction measurement)	°
ρ	mass density	$\text{kg} \cdot \text{m}^{-3}$
σ_{abs}	microscopic cross section (absorption)	barn = 10^{-24} cm^2
ω_p	plasma frequency	s^{-1}
\bigcirc	average	
Δ	delta	
∇	nabla-operator	

Chapter 1

Motivation

In 2004 the new research reactor “Forschungsneutronenquelle Heinz Maier-Leibnitz (FRM II)” in Garching, Germany, went into operation. The reactor has been designed as a high performance neutron source. This means that on the one hand the reactor provides a thermal neutron flux (unperturbed) as high as $8.0 \cdot 10^{14} \text{ cm}^{-2} \text{ s}^{-1}$ outside of the core, and on the other hand that the total heat production is very low, only 20 MW_{th} . This is achieved by using a single cylindrical fuel element which contains a graded high density fuel with highly enriched uranium (HEU, 93wt% ^{235}U).

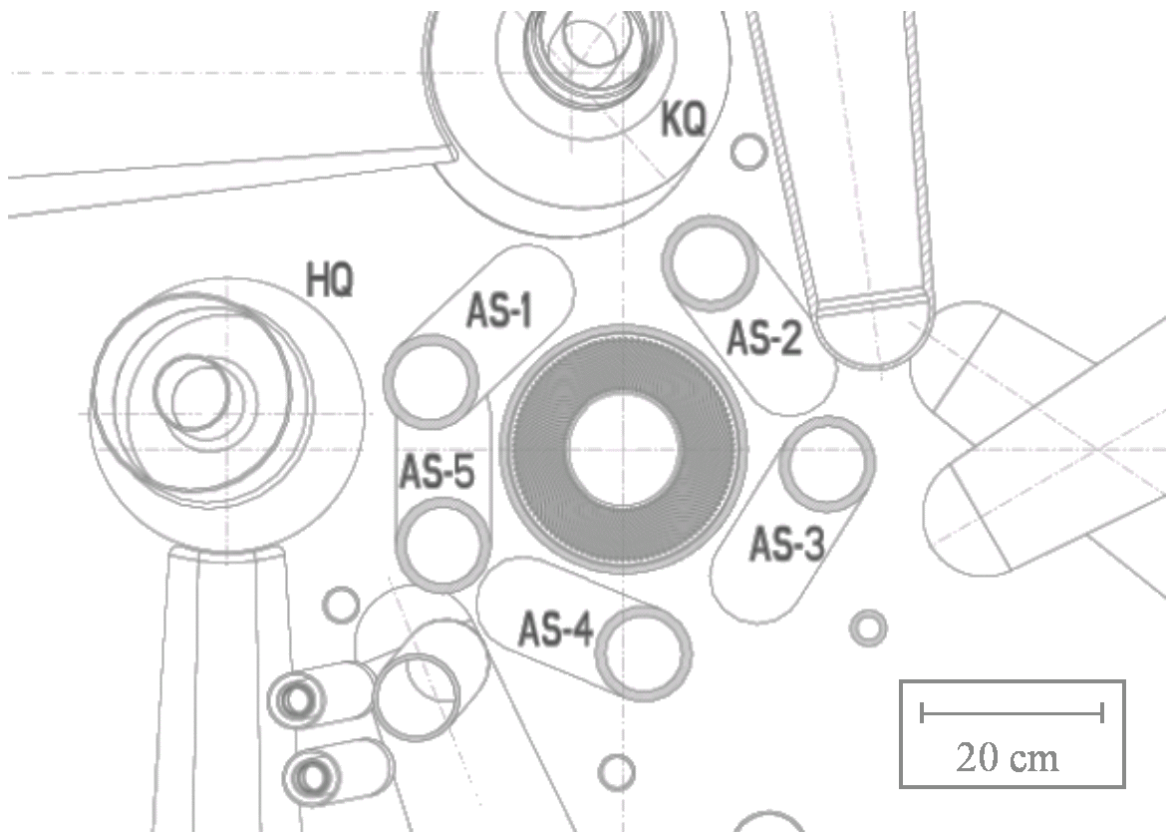


Figure 1.1: Horizontal cut, 30 cm above core midplane, through the inner part of the moderator tank of the FRM II with the fuel element in the central core tube

Table 1.1: Characteristic values of the FRM II fuel element [5], see also Tab. 1.2

fuel element dimensions	
outer radius	12.15 cm
inner radius	5.9 cm
fuel plates (involute shape)	
number	113
width of the plate	1.3 mm
(hereof meat)	(0.6 mm)
uranium density in the meat	
r < 10.5 cm	3.0 gU · cm ⁻³
r > 10.5 cm	1.5 gU · cm ⁻³
width of the cooling channel	
	2.2 mm

Figure 1.1 shows a horizontal cut (30 cm above core midplane) through the fuel element of the FRM II and the inner part of the heavy water tank, which surrounds the fuel element. In the inner space of the fuel element the control rod (not shown) moves, and the five shutdown rods (AS-1 through AS-5) are plotted in their shutdown positions. Further, the cold source (KQ), hot source (HQ), two inclined beam tubes and some of the 10 horizontal beam tubes are shown.

Since the fuel element is cooled by light water and surrounded by a heavy water reflector, a very high power density (\Rightarrow high neutron flux) can be achieved for a cycle length of 52 days, resulting in a very high burn-up of the uranium. The fuel, which satisfies such a high requirement, is a $\text{U}_3\text{Si}_2/\text{Al}$ dispersion fuel, this means that U_3Si_2 particles (fuel) were dispersed in an aluminum matrix¹. This mixture of fuel particles and matrix is denoted as meat. In the end of a cycle, this means after 52 full power days at 20 MW_{th} ($=1040 \text{ MW}_{thd}$) up to $2.1 \cdot 10^{21}$ fission per cm^3 in the meat took place, this value is denoted as the maximum meat fission density (FD).

Furthermore, the meat is sealed in a frame and two cladding layers (in this case: AlFeNi), resulting in a fuel plate². A detailed description of the manufacturing of a

¹Aluminum was chosen as matrix material, because it is a relatively soft material - compared to the fuel. Since fuel plates, which contain the dispersion fuel, are manufactured by rolling, each fuel particle will be embedded in aluminum. This guarantees a good heat removal from the fuel particles (where fission takes place = energy release) into the aluminum matrix, and from the aluminum matrix into the cladding of the fuel plate. Therefore the heat removal from the fuel particle is still guaranteed, even when a fuel particle swells under irradiation. Other advantages of aluminum are the low cross section for neutron capture σ_{abs} , the high thermal conductivity λ and low costs.

²In the meat will also be voids (denoted as as-fabricated porosity). During in-pile irradiation the as-fabricated porosity will disappear because on the one hand voids will be filled up with fission gases and on the other hand the fuel particles expand significantly under irradiation and therefore they consume space.

Table 1.2: Characteristic values of the FRM II fuel element [5], the EPR core [6, 8] and the THTR-300 core [7, 8]

	FRM II	EPR	THTR-300
nominal power P_{th}	20 MW _{th}	4280 MW _{th}	750 MW _{th}
⊙ VHGR in the meat	7 kW·cm ⁻³	310 W·cm ⁻³	6 W·cm ⁻³
fuel inventory	8.1 kg	> 100 t	344 kg
active core height	70 cm	420 cm	≈ 400 cm
fuel type	U ₃ Si ₂ /Al	MOX	UO ₂ +ThO ₂
fuel enrichment in ²³⁵ U	93 wt%	≤ 5 wt%	93 wt%
cycle length	52 days	up to 24 month	up to ∞
max. burn-up	≈ 250 GWd/t	> 60 GWd/t	-
moderator	light and heavy water	light water	graphite
coolant	light water	light water	helium
max. coolant temperature	52 °C	326 °C	750 °C

fuel plate will be presented in section 3.1. A complete fuel element of the FRM II contains 113 fuel plates. These plates have an involute shape and contain two different fuel densities in the meat. Between the fuel plates are coolant channels. Dimensions and characteristic values of the fuel plates and the fuel element of the FRM II are given in Tab. 1.1 and Tab. 1.2.

For classification, these values are compared in Tab. 1.2 with two other types of reactors. These are on the one hand a pressurized water reactor (generation III+, here represented by the European pressurized water reactor (EPR), which is currently under construction in Finland and France - the latest generation of commercial nuclear power plants), and on the other hand with a high-temperature pebble bed prototype reactor (Generation IV, here represented by the THTR-300 (German abbreviation for: Thorium Hoch Temperatur Reaktor - 300 MW_{el}), which was operated in Germany from the year 1985 to 1988). The table shows that compared to the nuclear power plant and the prototype reactor, the FRM II research reactor has:

- a very small nominal power P_{th} , but a much higher volumetric heat generation rate (VHGR) in the meat
- a much lower fuel (uranium) inventory
- a much higher burn-up as referred to heavy metal

- a relative short cycle length
- and much lower operating temperatures

A condition of the final license, which was received in 2003 for operating the FRM II reactor, was that the FRM II should develop a new fuel element with medium enriched uranium (MEU, not more than 50% enrichment in ^{235}U) before the end of the year 2010. Since a redesign of the reactor facility would appear to be unrealistic, the dimension of the fuel element have to be unchanged. Also the new fuel element should lead only to marginal losses in performance and safety. Because the quantity of uranium-235 (fissionable material) has to be at least maintained, the total uranium (^{235}U and ^{238}U) in the meat has to be increased. This means that a very high density fuel is required [9, 10]. Calculations revealed that the FRM II fuel element would require at least 7.75 g uranium (for an enrichment of 50wt% in ^{235}U) per cm^3 in the meat, and taking into account other aspects like the less than optimal power distribution, the minimum density can hardly be below 8.0 g uranium per cm^3 [11, 12].

For this reason, the volume fraction of the fuel particles in the meat has to be increased. This technique is limited to approximately 55 vol% fuel particles in the meat in commercial available processes and considering a good accommodation of the fuel particles, which swell strongly during irradiation, in the aluminum matrix. The drawback of an increase of the volume loading is a strong loss in the thermal conductivity λ of the meat. Fig. 1.2 shows the thermal conductivity of typical Al-dispersion fuels (non-irradiated) versus the volume fraction of fuel particles and voids (as-fabricated porosity). It demonstrates that the different dispersion fuel types have the same tendency. However, the encircled 1 marks the position of the currently used $\text{U}_3\text{Si}_2/\text{Al}$ dispersion fuel (3g uranium per cm^3 in the meat). Assuming that this tendency is also valid for other dispersion fuel types, the encircled 2 would mark the position of the desired fuel for the conversion of the FRM II. This means a loss in thermal conductivity by a factor of seven.

Since in first approximation

$$\Delta T \propto \lambda^{-1} \quad (1.1)$$

assuming unchanged geometry and power distribution, this would lead to undesired high temperatures T in the meat.

Furthermore the uranium density in the fuel particles itself could be increased. Tab. 1.3 lists the uranium compounds with densities greater or equal to that of U_3Si_2 which is currently used. With the exception of U_6Fe and U_6Mn , which were tested in the US-American reduced enrichment for research and test reactors (RERTR) program and shown to be subject to breakaway swelling³ at relatively low burn-ups, and similar

³All nuclear fuels swell strongly under irradiation, one reason for instance is that fission leads to an increase of the number of atoms, and the volume is (in first approximation) proportional to the number of atoms. Therefore the swelling of the fuel is linear to the burn-up. However, some fuels

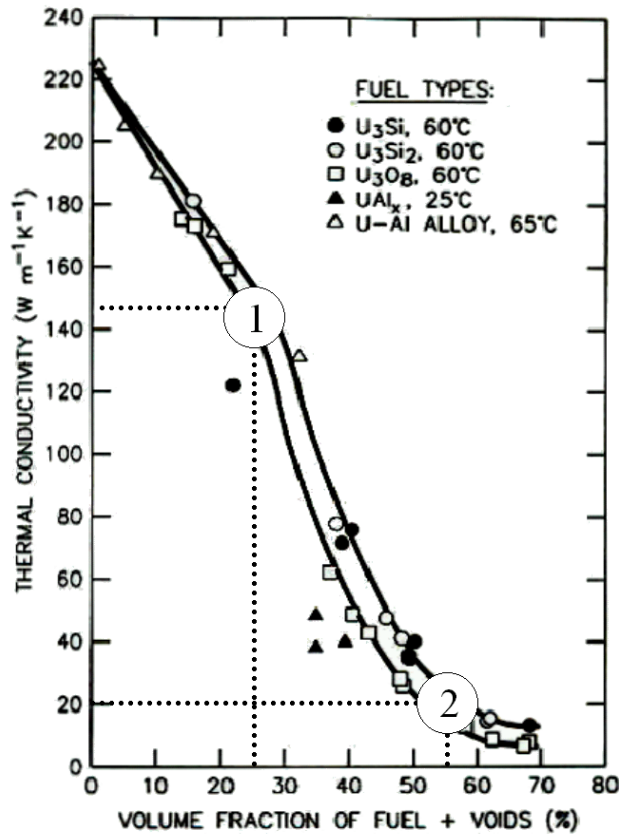


Figure 1.2: Thermal conductivity of typical Al-dispersion fuels (non-irradiated) versus the volume fraction of fuel particles and voids. Position 1 marks the currently used fuel and position 2 marks the position where the desired fuel for the conversion of the FRM II could be [2].

compounds are also expected to exhibit similar swelling properties [14]. None of the remaining compounds meets the density requirements of the FRM II.

The only fuels with sufficiently high uranium densities are pure uranium metal ($\rho(\text{U}) = 19.05 \text{ g per cm}^3$ [59]) and alloys of uranium with small amounts of other metals. Pure uranium is known to be a notoriously poor performer under irradiation, but a series of alloys designed to maintain in a metastable γ -phase have shown good irradiation performance in bulk form under fast reactor conditions [14]. Examples of such alloys are listed in Tab. 1.4, hereby U-Zr-Nb alloys showed a poor performance under annealing and in-pile irradiation under research reactors conditions.

Only the metallic U-Mo alloy in the metastable γ -phase is remaining (see Fig. 1.3). This fuel would allow even a uranium density of around 8.5 gU/cm^3 in the meat at the highest volume loading of 55 vol%. Therefore it is currently under worldwide investigation [14].

Some major research groups, who investigate the U-Mo/Al dispersion fuel, should be mentioned:

swell from a certain burn-up much stronger than expected. This phenomena is named "breakaway swelling".

Table 1.3: Selected uranium-compounds with higher density than that of U_3Si_2 [14]

Compound	Density [g/cm ³]	U-Density [g/cm ³]
U_3Si_2	12.2	11.3
UB_2	12.7	11.6
UCo	15.4	12.3
UC	13.6	13.0
UN	14.3	13.5
U_2Ti	15.1	13.7
U_2Mo	16.6	13.8
U_2Tc	16.8	13.9
U_2Ru	16.9	13.9
U_3Si	15.5	14.6
U_6Co	17.7	17.0
U_6Ni	17.6	16.9
U_6Fe	17.7	17.0
U_6Mn	17.8	17.1

Table 1.4: Selected uranium-alloys with higher density than that of U_3Si_2 [14]

Alloy	Density [g/cm ³]	U-Density [g/cm ³]
U-9wt% Mo (U-19at%Mo)	17.0	15.5
U-5wt% Mo (U-11at%Mo)	17.9	17.0
U-3wt% Zr-9wt% Nb	16.2	14.3
U-4wt% Zr-2wt% Nb	17.3	16.3

- the Reduced Enrichment for Research and Test Reactors - team (RERTR) at Argonne National Laboratory (ANL) and Idaho National Laboratory (INL) - the initiator of the (re-)investigation, USA
- the French-group, that means the Commissariat à l'Énergie Atomique (CEA) and CERCA, France
- A.A. Bochvar All-Russian Scientific Research Institute of Inorganic Materials (VNIINM), Russia
- Korea Atomic Energy Research Institute (KAERI), Korea
- Comision Nacional de Energia Atomica (CNEA), Argentina

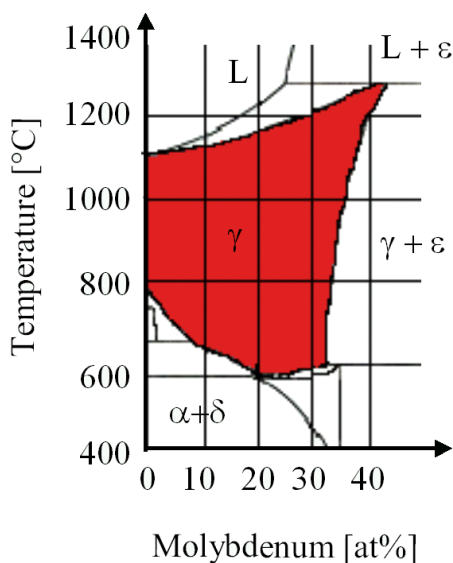


Figure 1.3: Part of the U-Mo phase diagram - only the metastable γ -phase (red) has a stable in-pile irradiation behavior [17]

- and last but not least the group at the Technische Universität Munich (TUM), Germany.

While all of these groups aim at qualifying the U-Mo/Al dispersion fuel, approaches, aims and motivations vary.

It has also to be pointed out that there are two annual conferences where the progress in research reactor fuel development (presently mainly U-Mo/Al dispersion fuel) is discussed. These conferences are the RERTR (every late autumn) and the RRFM (research reactor fuel management - every late spring). Papers presented are available at the appropriate homepage (for RERTR: [4], for RRFM: [16]).

So far most of the U-Mo/Al in-pile irradiation tests have been performed on very small specimen in order to test a variety of specimen. These tests revealed, that the minimum quantity of Mo in the fuel particles should be in the range of 6 wt% (\equiv 13 at%) [15]. Tested specimen with 4 wt% (\equiv 9 at%) Mo tend to break away swelling⁴. But with at least 6wt% Mo in the fuel particles, the obtained results were encouraging in order to qualify the U-Mo/Al dispersion with a very high uranium density.

However, since the year 2003 some concerns have arisen owing to the anomalous swelling (break away swelling) of full size U-7wt%Mo/Al plates during irradiation at elevated neutron flux and heat load. Post irradiation examinations (PIEs) of these plates revealed an Al-rich interdiffusion layer (IDL) building up at the interface between U-Mo particles and the Al-matrix with a thickness of some 10 μm . Further, cracks which are regarded as the reason for the anomalous swelling have been observed between the IDL and the aluminum matrix. Details are reported for instance in [13] or [29].

⁴The reason was the “swelling” of the fuel particles.

Therefore the build-up and the composition of the IDL is of outstanding interest. But because of the strong activation after the reactor irradiation of the specimen only a few types of examinations have been carried out, for example optical microscopy (OM) and scanning electron microscopy (SEM).

Here, for the first time, an approach is shown to generate the IDL by out of pile irradiation with heavy ions⁵, thereby simulating the radiation damage created by fission fragments during reactor irradiation, without the drawback of creating, since it is difficult to handle, strong radioactive specimens. A further advantage of this method is, that it is less time consuming, making this method cost efficient. Some hours of irradiation by heavy ions can be compared with months of in-pile irradiation.

A complete in-pile irradiation program requires even several years, depending on:

- *physical margins*: for instance in order to reach the desired burn-up, the plates must be approximately for one year in the reactor - including reactor breaks
- *technical margins*: for instance a detailed safety analysis has to be done in advance (requires at least some months, in special cases up to years in order to obtain an irradiation license) or, the required decay time of the plates after in-pile irradiation before the plates can be transported to a PIEs facility (usually at least 6 months)
- *availability of the material test reactor, transportation casks etc.*

For instance, the irradiation program for the in-pile irradiation of U-Mo/Al full size plates for the FRM-II started in July 2003 and is now - 3 years later - not completely finished.

First of all this work will provide the required theoretical background in chapter 2. Afterward the preparation of the specimen and irradiation experiments (chapter 3) will be presented. The analysis of the specimen (post irradiation examinations - PIE) is given in chapter 4. In the following discussion these PIEs will be compared with the PIEs of in-pile irradiated specimens (chapter 5). In conclusion a possible explanation of the break away swelling of in-pile irradiated specimen will be offered.

⁵Annealing experiments have shown, that a thermally activated diffusion is also possible, but requires very high temperatures (at least $\approx 340^\circ\text{C}$) and the properties of the interdiffusion layer produced are very different from that obtained after in-pile irradiation, also the risk of decomposition of the metastable γ -phase has to be taken into account. Examples for such annealing tests can be found for instance in [31, 32]

Chapter 2

Theory and simulations

This chapter aims to provide the theoretical background for understanding why U-Mo/Al dispersion fuel has been bombarded with heavy ions in this work. Also some simulations and estimations will be presented, which were required before an irradiation can take place.

First of all, a basic introduction into fission will be given, followed by a detailed description of the interaction between swift heavy ions (representing the high energetic fission fragments) and condensed matter. Also sputtering and activations of the specimen were taken into account under irradiation conditions. Since both can be a concern under heavy ion irradiation. Finally a simulation of U-Mo/Al dispersion fuel behavior during in-pile irradiation will be presented. This simulation will provide a basis for comparison of in-pile and heavy ion irradiation.

2.1 Fission and fission fragments

Since the discovery of fission by thermal neutrons in 1938 by Otto Hahn and Fritz Straßmann, fission can be described very well in a phenomenological way. But a fully accepted theoretical approach seems to be still missing [20]. Anyway, only properties of fission, which are very well known from experiments and are required for this work, will be presented in this chapter.

Every element, that means in this case any atomic nucleus, has a certain cross section for neutron absorption. When such an element absorbs a neutron, the binding energy E_b can be released. For instance this can take place by emitting a γ -quant (an example is $^{113}\text{Cd}(n,\gamma)^{114}\text{Cd}$).

Also every atomic nucleus, which contains protons and neutrons, can be separated into two or even more atomic nuclei, but a minimum amount of energy E_f is required.

Fission can happen, if the released binding energy E_b of a neutron absorbed in an atomic nucleus is greater than the necessary energy to separate the nucleus E_f . Examples are given in Tab. 2.1. The table shows that for ^{233}U , ^{235}U , ^{239}Pu , and ^{241}Pu fission is possible, but not for ^{232}Th , ^{238}U , and ^{240}Pu . The latter nuclei absorb

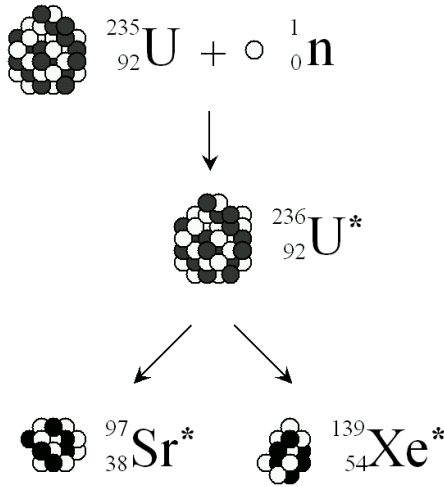
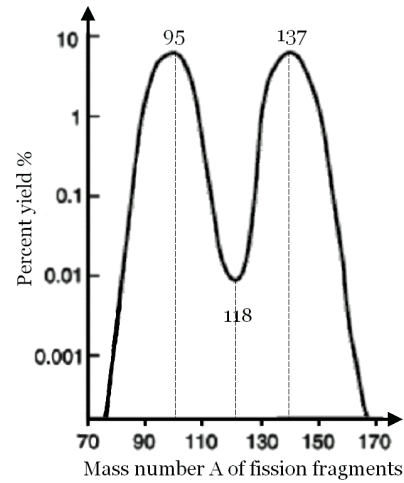


Figure 2.1: Example for fission

Figure 2.2: Fission fragment distribution of thermal fission of ^{235}U [55]

neutrons, and therefore they are a poison in a reactor. Nevertheless, if these nuclei absorb a neutron they become a fissionable nuclei (^{233}Th and ^{239}U will undergo two beta-decays, resulting in ^{233}U and ^{239}Pu , respectively).

If the released binding energy of the neutron is not sufficient, the missing energy for fission can be provided by the kinetic energy of the incoming neutron. However, when the kinetic energy of the neutron is increased, the microscopic cross section for absorption σ_{abs} (\propto probability for an absorption) of a neutron will also be decreased - with the exception of resonances [20].

If ^{235}U undergoes fission, the fission process leads, in the majority of cases, to the production of two fission fragments¹ (see Fig. 2.1), neutrons ($\nu = 0.6$ or even more, $\nu(^{235}\text{U}, \text{thermal}) = 2.52$), beta particles, neutrinos, and gamma radiation [33]. Exact values vary from fission to fission, but average values of the energy release are given in Tab. 2.2. While the two fission fragments have a similar mass for fission with fast neutrons, the two fission fragments for thermal fission have a mass of around $A=95$ and $A=137$ respectively. Fig. 2.2 shows the distribution of fission fragments of a thermal fission of ^{235}U versus the atomic mass number. Since two fission fragments are emit-

¹Also a fission into three parts is possible, but very rare. The probability for two fission fragments and one alpha particle or three similar fission fragments is $3 \cdot 10^{-3}$ and $1 \cdot 10^{-7}$ respectively [20].

Table 2.1: Binding and fission energies of some Th, U, and Pu isotopes

atomic nuclei after neutron capture		^{233}Th	^{234}U	^{236}U	^{239}U	^{240}Pu	^{241}Pu	^{242}Pu
E_f	[MeV]	6.5	6.2	5.7	6.5	5.8	6.2	5.6
E_b	[MeV]	4.8	6.8	6.5	4.8	6.5	5.2	6.3
$E_f - E_b$	[MeV]	1.7	-0.6	-0.8	1.7	-0.7	1.0	-0.7

Reaction products	Energy [MeV]
fission fragments	167 ± 5
neutrons	5
β -particle	8 ± 1.5
γ -radiation (prompt from fission)	6 ± 1
γ -radiation (from fission fragments)	6 ± 1
neutrinos	12 ± 2.5
total	204

Table 2.2: Energy of the reaction products of thermal fission of ^{235}U [21]

ted, the diagram is calibrated to 200% [20]. These two fission fragments (FF) carry approximately 80% of the total fission energy in the form of kinetic energy E_{ff-tot} . Owing to the conservation of momentum and the different weights ($m_{ff1,2}$: mass of fission fragment 1 and 2) of the two fragments, they receive different energies:

$$E_{ff1} = E_{ff-tot} \cdot \frac{m_{ff2}}{m_{ff2} + m_{ff1}} \quad (2.1)$$

Hereby E_{ff1} is the kinetic energy of fission fragment 1. That means the lighter one obtains on average ≈ 98 MeV and the heavier one gets ≈ 68 MeV, which corresponds to a velocity in the order of 10^7 m \cdot s $^{-1}$. Initially, fission fragments are ionized strongly (10..20), excited and have an excess of neutrons. All fission products are inherently unstable and therefore radioactive. As mentioned above, they emit γ -, β -, neutrino- and neutron-radiation [20, 33]. In spite of the importance of this kind of radiation - for instance for sustaining the chain reaction in nuclear power plants or shielding concerns - it will be not further highlighted, because their contribution to radiation damage directly in a nuclear fuel during operation is weak compared to the contribution of the fission fragments. Outside of the fuel or within spent fuel the situation is different.

2.2 Swift heavy ions in matter

Usually defects caused by swift heavy ions in condensed matter are studied at a very low temperature in order to avoid heal-up of the defects. Also a low density of defects is sufficient or even desired for examination [2].

These laboratory conditions are not comparable with nuclear fuel during irradiation in a reactor, where the radiation damage appears at a comparatively high temperature (for instance some hundred degrees Celsius in a nuclear power plant) and the density of defects is in some cases close to the atomic density. Nevertheless, a classical description of radiation damage seems to be applicable and will be shortly outlined.

2.2.1 Types of energy loss

When a swift particle, denoted as projectile, enters condensed matter, also denoted as target, it loses kinetic energy and is finally stopped, more precisely: thermalized. This means that the projectile will become the temperature of the surrounding atoms, or the projectile will be captured by a target atom.

The stopping power dE/dx depends on the particle itself and the target material and can be separated into three different terms [3]:

$$\frac{dE}{dx} = \frac{dE}{dx}\Big|_d + \frac{dE}{dx}\Big|_e + \frac{dE}{dx}\Big|_n \quad (2.2)$$

- $dE/dx|_d$ describes the energy loss per unit of penetration caused by elastic collisions between the interacting partners, i.e. the projectile transfers a recoil energy E_r to a lattice atom of the target. If E_r exceeds a material-dependent threshold energy, the creation of displacement E_D or a vacancy-interstitial, a so called Frenkel defect, is possible - index d for displacement.
- $dE/dx|_e$ characterises inelastic interactions between the projectile and the electrons of the target and occurs only for charged particles (projectile or recoil atoms). The electronic loss can lead to excitation, ionization, transfer or exchange of electrons in the target - index e for electronic losses.
- $dE/dx|_n$ specifies the inelastic collisions between the projectile and the nuclei of the target - index n for nuclear reactions.

While the deposited energy depends on the kinetic energy of the projectile for the first and second items, the last item is different. For instance a cold neutron ($E_{kin} \approx 3.5$ meV) could activate the nuclear reaction $^{10}\text{B}(n,\alpha)^7\text{Li}^*$, which releases 2.49 MeV [23]. Since this work regards exclusively charged particles as projectiles at an energy below the Coulomb barrier, the third item will be irrelevant in what follows.

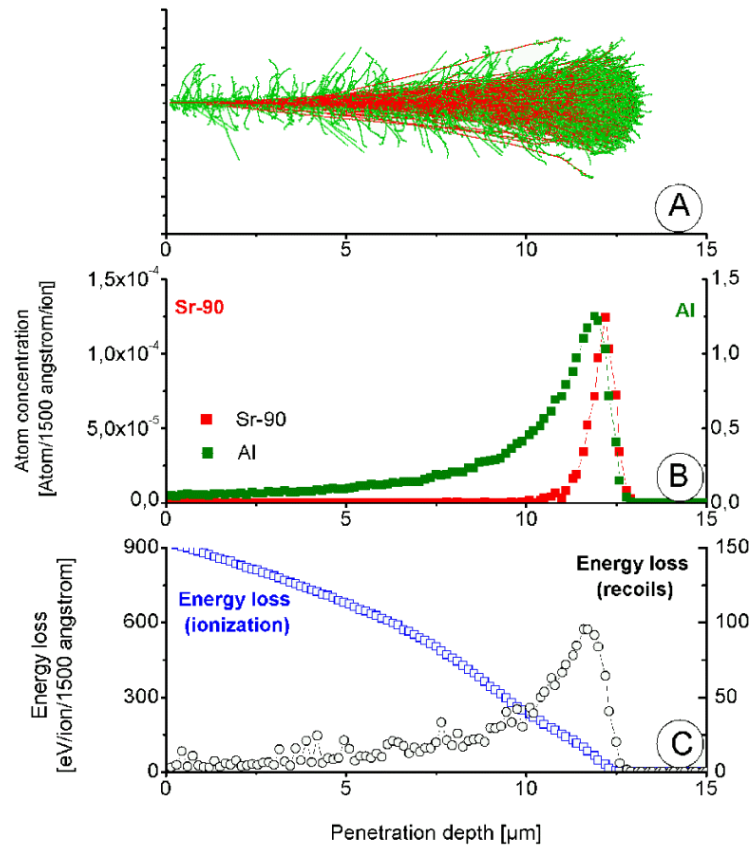


Figure 2.3: *Part A:* Traces of 1000 ^{90}Sr ions (red) into an aluminum target (the traces of the recoiled aluminum atoms are shown in green), the initial kinetic energy was set to 70 MeV *Part B:* Atom concentration of the ^{90}Sr projectiles and the recoiled atoms in the target versus the penetration depth *Part C:* Energy loss per ion and 1500 Å of the projectile by ionization and recoils.

Example: ^{90}Sr at 70 MeV into aluminum

This section is to show how a typical fission fragment, in this case ^{90}Sr , loses kinetic energy when it enters a typical material used in nuclear fuel, in this case aluminum. For this reason, simulations with the TRIM (transport of ions in matter) - code [27] have been carried out. TRIM is a Monte-Carlo-Code, which simulates the penetration of fast ions in matter. Fig. 2.3 A shows traces of 1000 ^{90}Sr ions (red) entering an aluminum target with an initial kinetic energy of 70 MeV. The density of the aluminum target was assumed to be $6.03 \cdot 10^{22}$ atoms/ cm^3 ($\equiv 2.702$ g/ cm^3). Also shown in this figure are the traces of the recoiled aluminum atoms (green).

The penetration depth for each projectile varies, but for a high number of histories an average penetration depth, lateral range, energy loss per unit of penetration etc. can be defined. Fig. 2.3 B shows the concentration of the projectiles (red) and the recoiled target atoms (green) in atoms per 1500 Å and ion versus the penetration depth. It shows that most of the projectiles are stopped in a narrow region, forming a

peak, its full width at half maximum (FWHM) is less than $1 \mu\text{m}$. The diagram shows that most of the target atoms are displaced shortly before the projectile stops. Not shown is the straggling of the projectile ($\approx 0.48 \mu\text{m}$), which is small in comparison to the penetration depth ($11.9 \mu\text{m}$), this means that the projectile maintains almost its initial direction. The skewness, which is a measure of the asymmetry of the final ion distribution (projectiles), is negative (-2.47) because the lower tail, on the left hand side of the peak, is longer than the upper one, on the right hand side of the peak. Since the distribution is much more precipitous than a Gaussian one, the kurtosis is greater than one (≈ 16.1). This part suggest collision events as target displacements. Assuming a displacement energy of 25 eV per target atom, in average $33\,978$ displacements ($32\,405$ creations of vacancies + 1573 replacement collisions) per ion are generated in the target, mainly at the end of each projectile history.

Fig. 2.3 C shows the average energy loss per ion and 1500 \AA due to direct ionization (66.9 MeV) and recoils (3.08 MeV) versus the penetration depth. The recoiled atoms loose their kinetic energy mainly by ionization (1.63 MeV) and creating phonons (1.27 MeV). A negligible portion of phonons are also generated by the projectile itself (26.9 keV).

Finally the law of conservation of energy is fulfilled:

$$\underbrace{70 \text{ MeV}}_{E_{kin}} = \underbrace{66.9 \text{ MeV}}_{\text{Ionization}} + \underbrace{3.08 \text{ MeV}}_{\text{Recoils}} + \underbrace{26.9 \text{ keV}}_{\text{Phonons}} \quad (2.3)$$

Ion ranges

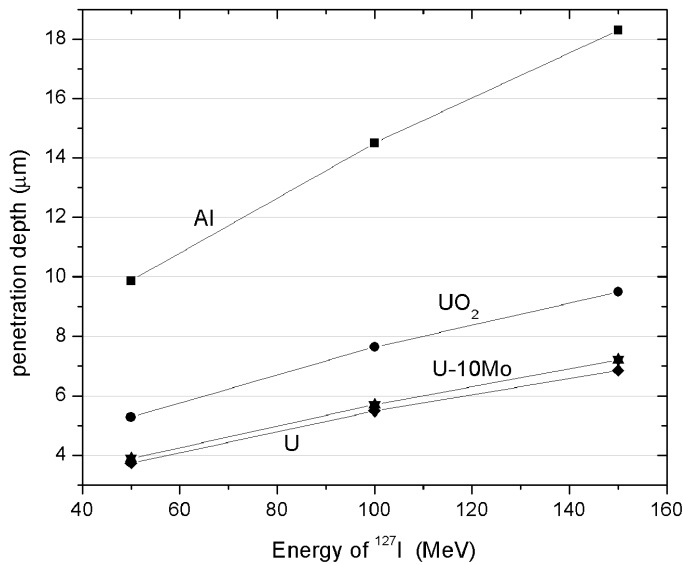


Figure 2.4: Penetration depth of ^{127}I into different materials versus energy

Fig. 2.3 part B shows that the distribution of the ion range has a very high kurtosis, therefore an effective penetration depth, i.e. ion range, can be defined. The effective penetration depth will be defined as the maximum of the ion range distribution. The

penetration depth depends on the ion, especially on the kinetic energy and the atomic number, and the target material. Fig. 2.4 shows the penetration depth into different targets versus the initial kinetic energy of the projectile. Here the projectile is ^{127}I , because iodine will be used later for irradiation (see chapter 3).

The diagram shows an almost linear dependence of the penetration depth on the projectile energy and an inversely proportional dependence between the mass density, more precisely: electron density, of the target and the penetration depth.

In conclusion, only the surface of the U-Mo/Al specimen will be modified by an bombardment with heavy ion. The effective penetration depth will be even less than suggested in the diagram due to an inclined irradiation with heavy ions.

Collision events

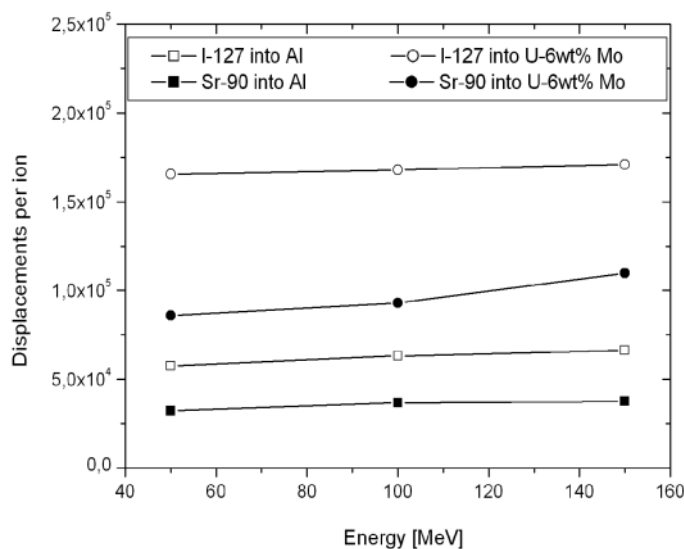


Figure 2.5: Displacements in the target versus kinetic energy of the projectile as calculated with the TRIM-code

In spite of the low contribution to the energy loss of the projectile, collision events cause important radiation damages and contribute to an atomic mixing. Collision events take place either as replacement collisions or as a creation of vacancies. Both cause an atomic displacement. Since displacements take place mainly at the last few micrometers of each heavy ion trace, it is not surprising that the number of displacements above a given threshold does not vary much with the kinetic energy of the projectile. But the number of displacements varies significantly for different target materials and projectiles. The number of displacements per ion versus the kinetic energy of the ion is shown in Fig. 2.5 for Al and U-6wt%Mo as targets, and ^{90}Sr and ^{127}I as projectiles. Hereby a displacement energy of 25.0 eV and a lattice binding energy of 3.0 eV was assumed for all target elements (aluminum, uranium, and molybdenum).

In general, the higher the density of the target and the heavier the projectile, the more displacements take place. To estimate an average number of displacements per

fission fragment, simulations have to be done for all fission fragments and targets, and weighted by their occurrence (see Fig. 2.2). Since not all displacement energies are available, especially in irradiated fuel, an assumption of $1 \cdot 10^5$ displacements per fission fragment seems reasonable. This number will be used later for all following calculations.

2.2.2 Sputtering

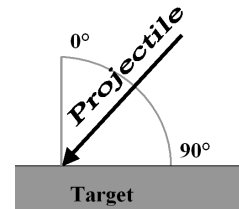
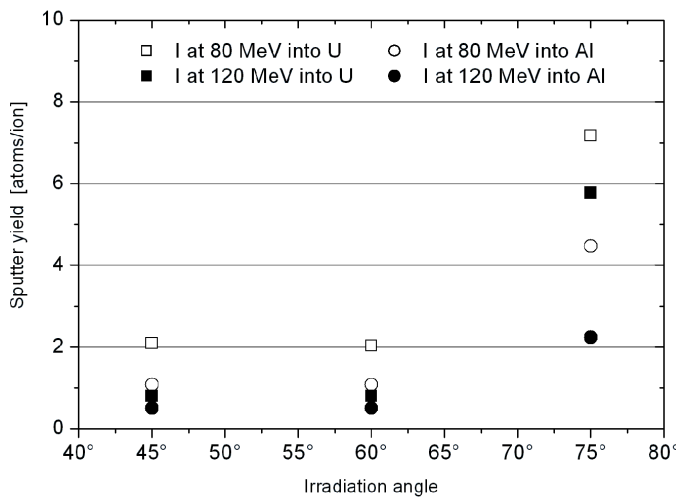


Figure 2.6: Sputter yields of iodine into aluminum and uranium versus irradiation angle.

Sputtering is largely driven by momentum exchange between the incoming projectile and atoms of the target material, due to (multi-)collisions. Therefore sputtering is possible, when displacements take place close to the surface.

Fig. 2.6 shows the sputter yield, that means how many atoms of the target are sputtered/released per incoming projectile, for iodine ions (projectile) at 80 and 120 MeV entering pure aluminum or uranium versus irradiation angle. An angle of $\alpha = 0^\circ$ denotes a perpendicular beam direction to the surface, and an irradiation angle of $\alpha = 90^\circ$ means that the beam is parallel to the surface. The surface binding energy of aluminum and uranium was assumed as 3.36 eV, and 5.42 eV as suggested by the TRIM-code.

The figure shows that as more collisions take place close to the surface the sputter yield is higher. That means the higher the angle and the lower the kinetic energy of the projectile or the higher the stopping power of the target material, the higher is the sputter yield.

In any case, the number of sputtered atoms is at least of the order of magnitude of the number of projectiles. Therefore a contamination of the irradiation device with the target material can not be completely excluded.

Table 2.3: Coulomb thresholds for Al, Mo, and U (target material) by irradiating with ^{90}Sr , ^{127}I , and ^{135}Xe (projectile)

projectile \ target	^{27}Al	^{92}Mo	^{235}U
^{90}Sr	56.6 MeV	152.1 MeV	281.4 MeV
^{127}I	73.6 MeV	200.1 MeV	373.4 MeV
^{135}Xe	74.0 MeV	201.6 MeV	376.9 MeV

2.2.3 Activation

One of the main advantages of heavy ion irradiation compared to in-pile reactor irradiation is that the fission fragments (i.e. projectiles) are stable and therefore not radioactive. But nuclear reactions of the projectile with the target atoms could lead to radioactivation. Therefore all nuclear reactions have to be excluded. A basic requirement for nuclear reaction is to overcome the Coulomb threshold. This threshold can be calculated with equation 2.4 [22].

$$V_C = \frac{e^2}{4 \cdot \pi \cdot \epsilon_0} \cdot \frac{Z_1 \cdot Z_2}{r_1 + r_2} \quad (2.4)$$

$$\text{with } r_{1,2} = 1.68 \text{ fm} \cdot A_{1,2}^{1/3}$$

Data for typical fission fragments and nuclear materials are presented in Tab. 2.3. By a comparison of these data with typical fission fragment energies, it can be concluded that activation of the specimen is not likely to occur, with the exception of aluminum. However, even after an irradiation to very high fluences with iodine, no activation could be measured.

2.2.4 Temperature consideration

The global temperature of a specimen will not change significantly due to a penetration of a swift heavy ion, since the deposited energy ($= E_{kin}$ of the projectile) is sparse compared to the required energy for a significant temperature increase ΔT .

$$\Delta T = \frac{E_{kin}}{m \cdot C_m} \quad (2.5)$$

Hereby denotes m the mass and C_m the heat capacity of the target.

However, this is different for very small volumes. Here temperature and their evolution is described by the thermal spike model [24, 25].

As described in the last section, charged particles are stopped mainly due to ionization. Therefore electrons are recoiled, i.e. they obtain kinetic energy. Now, two temperatures in a small volume can be defined - one for the electrons (T_e) and one for the lattice (T_l). That means, the energy loss of the projectile causes mainly an

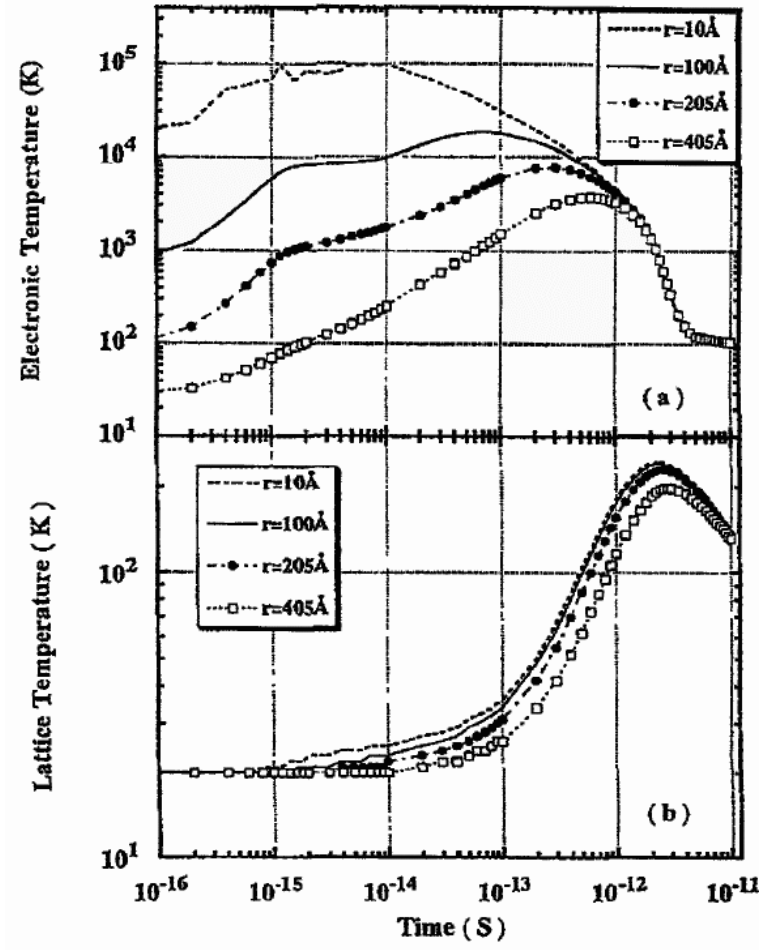


Figure 2.7: Calculated evolution of temperature for electrons and lattice while a 1190 MeV projectile (uranium ion) enters at time $t = 0$ s a copper target - taken from [25]

increase in the temperature T_e . The exact value of T_e depends on the heat capacity of the electrons C_e , the thermal conductivity of the electrons λ_e , the coupling to the lattice and finally on the total amount of deposited energy.

From here two differential equations follow, one for the electrons and one for the lattice [25]:

$$C_e(T_e) \frac{\delta T_e}{\delta t} = \nabla(\lambda_e(T_e) \nabla T_e) - g(T_e - T_l) + B_e(r, t) \quad (2.6)$$

$$C_l(T_l) \frac{\delta T_l}{\delta t} = \nabla(\lambda_l(T_l) \nabla T_l) + g(T_e - T_l) \quad (2.7)$$

with the coupling constant g for a free electron gas, t is the time, and $B_e(r, t)$ is the energy deposit in the electronic system.

$$g = \frac{\pi^4 (k_B n_e v)^2}{18 \lambda_l(T_l)} \quad (2.8)$$

here v means the sound-propagation velocity of the lattice

$$v = \frac{k_B T_l}{\hbar \sqrt[3]{6\pi^2 n_l}} \quad (2.9)$$

A more general expression, which is even valid for isolators and semiconductors, is [25]:

$$g = \frac{D_e \cdot C_e}{\tau^2} \quad (2.10)$$

Here D_e denotes the thermal diffusivity in the electron system and τ the mean free path length of the electrons.

And finally the life time t_{th} of the thermal spike is given by:

$$t_{th} \sim \frac{C\rho}{\lambda} \sim D_e^{-1} \quad (2.11)$$

That means: The lower the thermal diffusivity the longer is the lifetime of the thermal spike.

An example of the above mentioned algorithm is shown in Fig. 2.7. Here an 1190 MeV uranium ion enters a copper target at time $t = 0$ seconds. The diagram shows the temperature for the lattice (bottom) T_l and electrons (top) T_e of the copper target versus the time t for different radial distances to the trace of the projectile. Immediately after the impact, the temperature of the electrons increases and reaches a maximum of $10^5 K$, after approximately 10^{-15} to 10^{-14} seconds. During the cooling down of the electrons, the lattice warms up due to the electron-phonon coupling. The maximum temperature increase of around 200 K of the lattice is reached after around $2 \cdot 10^{-12}$ seconds. This means that for a copper-specimen considered at room temperature, the temperature of the lattice does not rise high enough to cause thermally activated displacements, nor is it high enough for a local melting, and consequent mixing of the atoms. The reason is the very high difference between room temperature and the melting point. Nevertheless, if the electronic diffusivity is low, because the lattice is heavily perturbed or in non-metals, the maximum temperature can rise much higher and a local melting could be possible.

2.3 Simulations of U-Mo/Al in-pile irradiation

This section is not directly necessary for a proper understanding of the heavy ion bombardment of U-Mo/Al dispersion fuel, but it provides data of the in-pile irradiation behavior of U-Mo/Al dispersion fuel. These data will be compared later with data of the heavy ion bombarded specimen.

In the frame of the conversion of the FRM II reactor from HEU to MEU, an in-pile irradiation test of U-Mo/Al dispersion fuel is under way. This test will be shortly described and one basic simulation, which has been carried out for this test, will be presented and discussed².

For the in-pile irradiation test, first of all six full size plates have been manufactured at CERCA. While all plates contain U-Mo/Al dispersion fuel, the uranium density varies slightly. Four of them have a uranium density of about 8g U per cm³ in the meat (denoted as UMo8001, UMo8002, UMo8501 and UMo8503) and two have a uranium density of 7g U per cm³ (denoted as UMo7001 and UMo7003). Only the UMo8xxx plates are scheduled to be in-pile irradiated, but if one of them fails, it will be replaced by a 7g U per cm³ plate. In order to improve the fuel performance the international community suggested adding silicon to the matrix [48]. The reason of adding silicon to the matrix is that annealing experiments have shown that a thermally activated diffusion from U-Mo particles into the aluminum matrix is suppressed. Therefore two of the higher density plates contain 2wt% Si in the aluminum matrix (UMo8501 and UMo8503). Since this kind of improvement is new, no experimental data from in-pile irradiation tests are available and consequently this improvement can not be taken into account in the simulation. Therefore the plates, which contain silicon, are simulated as plates without silicon. This means that the plates with the higher density vary only slightly in the volume loading and the porosity in the simulations, the variations are due to the manufacturing process of the fuel plates.

The in-pile irradiation takes place in the OSIRIS-reactor, operated by the CEA-Saclay, France, which is currently the most powerful open core material test reactor in the world.

2.3.1 The MAIA-Code

All simulations of the in-pile behavior of U-Mo/Al dispersion fuel, that will be presented in this work, are carried out with the MAIA-code. MAIA is a 2D thermo-mechanical code using a finite element method (FEM). The code was developed and is still under development at CEA-Cadarache and models for instance the growth of the IDL, disappearance of the as-fabricated porosity, swelling of the fuel particles or the oxidation

²Further simulations for full size plates, which include variations of the heat flux (= real heat flux) during the irradiation, are presented and discussed in the appendix B.

Table 2.4: Main input parameters for the simulation of the high density U-Mo/Al full size plate UMo8001

Fuel plate	
length	73.3 mm
thickness	1.3 mm
Cladding	
material	Al 5754 (AlMg3)
thickness	0.405 mm
thermal conductivity	130 W · m ⁻¹ · K ⁻¹
Meat (inside the fuel plate)	
length	55.5 mm
thickness	0.49 mm
as-fabricated porosity	8.13 vol%
Uranium density in the meat	8.48 g · cm ⁻³
wt% of Mo in fuel	8.0
kind of powder	atomized (spherical)
Particle size distribution	
r = 15 μm	0.8 wt%
r = 27 μm	3.7 wt%
r = 42.25 μm	22.2 wt%
r = 71.5 μm	73.3 wt%
stoichiometric proportion of the IDL (U-Mo/Al _x)	x = 5
Coolant	
type	light water
channel thickness	3.7 mm
channel width	68 mm
coolant velocity	12 m/s
heat transfer correlation	Dittus-Bölder
Oxidlayer	
oxid layer growth correlation	PAWEL88
off-set	0 μm
Irradiation conditions	
heat flux (constant)	300 W/cm ²
VHGR	12.24 W/mm ³
duration	70 d

of the fuel plate. A detailed description of MAIA is given in reference [28].

MAIA's development is carried out in close collaboration with the RERTR-team. The code of the RERTR-team is named PLATE. Therefore both codes achieve similar results. Both codes are still under development and are updated when new results are presented. In spite of the early state of both codes, reasonable results can be achieved and provide presently the best prediction for in-pile irradiation tests of U-Mo/Al dispersion fuel.

2.3.2 Input parameters

All relevant input parameters for the simulation are shown in Tab. 2.4. As far as possible all input parameter are representative for the UMo8001 plate. Discrepancies appear in the kind of particle powder and the particle size distribution. The type of particle powder had to be changed, because the six fabricated fuel plates (including the UMo8001 plate) contain ground powder³ and MAIA supports exclusively atomized powder, where each fuel particle has a spherical shape. Since a particle size distribution for ground powder is hard to define, here the one from the French FUTUR⁴ test is chosen.

Further, the table shows that the dimensions of the UMo8001 fuel plate are slightly different from that one of the FRM II, since the fuel plate has to fit into the irradiation device (called IRIS-device) at the OSIRIS reactor. One of the differences is for instance the thickness of the meat layer (-22%).

The heat flux q'' (\propto fission rate = fission per second and cm^3 in the meat) was assumed as constant ($q'' = 300 \text{ W/cm}^2$ ⁵) because the simulation had been carried out before the real irradiation was scheduled. Therefore the desired - but not real - heat flux was chosen in the simulation and set as constant.

The total duration of the in-pile irradiation was set in order to achieve at least the fission density (FD) of the maximum meat FD of the FRM II reactor ($2.1 \cdot 10^{21}$ fissions per cm^3 in the meat or in this case $3.7 \cdot 10^{21}$ fissions per cm^3 in the fuel particles). Therefore 70 effective full power days (EFPD) of irradiation were simulated, this means that a maximum FD in the meat, where the heat flux was fixed to 300 Watt per cm^2 , of $2.3 \cdot 10^{21}$ fission per cm^3 is achieved. This value corresponds to $4.2 \cdot 10^{21}$ fission per

³Ground powder means that the U-Mo particles are obtained through a grinding process. Therefore each particle of the powder has an arbitrary shape in contrast to powder, which has been obtained by an atomization process. Here each fuel particle has a spherical shape.

⁴FUTUR is a French full size in-pile irradiation test, which was carried out under similar conditions like the one for conversion of the FRM II. Some data are presented on page 52, Tab. 5.2. However, the powder used was atomized powder and the particle size distribution was known and therefore it is used.

⁵This heat flux seems to be currently the maximum allowed heat flux in the IRIS-device for this kind of irradiation [54], but (unfortunately) it is lower than the maximum heat flux at the FRM II (500 Watt per cm^2)

cm^3 in the fuel particles.

2.3.3 Results of simulations with constant heat flux

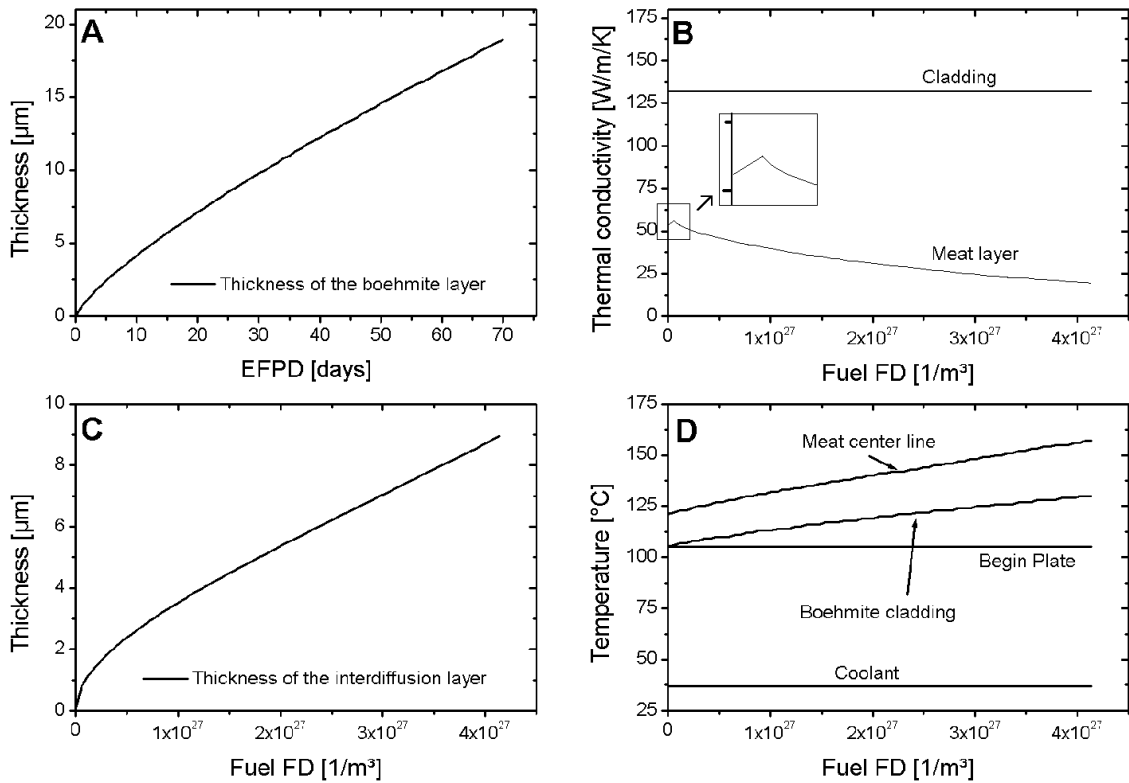


Figure 2.8: *Part A:* Thickness of the Boehmite-layer versus effective full power days (EFPD) of in-pile irradiation *Part B:* Thermal conductivity of the meat versus fission density (FD) in the fuel particles *Part C:* Thickness of the interdiffusion layer versus the FD *Part D:* Temperature at different position versus FD

Fig. 2.8 part D shows the temperature versus burn-up in fission per cm^3 in the fuel particles at different positions (coolant, begin of the plate = surface, the transition between the oxide layer of the fuel plate and the cladding, and in the middle of the plate = meat center line). Whereas the coolant temperature and the surface temperature are constant during irradiation, all other temperatures are increasing. The maximum temperature in the meat center line exceeds even 160°C . The reason for this temperature increase is, on the one hand, the growth of the oxide layer (more precisely: the growth of the boehmite ($\text{AlO}(\text{OH})$) layer - shown in Fig 2.8 part A), which arises on the surface of the cladding during in-pile irradiation and has a very low thermal conductivity, and on the other hand, the decrease of the thermal conductivity of the meat layer during burn-up (Fig. 2.8 part B). The thermal conductivity of the meat layer decreases due to the formation of the IDL, which will have a thickness, around each fuel particle, of approximately $9 \mu\text{m}$ at the final burn up. A little increase in the

thermal conductivity of the meat layer at the beginning of the irradiation is due to the filling of the as-fabricated porosity by fission gases (see. Fig. 2.8 part C). However, compared to Fig. 1.2 the thermal conductivity of U-Mo/Al dispersion fuel seems to be higher than for other dispersion fuel types, which are approximately $20 \text{ W}\cdot\text{m}^{-1}\cdot\text{K}^{-1}$.

This example for the simulation of an in-pile irradiation assumes many parameters. Variation of most of them can change the result significantly. For instance the growth of the boehmite layer depends largely on the pH-value of the coolant and the used relation. Since the exact pH-value was unknown, one of the easiest relation was used (Pawel), which does not take the pH-value into account. Therefore big uncertainties are expected.

The thickness of the boehmite layer directly affects the temperature of the meat. Since the growth rate of the IDL depends on the temperature, also the thermal conductivity of the meat depends on the temperature history of the meat. This means that a thicker boehmite layer would lead to a higher meat temperature, a higher meat temperature to a lower thermal conductivity of the meat, and this leads again to a higher meat temperature ... a self-energising process is started.

Nevertheless, the simulations, which have been carried out with MAIA- or the PLATE-code, fits with in-pile tests and therefore they seem to be a good and reasonable assumption.

Swelling

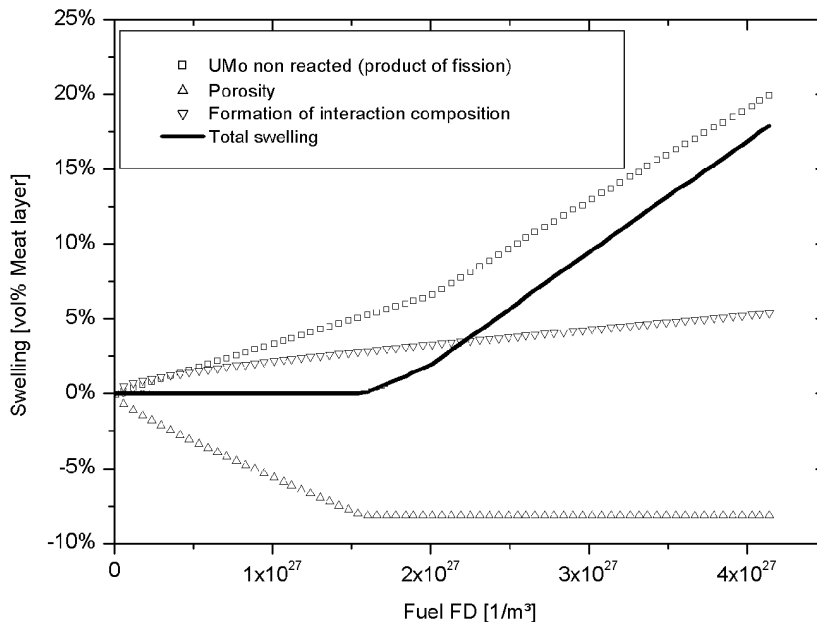


Figure 2.9: Contribution to the thickness swelling of the U-Mo/Al dispersion fuel plate

The swelling of a fuel plate during irradiation is of importance for in-pile irradiation tests, since this parameter measurement can be accomplished during irradiation breaks even with highly activated specimens. Therefore the swelling measurements provide

also information about the accuracy of the simulation or indicate a possible break away swelling.

Fig. 2.9 shows the swelling of the fuel plate and their contributions versus the fission density in the fuel particles. Contributions to the swelling are mainly due to the U-Mo particles, which are non reacted, and the formation of the IDL. Each contribution to the swelling can be almost compensated and as far as available by the consumption of the as-fabricated porosity, see Tab. 2.4. Therefore the start of the measurable plate swelling depends on the as-fabricated porosity.

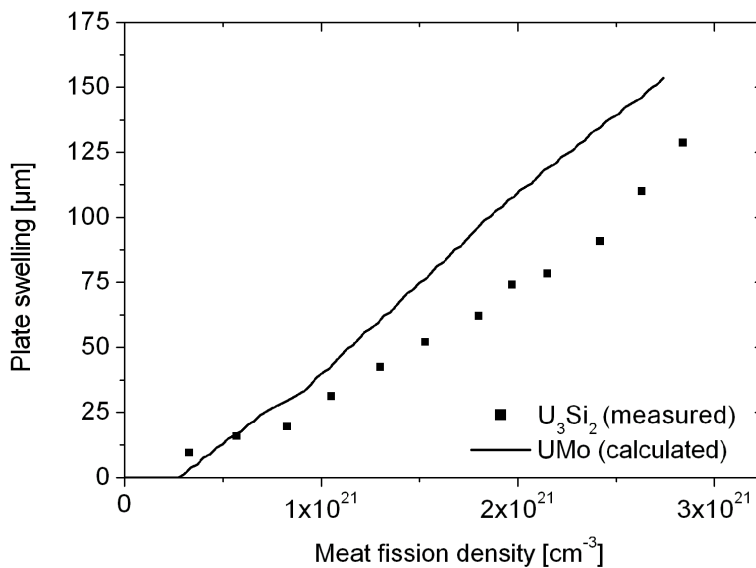


Figure 2.10: Swelling of U-Mo/Al dispersion fuel (8g U per cm³, calculation) and U₃Si₂/Al dispersion fuel (3g U per cm³, measurement) under similar irradiation condition.

In order to compare these data with the U₃Si₂/Al dispersion fuel, which is currently used in the FRM II reactor, simulations have been carried out for U-Mo/Al dispersion fuel under FRM II operating conditions. These simulated data will be compared with measured data of an in-pile test, which was carried-out in order to qualify U₃Si₂/Al dispersion fuel for the FRM II. This means that the irradiation condition in the simulation was set to a constant heat flux of 500 W per cm² for more than 52 effective full power days (see Fig. 2.10) within the same geometry. Due to the high porosity of the U-Mo/Al dispersion fuel, the swelling will start at a higher burn up, but also with a steeper slope. Therefore the swelling of the U-Mo/Al fuel plate will be slightly higher than for the U₃Si₂/Al fuel plate at the end of a cycle (52d · 20MW = 1040MWd) of the FRM II reactor. This means that the coolant channel will be slightly more reduced.

Since the limit of the U-Mo/Al dispersion fuel is not exactly known, a possible breakaway swelling can not be taken into account in the simulation.

Chapter 3

Irradiation experiment

3.1 Specimen preparation

Miniplates containing U-6wt%Mo/Al and U-10wt%Mo/Al dispersion fuel have been manufactured as plates for in-pile irradiation made by the RERTR-team. That means in this case:

First of all, spherical U-Mo particles in the metastable γ -phase have been produced by atomization. A detailed description of the atomization process can be found in [39]. Hereafter the U-Mo particles were mixed with almost pure aluminum powder (total impurities < 0.5 wt%). The volume fraction of the U-Mo particles in the meat was set to approximately 55 vol%. Hereafter the U-Mo/Al powder was put on a cladding (Al6061), surrounded by an aluminum frame and, once again a cladding layer is placed on the top, see Fig. 3.1. The frame is shown between the cladding, beside the meat layer. Several hot and cold rolling steps reduced the thickness of the plate and welded it together. Now the meat layer, which contains the fuel particles, is sealed in the cladding and the frame. Since the cladding is in most cases an layer of an aluminum-alloy (for instance Al6061, AlMg3, or AlFeNi) of some hundred micrometer, fission fragments can not pass this barrier during irradiation, but heat and neutrons can. Since atomized powder was used, the as-fabricated porosity is in the range of 1 vol%. Another set of specimen has been manufactured at CERCA in a similar way for heavy ion bombardment. Such specimen are shown in Fig. 3.2. They have been heavy ion bombarded, like the ones from the RERTR-Team, at the Munich Tandem Accelerator.

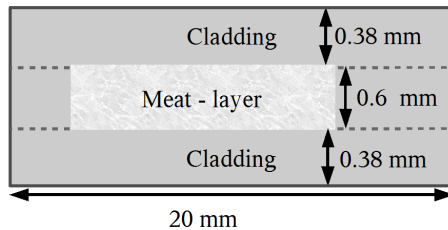


Figure 3.1: Cut-through sketch of a miniplate with typical dimensions



Figure 3.2: Miniplates manufactured at CERCA for heavy ion bombardment

Since the bombardment intended to simulate damages caused by fission fragments in the meat, the cladding had to be removed. This was carried out in a glove box by rough polishing. Later on the remaining meat layer was cut into pieces of $5 \times 5 \text{ mm}^2$. Finally a fine polishing resulted in a thin meat layer (foil), with a thickness of approximately $150 \mu\text{m}$. It was not possible to make the foil thinner because the biggest U-Mo particles were already polished on two opposite sides. An optical image of the specimen is shown in Fig. 3.3. It shows spherical U-Mo particles, each with a different diameter, in the aluminum matrix. Further, the last polishing direction is visible (shadows around the U-Mo particles) and a substructure of the U-Mo particle can be recognized. Analysis of the optical microscopy also revealed the particle size distribution, more precisely a diameter distribution d as determined by visual inspection. This distribution is shown in Fig.3.4. In order to obtain the real particle size distribution, the distribution has to be multiplied by a factor V .

$$V = \left(\int_0^1 \sqrt{1-y^2} dy \right)^{-1} \approx 1.27 \quad (3.1)$$

Hereby y denotes a variable.

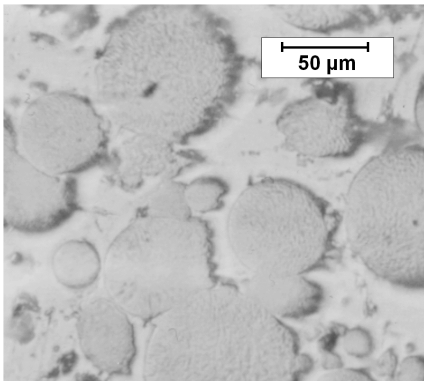


Figure 3.3: Optical microscopy of an U-6wt%Mo/Al specimen after polishing

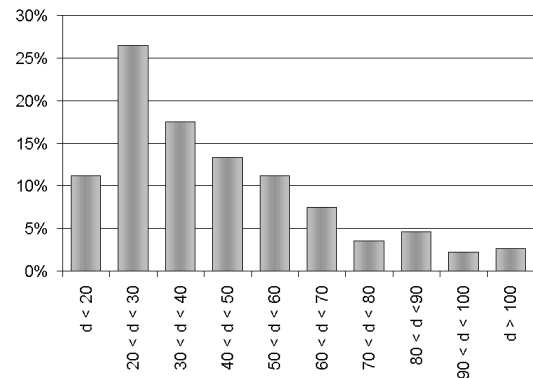


Figure 3.4: Diameter (d) distribution as determined by visual inspection of the U-Mo particles after polishing

3.2 Heavy ion accelerator and irradiation device

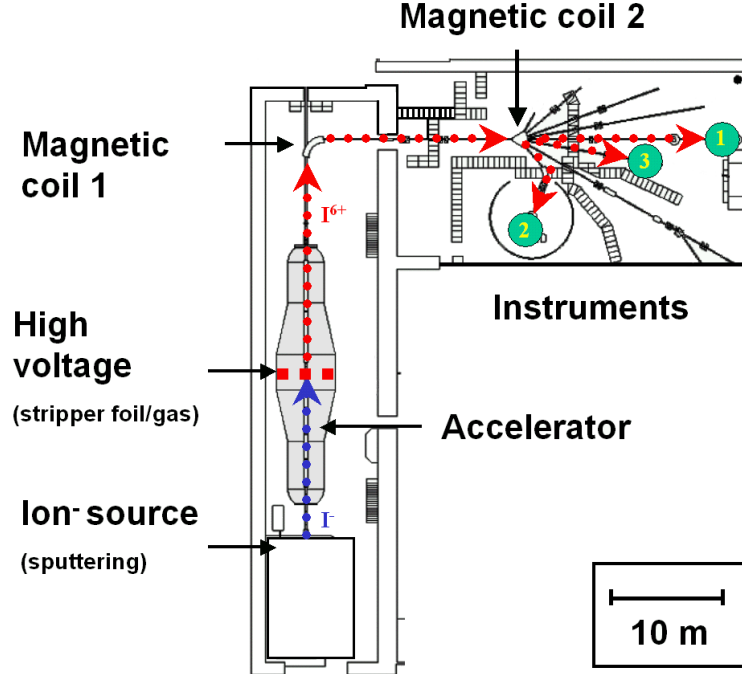


Figure 3.5: Sketch of the heavy ion accelerator

All specimens have been irradiated at the Munich tandem accelerator of the Maier-Leibnitz Institute in Garching, Germany [56], which is operated by the Ludwig - Maximilian - Universität and Technische Universität München. A sketch of the accelerator is shown in Fig. 3.5. On the bottom left hand side it shows the ion source. Here ions are produced by sputtering from a solid target. Ions, which are negatively charged, are attracted by the positive potential of the accelerator¹. In the middle of the accelerator, where the voltage is at its highest value ($V_{acc,max} \approx 14$ MV), electrons are stripped off from ions either by a stripper foil (carbon) or a gas (nitrogen). While a stripper foil has the potential of removing more electrons on average from the ion, the gas stripper allows a much higher particle flux. After passing the stripper, ions are positively charged. This means that they are pushed away from the high positive voltage of the accelerator. Now the ions will be accelerated to their final speed. The final kinetic energy $E_{kin,final}$ can be calculated by:

$$E_{kin,final} = (1 + i) \cdot e \cdot V_{acc} + V_{pre-acc} \cdot e \quad (3.2)$$

where i is the charge states of the ion after the stripper and $e = 1.602 \cdot 10^{-19}$ C. For instance: If iodine ions with a kinetic energy of $E_{kin} = 80$ MeV are desired with a high

¹Indeed there is a pre-accelerator as well, which will not be taken into consideration, but has a weak contribution to the final kinetic energy of the ion, around 150 keV and the sputter target is covered by a thin Cs layer in order to increase the yield of negatively charged ions.

Table 3.1: Parameter of the different irradiation positions with typical operation condition

	Position 1	Position 2	Position 3
isotope	I-127	I-127	I-127
charge state	11+	11+	6+
projectile energy	100 MeV	120 MeV	80 MeV
beam power	0.18 W	6 Watt	27 watt
particle flux	10^{10} s^{-1}	$3 \cdot 10^{11} \text{ s}^{-1}$	$2 \cdot 10^{12} \text{ s}^{-1}$
beam size	$10 \times 10 \mu\text{m}^2$	$2 \times 2 \text{ mm}^2$	$4 \times 4 \text{ mm}^2$
temperature measurement	-	possible	possible
cooling of the specimen	-	-	possible

particle flux, the gas stripper will be chosen. Since one of the most probable charge state of the iodine ions after stripping is $i = 6+$, the accelerator voltage has to be set to $V_{acc} = 11.4 \text{ MV}$, since:

$$(6 + 1)e \cdot 11.4 \text{ MV} + 0.15 \text{ MeV} \cong 80 \text{ MeV}. \quad (3.3)$$

The ion flux can be measured at several positions by putting a conductive cup into the beam. Beside the cups, there are beam profilers, electrical fields, magnetic lenses and coils for characterizing and guiding the beam.

The heavy ion beam has to pass at least two magnetic coils. The first magnetic deflection (90°) is done in order to filter the beam, only one isotope with the appropriate energy can pass it. Magnetic coil 2 directs the heavy ion beam to the instrument. This means that the accelerator can serve only one instrument with one energy and one isotope at a time.

Irradiation experiments have been carried out at three different positions. They are numbered chronologically in Fig. 3.5. The first two irradiations were carried out on still existing instruments, but at position number 3 a special irradiation device shown in Fig. 3.6 has been build. Some characteristic values of all the irradiation positions are given in Tab. 3.1.

In position number 1 (Instrument SNAKE) a microfocus beam has been used. The aim was to irradiate a single fuel particle. Therefore all "fission fragments" should be produced in the fuel particle. However, it turned out, that it was impossible to guide the heavy ion beam exactly onto one fuel particle. The reasons were an insufficient specimen preparation (specimen were delivered on the same day as the bombardment took place, therefore a better preparation was impossible) and difficulties in detecting the beam on the specimen.

In position number 2 (Instrument Q3D) a larger heavy ion beam has been used, therefore fuel and matrix were irradiated at the same time. Due to the bigger beam,

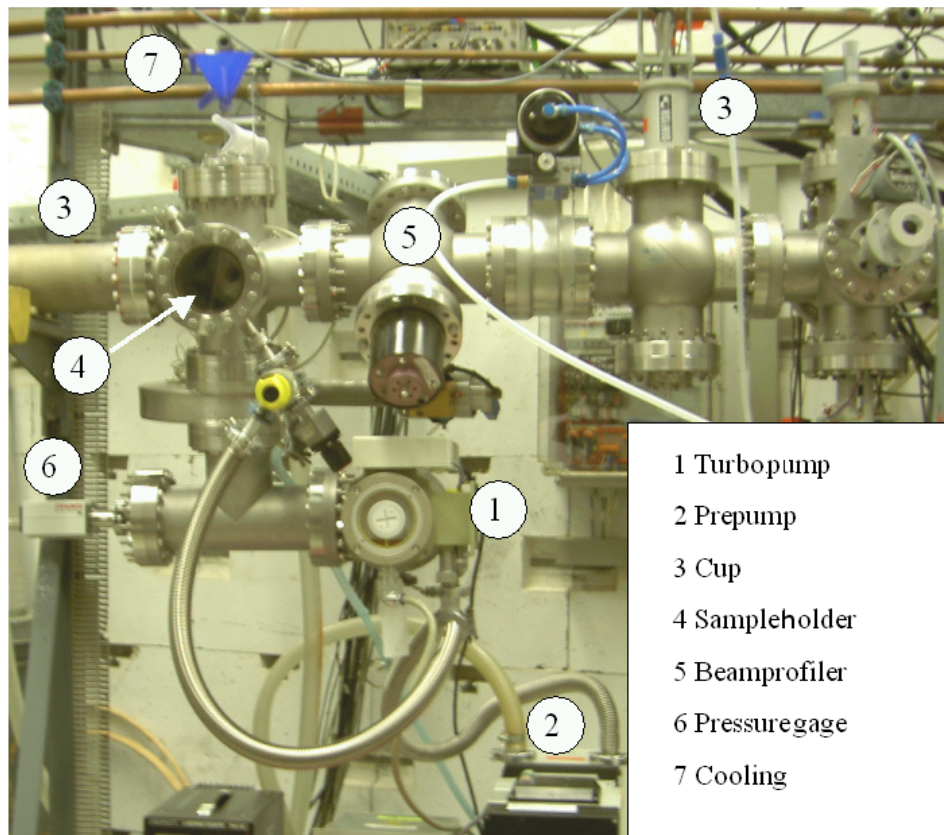


Figure 3.6: Device for bombardment at very high fluxes

the particle flux (ion per cm^2 and s) was reduced and could be not increased. The limitation is caused by magnetic coil 2 in Fig. 3.5. Here the beam can only be deflected with a high charge state, which is only possible with a stripper foil. Therefore the new irradiation device has been built at a position, where the beam should pass magnetic coil 2 with a small deflection of only 10 degrees.

Since the here used specimens act as pure beam stops, the irradiation device itself is one of the simplest instruments in the accelerator. It provides just everything what is necessary for a perfect bombardment of the specimen. An in-situ temperature measurement and cooling of the specimen, as well as a characterisation of the beam is possible and can be monitored. Due to a sophisticated pumping system, a change of the specimen is possible in less than 15 min. After 15 minutes the required vacuum ($1.0 \cdot 10^{-7}$ mbar) is in the recipient achieved and the shutter to the accelerator will open.

Additionally an active water cooling of the specimen was required, because the total energy input can easily exceed 50 Watts. Taking into account the total heat capacity of the specimen, a decomposition of the metastable γ -phase of the U-Mo fuel particles could occur or the specimen could even melt in seconds.

3.3 Irradiation conditions

The irradiation conditions were set in order to be as close as possible to in-pile irradiation. That means:

- Since the penetration depth of the heavy ions is only in the range of some micrometer, the **meat layer** must be **irradiated directly**.
- In order to simulate in-pile irradiation, the bombardment has to be carried out under the smallest angles as possible, between the heavy ion beam and the surface of the meat layer. This simulates fission products which are going from the fuel particle into the matrix (see Fig. 3.7 position B). Unfortunately the sputter yield increases significantly, by reducing the angle between the heavy ion beam and the surface of the specimen (see Fig. 2.6), as the best compromise an **irradiation angle** $\alpha = 60^\circ$ between the heavy ion beam and the perpendicular direction to the surface was chosen as described in the sketch on page 16.
- Simulations in chapter 2.3 have shown that the meat temperature during in-pile irradiation is in the region of around 150-200°C depending on the burn-up. Therefore the **temperature was limited to 200° C**.
- The final dose (fluence) was set between $5 \cdot 10^{16}$ and $1 \cdot 10^{18}$ ions per cm^2 in an area between $2 \times 2 \text{ mm}^2$ and $4 \times 4 \text{ mm}^2$. Assuming a penetration depth of $6.2 \mu\text{m}$ and $16.5 \mu\text{m}$ into U-6wt%Mo and Al respectively, this will result in an ion density of at least $1.6 \cdot 10^{20}$ ion per cm^3 , respectively $6 \cdot 10^{19}$ ion per cm^3 . Due to the high kurtosis, the real ion density is in certain locations even higher, around a factor of 10 in a region of $1 \mu\text{m}$ thickness. This means that at least the final fission density of the FRM II core (see chapter 1) is obtained at certain layers.
- The duration of an irradiation varied between just some minutes and went up to 13.5 h, depending mainly on the desired fluence, beam size and the kind of the stripper in the accelerator.
- All irradiations have been carried out under vacuum ($1.0 \cdot 10^{-7}$ mbar).

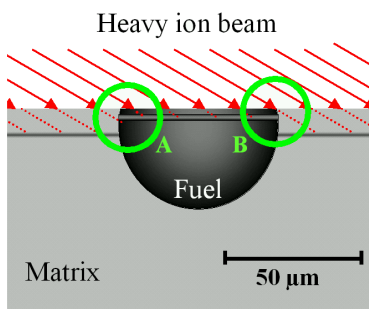


Figure 3.7: Concept of the heavy ion bombardment. In position B a simulation of in-pile irradiation is possible, since here the "fission fragments" go from the fuel particle into the matrix as it happens during in-pile irradiation - in position A vice versa.

Chapter 4

Post irradiation examination

Usually experiments at the accelerator aim to analyze specimens. Here the aim is to modify specimens with the swift heavy ion beam of the accelerator. The analysis will be carried out later, on other instruments. In this chapter the analysis, called: post irradiation examination (PIE), of the specimen will be presented. At first PIEs will be carried out as for in-pile irradiated specimen, that means optical microscopy (OM) and scanning electron microscopy (SEM) will be taken, and later an examination using synchrotron radiation will be presented. Previously this kind of examination could not be done with in-pile irradiated specimen due to the strong activation of the specimen.

Further, I want to point out that one of the main advantages of heavy ion bombardment compared to in-pile irradiation is that PIE's can be conducted immediately after irradiation. In-pile irradiated specimen for instance require at least 6 to 12 months of decay time. Subsequently the strongly activated specimen must be transported from the reactor to a PIE-facility in a special cask. Thereafter the PIEs can be carried out exclusively in hot cells with suitable instruments. Additionally the PIE's are hampered by the strong background radiation. After the PIEs, storage and disposal of the specimens cause difficulties as well. Therefore in-pile irradiation tests are extremely costly and time consuming.

For heavy ion irradiated specimen the radiation of the specimen is the natural radiation from the uranium, especially from ^{234}U and ^{235}U , both isotopes are especially important for enriched specimen. That means, for the used specimens with 19.75 wt% enriched uranium, a dose rate of $\approx 1 \mu\text{Sv}$ per hour on the surface per specimen can be measured. The dose rate is caused by α - (approximately 8 Bq), β - (approximately 30 Bq), and γ - radiation (low energetic, mainly less than 200 keV). Therefore no special shielding is required. Nevertheless, since uranium is a heavy metal, inhalation or ingestion of the specimen is to be avoided.

Also no further preparation is necessary, because the meat layer is still accessible by photons and electrons. Finally, I point out that PIEs can be accomplished as easily as for an arbitrary alloy of heavy metal. Therefore PIEs can be conducted in almost every laboratory or research facility. Thus making it possible to obtain better results

than for in-pile irradiated specimen by reducing costs and time required.

4.1 Optical microscopy

After the heavy ion bombardment, first of all an optical inspection of the specimen took place, which revealed that the irradiated area of the specimen is very dark. Therefore irradiated and non-irradiated areas can be easily differentiated. But therefore optical analysis is difficult, especially at the transition between irradiated and non-irradiated areas. Such a transition is shown in Fig. 4.1. First of all one realizes that the irradiated area seems to be underexposed, while the non-irradiated area seems to be overexposed, and further, that each spherical fuel particle in the irradiated area is surrounded by a new layer with distinct borders and a blue color. Hence this new layer will be called interdiffusion layer (IDL). The thickness of the IDL is approximately $20\ \mu\text{m}$ and its blue color is probably due to the incorporation of the iodine. Assuming a penetration depth of the iodine perpendicular to the surface of the specimen of $2\ \mu\text{m}$ and a fluence of 10^{17} ions per cm^2 , the iodine concentration would be as high as $5 \cdot 10^{20}$ ions per cm^3 . This is just one order of magnitude less than the atom density of the specimen.

The matrix has still the color of the aluminum, presumably due to the much higher penetration depth of the projectiles, and the fuel particles get a black color due to the oxidation at the air. Fig. 4.2 to 4.4 show optical images of U-6wt%Mo/Al and U-10wt%Mo/Al specimen, which have been irradiated up to relatively low fluences under the same conditions. Each picture shows an irradiated part of a comparable position of the specimen. The figures show that the specimen with the lowest fluence (Fig. 4.3) is the brightest one, but in principal there is not a big difference between these images. The thickness and shape of the IDL is almost the same in all three images. Therefore we conclude that there is not a big influence of the molybdenum content and the fluence on the IDL-growth rate. The direction of the heavy ion irradiation is shown by the arrow.

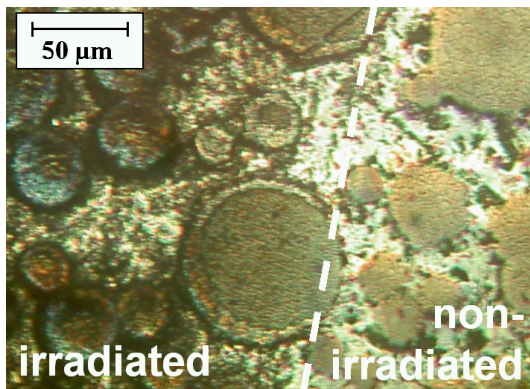


Figure 4.1: Optical image of a transition between irradiated and non-irradiated areas on a U-6wt%Mo/Al specimen.

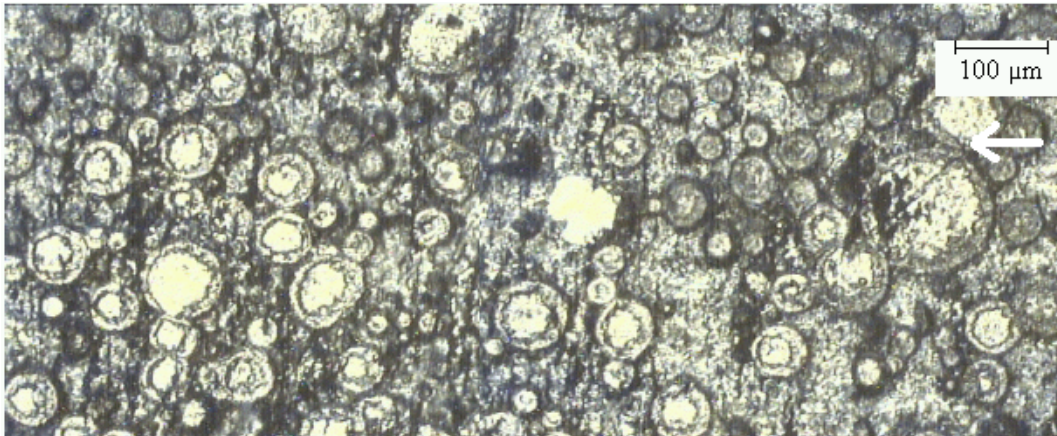


Figure 4.2: U-6wt%Mo/Al specimen, irradiated to a fluence of 10^{17} ions/cm²

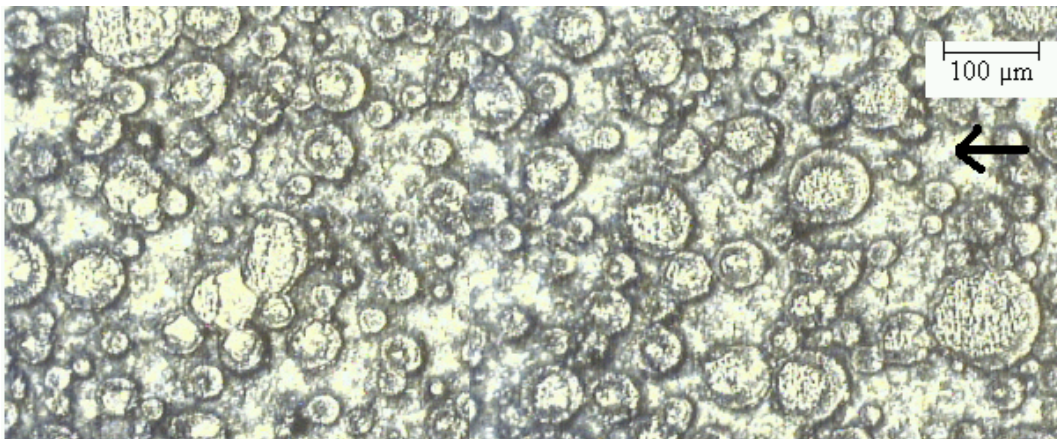


Figure 4.3: U-10wt%Mo/Al specimen, irradiated to a fluence of $5 \cdot 10^{16}$ ions/cm²

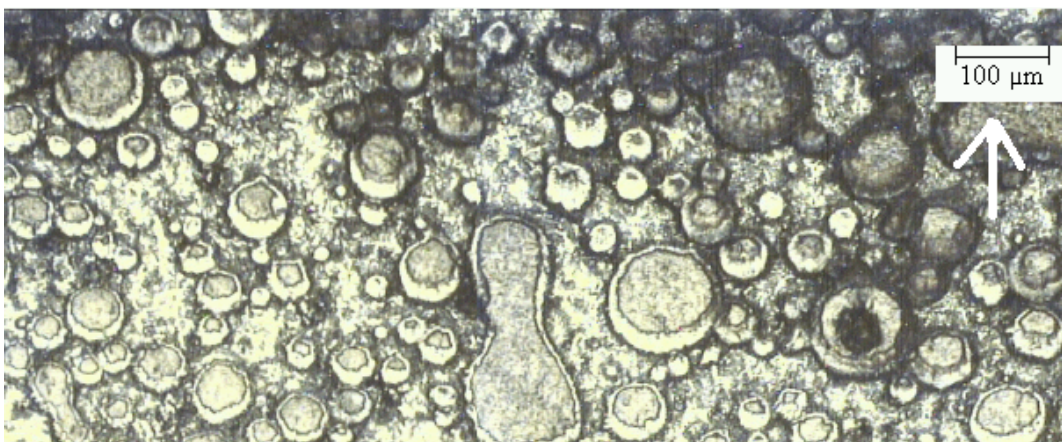


Figure 4.4: U-10wt%Mo/Al specimen, irradiated to a fluence of 10^{17} ions/cm²

4.2 Scanning electron microscopy with EDX

Scanning electron microscope (SEM) images were taken from a Hitachi model s-4000 field emission scanning electron microscope. Here the accelerating voltage was set to 20 keV. Specimen were mounted on a specimen holder, which had a slope of 45° between the electron beam and the surface of the specimen.

Whereas optical images of a transition between an irradiated and non-irradiated area were difficult to obtain, this is no challenge for a SEM. Such a transition is shown in Fig. 4.5. At first glance, a significant change due to the irradiation is visible between this two areas. Here also distinct borders between the fuel, the IDL and the matrix are clearly visible.

Fig. 4.6 to 4.8 show images of irradiated U-Mo/Al specimen. Each image shows - like the optical one - around each spherical U-Mo particle an IDL, but with much more detail. For instance here it can be seen that the IDL is particularly pronounced in the direction of the irradiation. Now also a thickness measurement of the IDL can be easily carried out. The thickness of the IDL is approx. $30 \mu\text{m}$ for position A in Fig. 3.7 and approx. $10 \mu\text{m}$ for position B in Fig. 3.7. Further, the thickness of the IDL seems to be independent of the fuel particle diameter, which is in agreement with the in-pile irradiated specimen.

It should also be mentioned, Fig. 4.8 (SEM-image) and Fig. 4.4 (optical image) show a mirror image of the same part of an U-10wt%Mo/Al specimen. Both show similar dimensions of the fuel, the matrix and the IDL.

On the fuel particles itself ripples are visible, which are perpendicular to the incoming beam. They suggest surface amorphisation. These ripples are shown in detail in Fig. 4.9.

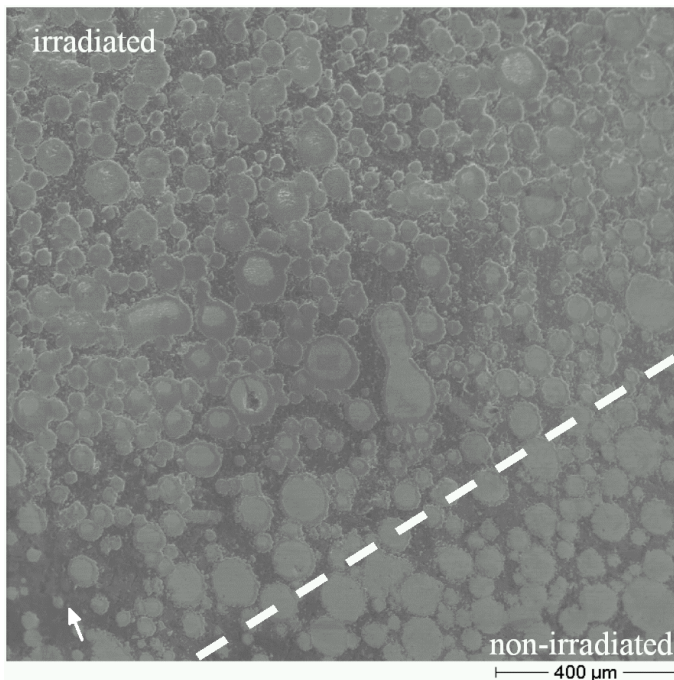


Figure 4.5: SEM image of an U-10wt%Mo/Al specimen, partly irradiated to a fluence of $1 \cdot 10^{17}$ ions/cm²

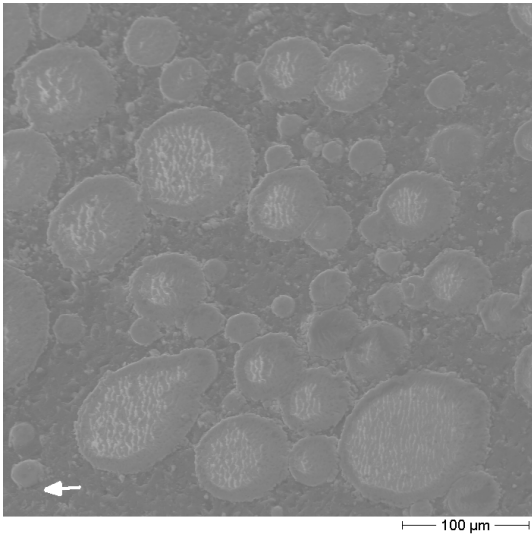


Figure 4.6: SEM-image of an U-6wt%Mo/Al specimen, irradiated to a fluence of $1 \cdot 10^{17}$ ions/cm²

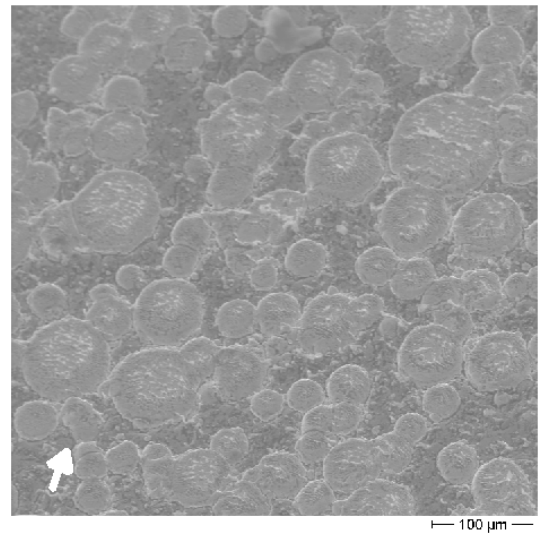


Figure 4.7: SEM-image of an U-10wt%Mo/Al specimen, irradiated to a fluence of $5 \cdot 10^{16}$ ions/cm²

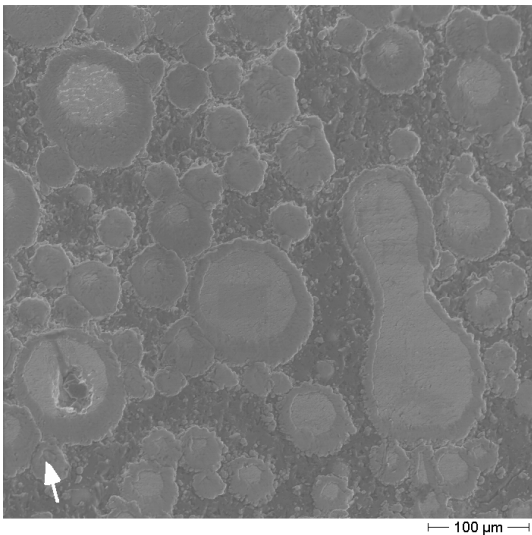


Figure 4.8: U-10wt%Mo/Al specimen, irradiated to a fluence of $1 \cdot 10^{17}$ ions/cm², SEM-image, part of Fig. 4.5

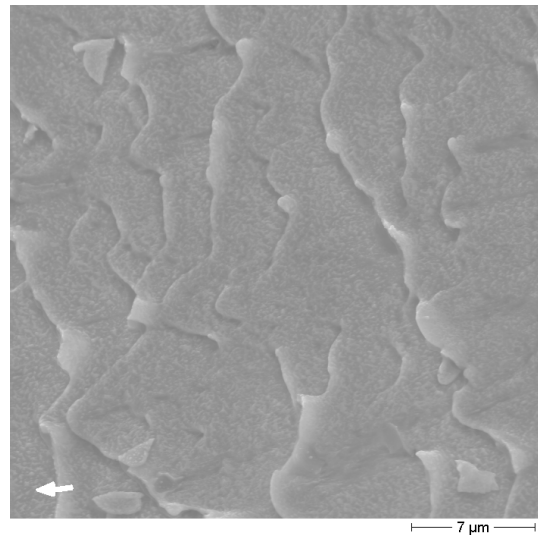


Figure 4.9: Ripples on a U-6wt%Mo fuel particle, irradiated to a fluence of $1 \cdot 10^{17}$ ions/cm², SEM-image

Energy-dispersive X-ray analysis

By taking SEM-images, the elements of the specimen are excited by high energetic electrons. Therefore they emit typical X-rays. These X-rays can be measured and analyzed. Now a qualitative and quantitative composition of the elements of the specimen is obtained with a high spatial resolution. This technique is called Energy-Dispersive X-ray analysis (EDX). Most relevant X-ray energies, types, and probabilities for our application are given in Tab. 4.1.

A qualitative analysis of the element distribution by EDX was performed at an EDR288, where the emitted X-rays are detected by a Si(Li) detector. Fig. 4.10 shows a SEM-image of an irradiated fuel particle (U-10wt%Mo) in an aluminum matrix. While the arrow marks the direction of the incoming heavy ion beam, the encircled numbers present the position where the EDX-measurements have been carried out. Results of these measurements are shown in Fig. 4.11. The measuring time for each EDX-measurement was in the range of 200 seconds - depending on the dead time of the detector and position at the specimen. The EDX-data show a homogeneous distribution of uranium and molybdenum in the fuel, and pure aluminum in the matrix. In the IDL, there is a weak gradient of the elements. While uranium and molybdenum are decreasing, aluminum increases slightly in the direction from the fuel to the matrix.

A quantitative analysis of the EDX-measurements yielded a composition of the IDL of (U-Mo)Al_{3±1} depending on the specimen (U-6wt%Mo/Al or U-10wt%Mo/Al), the position (close to the fuel or to the matrix, center of the irradiated area etc.) and, last but not least, at the correction for the Bremstrahlung.

Table 4.1: Some important X-ray energies for EDX measurements

Element	Energy (keV)	Type	Probability
Al	1.487	K _{α1}	0.9868
	1.557	K _{α2}	0.0132
Mo	2.293	L _{α1}	0.9274
	2.395	L _{β1}	0.9333
	2.518	L _{β2}	0.9096
	0.192	M _{α12}	1
I	0.497	M _{α12}	0.85
U	3.171	M _{α12}	0.54
	3.336	M _β	0.33

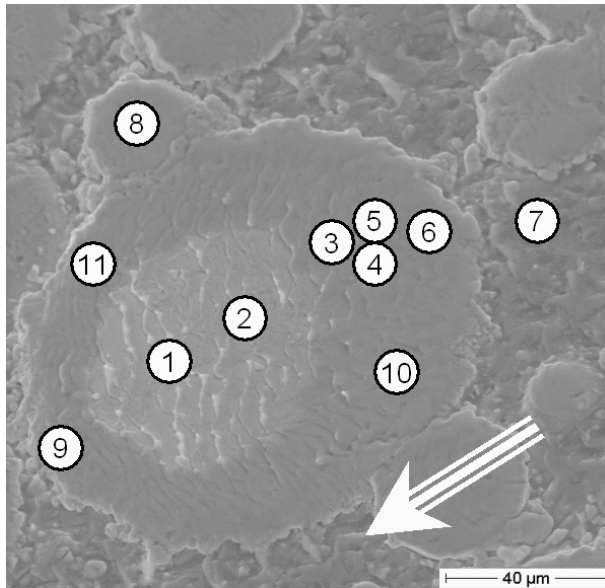


Figure 4.10: SEM-pictures of an U-10wt%Mo/Al specimen, irradiated to a fluence of 10^{17} ions/cm². Encircled numbers indicate positions where EDX-measurements have been carried out, see. Fig. 4.11

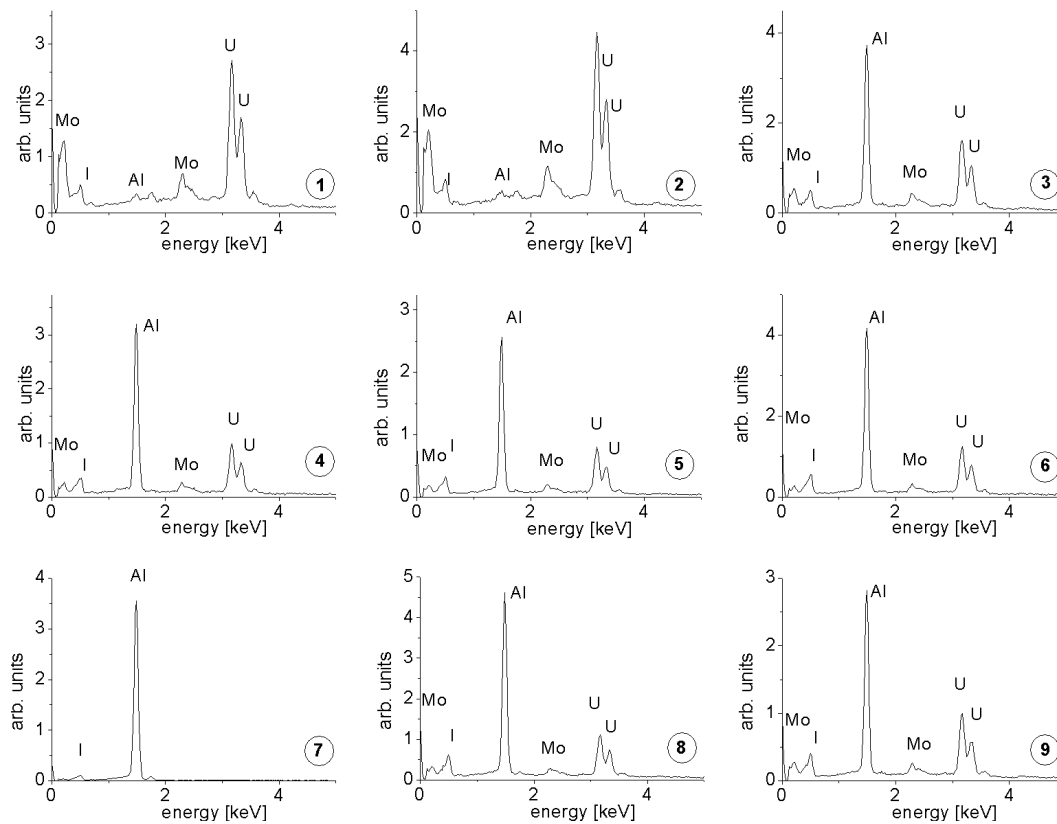


Figure 4.11: EDX-measurements of the specimen which is shown in Fig. 4.10

4.3 X-ray diffraction measurements

This section aims to identify the qualitative composition of the IDL. Since heavy ions and photons with the appropriate energy (see Tab. 4.2) have similar penetration depths¹, X-ray diffraction measurements are carried out in Bragg-Brentano geometry (see Fig. 4.12). Hereby two different approaches are applied. In the first approach the X-ray beam diameter and the detector have a similar size to the irradiated area on the surface of the specimen. Texture effects, which are expected - especially in the aluminum matrix, due to the rolling during manufacturing, are reduced by a rotation of the specimen during the measurement. A comparison between an irradiated and a non-irradiated specimen is expected to provide the composition of the IDL.

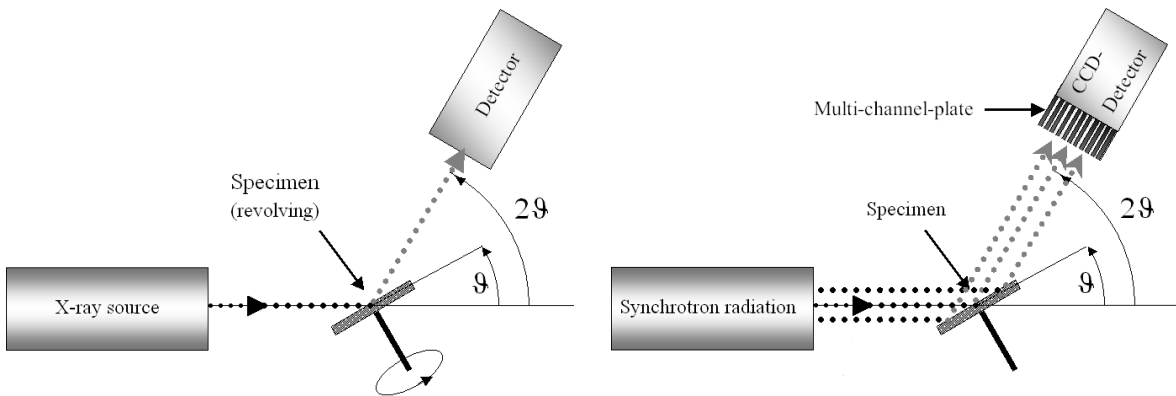


Figure 4.12: Bragg-Brentano geometry for first diffraction measurement (left hand side) and second diffraction measurement (right hand side)

The second approach aims for a higher spatial resolution, which is not possible with the first one. This is achieved by a high brilliance X-ray beam (high intensity and the X-ray beam has a low divergence, here synchrotron radiation will be used) and a detector with a very high spatial resolution. Here realized by a CCD-detector, which presents a two-dimensional array of detectors. Due to a multichannel plate, which acts as an array of collimators, between the specimen and the detector, a measurement with a high spatial resolution is possible. Of course this measurement must be done without a rotation of the specimen.

Two specimen are studied in detail with X-ray diffraction, both are irradiated to a fluence of $1 \cdot 10^{17}$ ions/cm². They differ only in the Mo-content in the fuel particles. One contains 6wt%Mo and the other one 10wt%Mo.

¹Unlike the penetration depth of heavy ions (detailed description in chapter 2.2 on page 12), X-ray attenuation obeys an exponential law. Therefore the penetration depth is defined as the length when the X-ray concentration is attenuated to a factor of $1/e$.

Table 4.2: Penetration depth of photons (A) [30] and heavy ions (B) [27]

	Type / Isotope	Energy	Penetration depth into	
			Al	U-6wt%Mo
A (photons)	Cu K_{α}	8.5 keV	87.8 μm	2.4 μm
	Mo $K_{\alpha 1}$	17.4 keV	719.2 μm	6.3 μm
B (heavy ion)	I-127	120 MeV	16.5 μm	6.2 μm
	I-127	80 MeV	12.9 μm	5.0 μm

4.3.1 First diffraction measurement

A first X-ray powder diffraction (XRD) measurement was performed with a STOE-STADIP diffractometer, where a curved, primary Ge(111) crystal monochromator produces strictly monochromatic Mo- $K_{\alpha 1}$ -radiation ($\lambda=0.07093$ nm). Three specimens (the two irradiated specimen and one non-irradiated U-6wt%Mo/Al specimen) were analyzed in reflection geometry (Bragg-Brentano) and a linear position sensitive detector (acceptance 6° , channel width 0.02°) coupled in a 1:2 mode was used for data acquisition. Up to 2700 data points in the angular range of 6° - 60° were taken for each specimen in 24 hour runs at an incoming beam diameter of approximately 1 mm. Hereby the specimen was revolving.

The obtained diffraction patterns are shown in Fig. 4.13. For the non-irradiated specimen peaks from aluminum and γUMo can be easily differentiated. Due to their inner structure the aluminum peaks are not so broad like the one from γUMo . Further one recognizes that the heavy ion bombarded specimens show the presence of new crystalline phases compared to the non-irradiated specimen.

Qualitative phase analysis indicates the presence of up to five crystalline phases, whose reflection positions are marked in the lower part of Fig. 4.13. The main reflexes are identified by the hkl-values directly in the diffraction pattern. Further I wish to emphasize that no decomposition of the metastable $\gamma\text{U-Mo}$ phase was observed. Evidence of neither a ternary (Al, Mo, and U) nor a binary compound of Al and Mo could be found. A detailed study of the peak width revealed no significant peak broadening for heavy ion irradiated specimen compared to the non-irradiated ones.

Quantitative multiphase Rietveld analysis yields the respective weight fractions of the specimen as shown in Tab. 4.3. Both irradiated specimens contain a significant portion of UAl_3 . Further, UAl_4 is present. In the U-10 wt% Mo/Al specimen UAl_2 also exists. These compounds did not exist before the irradiation with heavy ions and therefore they ought to be products of the irradiation process.

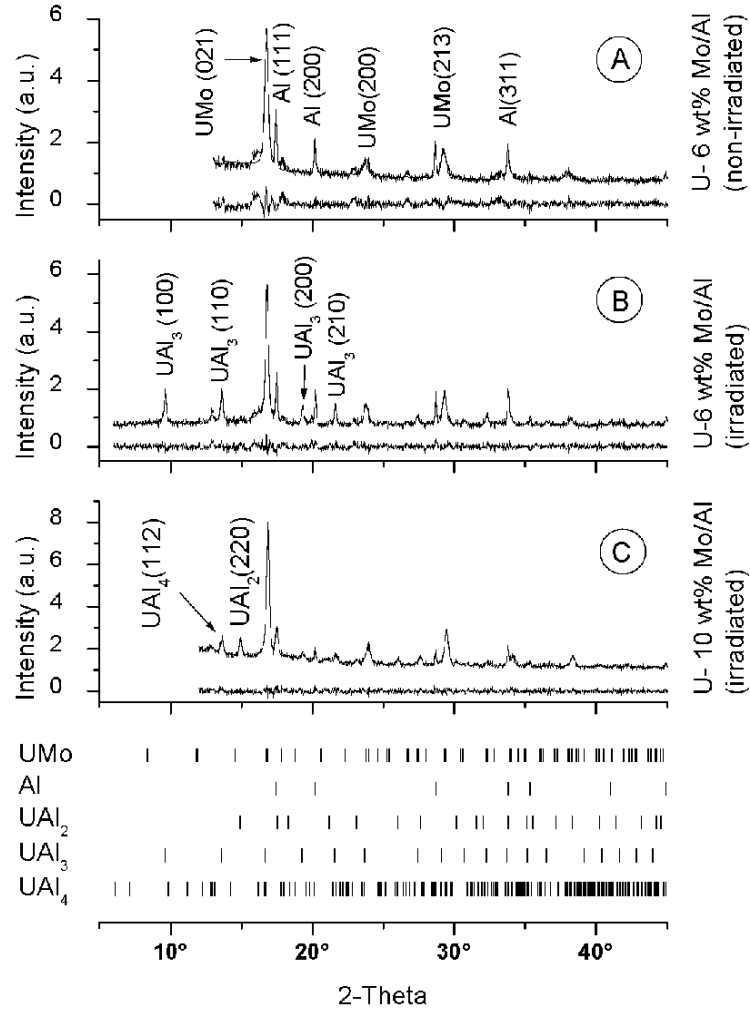


Figure 4.13: X-ray powder diffraction measurement and multiphase Rietveld analysis of a non-irradiated U-6wt%Mo/Al specimen (A), an irradiated U-6wt%Mo/Al specimen (B) and an irradiated U-10wt%Mo/Al specimen (C). The difference between the observed and calculated data is depicted around the zero intensity line. Reflection positions of the identified phases are shown in the lower part.

Table 4.3: Phase abundance in wt% of the heavy ion irradiated samples resulting from multiphase Rietveld analysis of X-ray powder data

Phase	Al wt%	γ UMo wt%	UAl ₂ wt%	UAl ₃ wt%	UAl ₄ wt%
Specimen					
U-6wt%Mo/Al	41.3±2.3	23.5±1.1	-	19.8±1.0	15.4±3.4
U-10wt%Mo/Al	27.7±1.2	36.3±0.8	11.0±0.4	13.4±0.5	11.6±1.8

4.3.2 Second diffraction measurement

While the first diffraction measurement showed that new crystalline phases are formed due to the irradiation with heavy ions, it provides no information about their spatial distribution. Therefore a diffractometer with a high spatial resolution is used for the second diffraction measurement.

A measurement with high spatial resolution requires either a high brilliance X-ray source or time, because for each single location a diffraction pattern has to be measured. Also, a very thin X-ray beam or a detector with a high spatial resolution is important as described in the introduction to this section. Here I follow the latter approach.

The very high intense X-ray beam is provided by the Deutsche Elektronen Synchrotron (DESY). Since the X-ray beam consists of a distribution of frequencies, the X-ray beam must be monochromated. This is achieved by a fixed-exit double-crystal monochromator. For intensity and practical purposes a wavelength of $\lambda = 1.54 \text{ \AA}$ was chosen. This wavelength corresponds to the wavelength of Cu K_{α} radiation. After the monochromator, the X-ray beam has a diameter of approximately 10 mm and will be reflected on the specimen and on the specimen holder, both are shown in Fig. 4.14 on the left hand side.

The high spatial resolution is achieved by a multichannel plate in front of a CCD detector as described in the introduction to this chapter on page 40. The thickness of the multichannel plate, that means the length of each channel, is 4 mm. Each channel has a diameter of $10 \mu\text{m}$ and the center to center distance between the channels is $12.5 \mu\text{m}$. Behind this multichannel plate a CCD detector is located (1000×1018 pixel, each $10 \times 10 \mu\text{m}^2$), which represents a 2-dimensional detector.

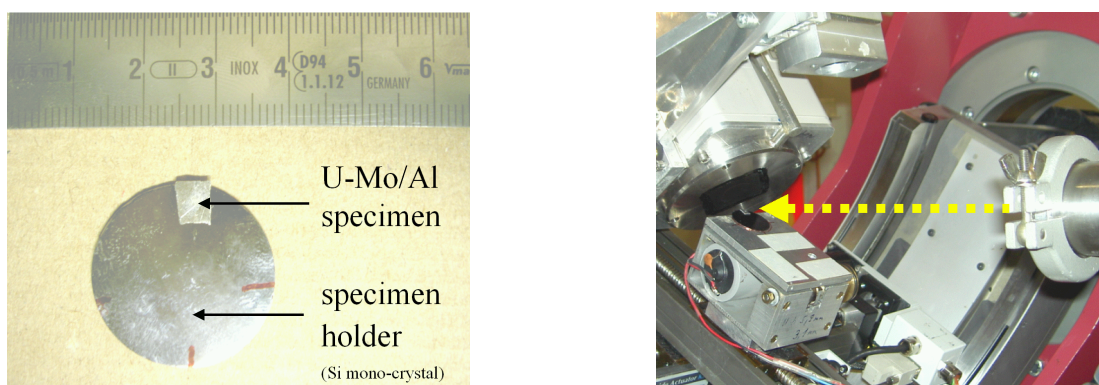


Figure 4.14: *Left hand side:* U-Mo/Al specimen on the specimen holder *Right hand side:* Experimental set-up. The yellow arrow indicates the X-ray beam from the beam tube in the direction to the specimen. The multichannel plate and the detector are located to the left above the specimen.

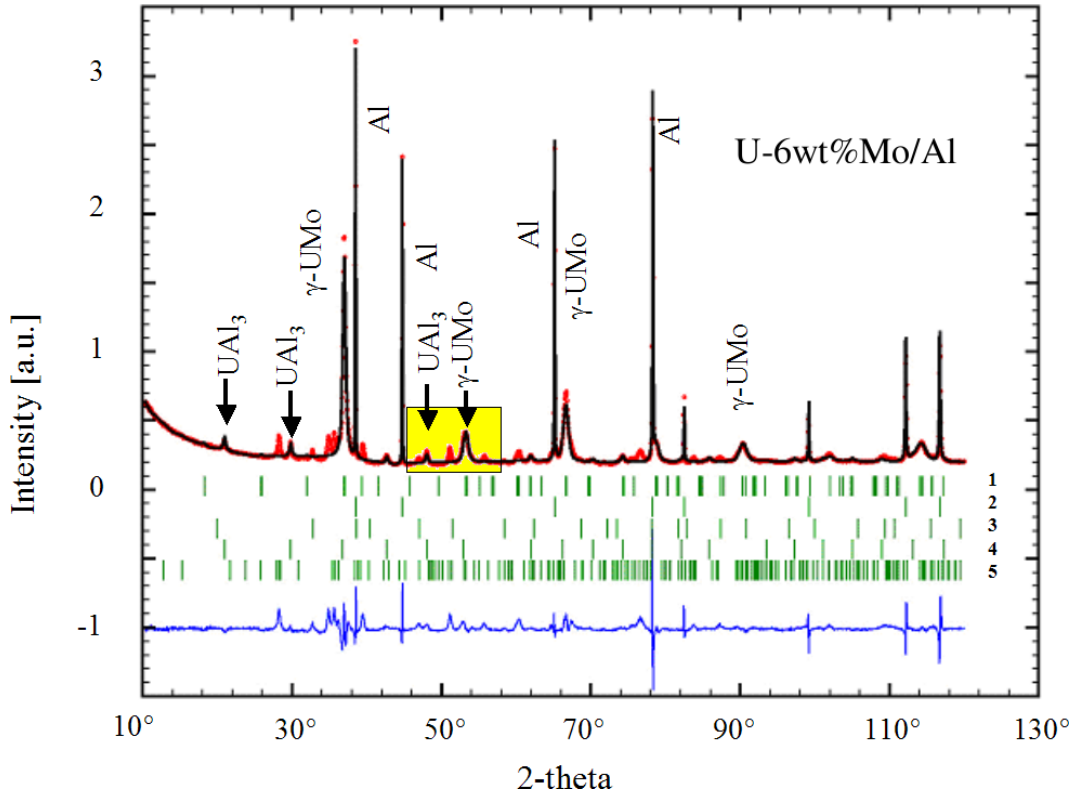


Figure 4.15: X-ray powder diffraction measurement and multiphase Rietveld analysis of an U-6wt%Mo/Al specimen (partly bombarded with heavy ion), same specimen as in Fig. 4.13 part B, the MAXIM-measurement has been carried out in the yellow region

Due to the multichannel plate each pixel of the CCD-detector receives photons exclusively from a small region of the specimen. Therefore 1000 x 1018 diffraction patterns are measured at the same time. This technique is called MAXIM. It allows a diffraction measurement with a high spatial resolution.

While the horizontal resolution is fixed with this technique, approximately $13 \mu\text{m}$ due to the distance between the specimen and the multichannel plate, the vertical resolution depends on the angle ϑ . In Fig. 4.12 one can see that the horizontal resolution is proportional to $13 \mu\text{m} \cdot (\sin\vartheta)^{-1}$. Further, the horizontal and the vertical resolution depend on the distance between the detector and the specimen. The closer the detector is to the specimen, the higher is the resolution.

Fig. 4.14 shows, on the right hand side, the experimental set up (experimental station G3 at the Hasylab in Hamburg, Germany). At the present time it is, in fact, the diffractometer with the highest spatial resolution in Germany. A detailed description of the instrument is given in [37, 38, 58].

In spite of the high brilliance of the synchrotron radiation, a MAXIM measurement for the whole angular region would require too much time to obtain a sufficient num-

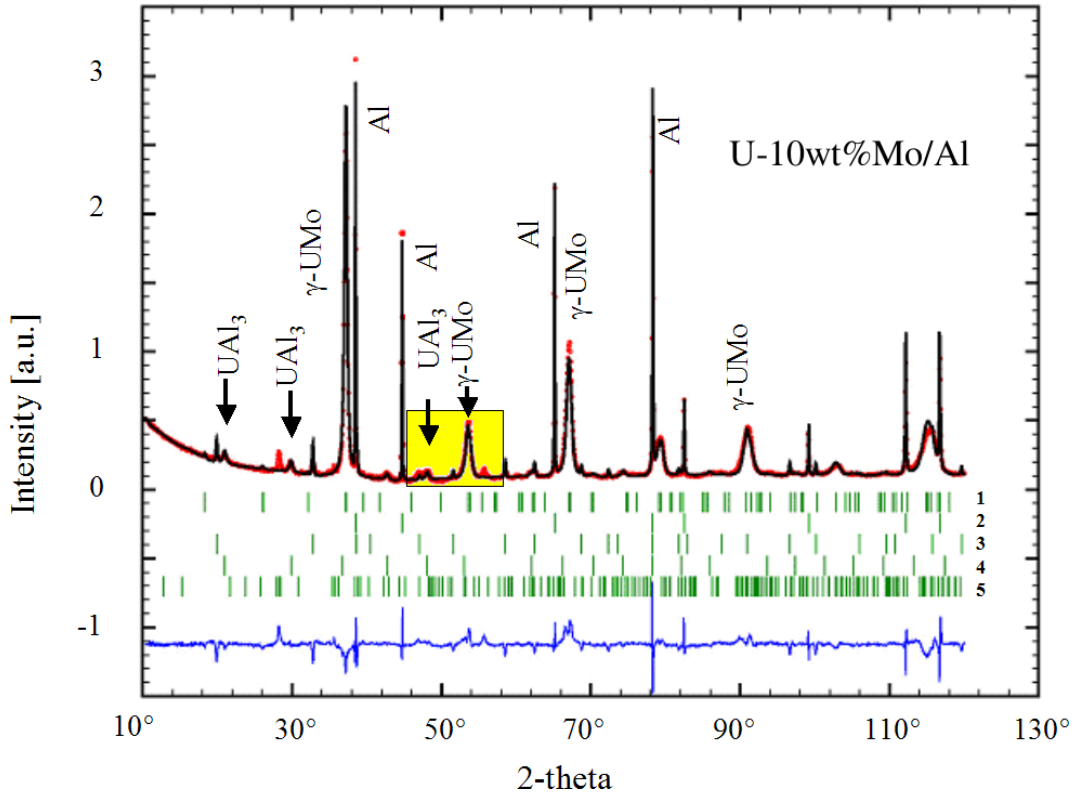


Figure 4.16: X-ray powder diffraction measurement and multiphase Rietveld analysis of an U-10wt%Mo/Al specimen (partly bombarded with heavy ion), same specimen as in Fig. 4.13 part C, the MAXIM-measurement has been carried out in the yellow region

ber of counts per pixel in the CCD detector. Therefore, first of all an overview scan is carried out, without a high spatial resolution, which means with a standard detector, and later a MAXIM measurement will be done only in an interesting angular region.

As described in the introduction to this chapter on page 40, two specimens are examined. An overview diffraction pattern for each specimen was taken in the region $10^\circ \leq 2\theta \leq 120^\circ$. The measurement required 12.7 h (U-6wt%/Al specimen) and 8.5 h (U-10wt%/Al specimen). Hereby the collected number of data points is even much higher than for the first diffraction measurement. The results of this measurement are shown in Fig. 4.15 and Fig. 4.16 for the U-6wt%/Al and the U-10wt%/Al (measured data in red, simulated data in black).

Compared to the first diffraction measurement a significant improvement of the signal to noise ratio, and therefore a higher quality of data is obvious. Beside the reflections from γ U-Mo and aluminum, other crystalline phases are present. Reflection positions of the identified phases are shown in the lower part for U-Mo in the metastable γ -phase (denoted as γ UMo in the pattern or as number 1 for the reflection positions), for aluminum (2), UAl_2 (3), UAl_3 (4), and UAl_4 (5).

Relative peak heights are different, compared to the first diffraction measurement. The reasons are on the one hand that the whole specimen is measured (irradiated and non-irradiated areas) and on the other hand that the specimen was not revolving during the measurement, therefore high texture effects, especially from the aluminum, are not suppressed. For low angles ϑ a direct view for the synchrotron radiation to the detector is possible, therefore the number of measured data points is increased.

Unlike the first diffraction measurement, only UAl_3 as a new crystalline phase is unambiguously identified, beside the γUMo and the aluminum phase. An UAl_2 phase is questionable, since some reflections are missing and an UAl_4 phase was not evidenced. Possible reasons are that the specimen was not revolving during the measurement, therefore high texture effects are not suppressed, or the different penetration depths of the used wavelength compared to the first diffraction measurement. Furthermore, presumably two additional crystalline phases exist in both specimen.

A MAXIM measurement has been carried out in the region from $46^\circ \leq 2\vartheta \leq 58^\circ$ - this region is shown in a yellow frame in Fig. 4.15 and Fig. 4.16. It was chosen, since there are two unambiguous peaks from well known phases (γUMo and UAl_3) and peaks resulting from unknown phases. The measurement required 7 h for the U-6wt%/Al specimen and 6.5 h for the U-10wt%/Al specimen.

After the measurement, the obtained multidimensional diffraction pattern were cut to a spatial region of interest. This is necessary since the detector area, which corresponds to the measured area, is much larger than the specimen. The obtained diffraction patterns (each pixel in the CCD-detector took one diffraction pattern, obtained from a very small region from the specimen due to the multichannel plate) are split by a computer program into twelve spectra, denoted as classes. These classes are shown in Fig. 4.18 for the U-6wt%/Al specimen². If we would add all these classes, we would obtain the yellow box in Fig. 4.15 again. At approximately 52° a little gap occurs in all classes, which can be ignored, since it is an artifact from the analysis of the data. Comparison of the twelve classes with the known phases reveals for instance that class number 10 (shown in red) is the UAl_3 phase.

Splitting of all the diffraction pattern, which were obtained per pixel in the CCD-detector, into these twelve classes, reveals in which part of the specimen which class is present. This yields in a two dimensional picture of the specimen for each of the twelve spectra, showing where and which class has been observed. These two-dimensional pictures are shown in Fig. 4.17. *Attention - this figure is shown before the classes in Fig. 4.18 due to space reasons.*

As described in the introduction to the MAXIM measurement, the spatial resolution of the picture is difficult to define, since it depends on the angle. However on some

²Classes and appropriate class-maps for specimen U-10wt%/Al are presented in the Appendix C.

pictures one can recognize the irradiated part - looks like a diamond on a playing card - and has the dimension of approximately $2 \times 2 \text{ mm}^2$.

A comparison of the twelve classes reduces the effective number for both specimens together to only eight different categories. This grouping of the classes to categories is shown in Tab. 4.4. Of course, two categories/phases have been re-found, UAl_3 and $\gamma\text{U-Mo}$.

Now each category can be given a different color and can be drawn together in one map. Such a map is shown in Fig. 4.19 for the specimen U-6wt%Mo/Al (left hand side) and U-10wt%Mo/Al (middle). Each map shows the part of the specimen, which contains completely the irradiated part of the specimen. The irradiated part, is surrounded by a non-irradiated area. Therefore yellow spots, which shows where the γUMo phase has been observed, can be found in the whole map, but only the irradiated part contains UAl_3 , red in Fig. 4.17, and as shown in Tab. 4.4 category A is class 10).

The two non-identified phases are between the irradiated part and the non-irradiated one or appear as background.

Table 4.4: Grouping of the classes to categories, also shown with colors on the following two pages

Category	Classes of the U-6wt%Mo/Al specimen	Classes of the U-10wt%Mo/Al specimen	Phase
A	10	2	UAl_3
B	3	-	
C	0	4,7	
D	4,8	1,3	$\gamma\text{U-Mo}$
E	2,5,11	-	
F	1,6,7,9	-	
G	-	0,6,8,9	
H	-	5,10,11	

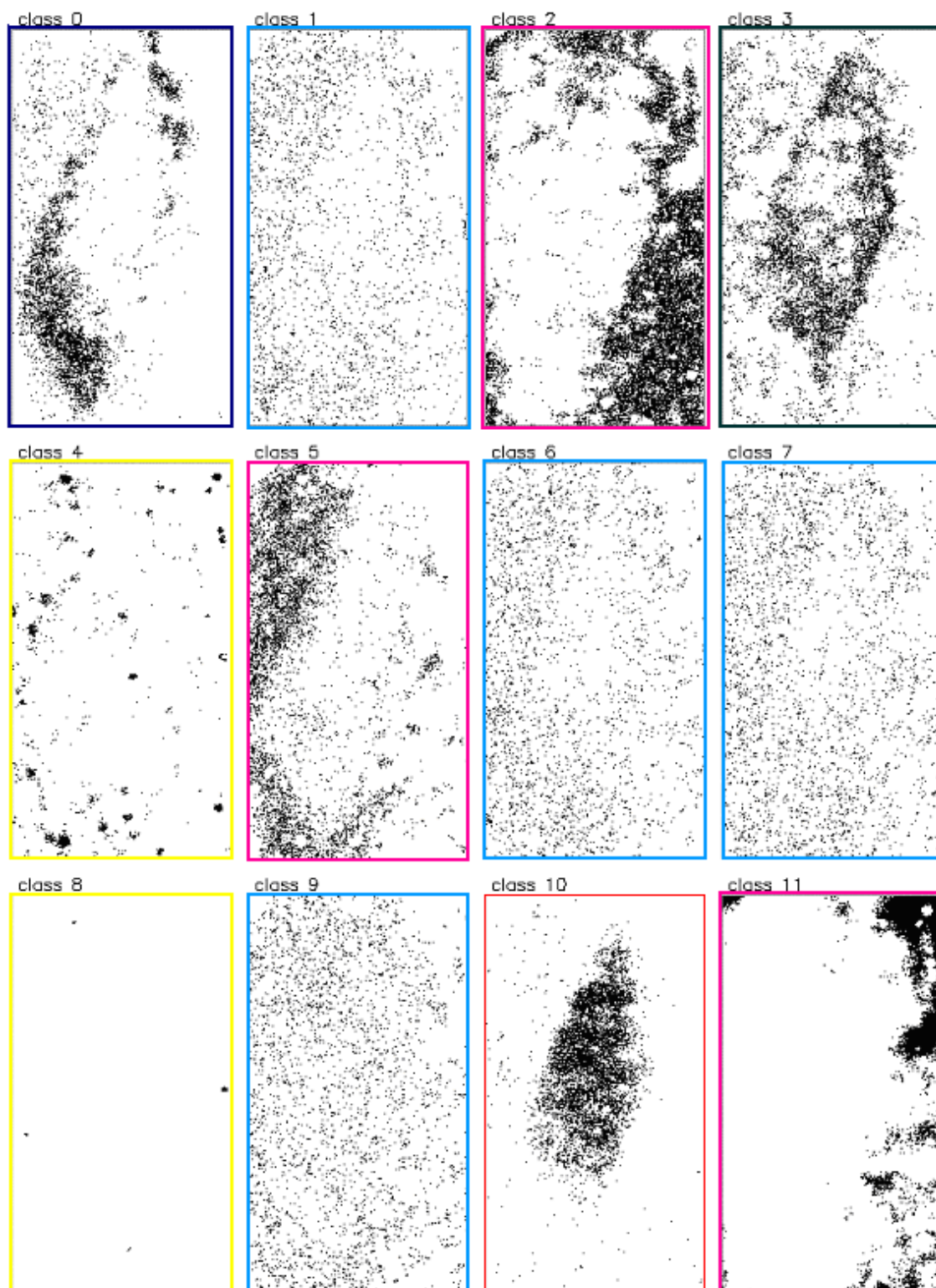


Figure 4.17: Two dimensional maps of classes of specimen U-6wt%Mo/Al.

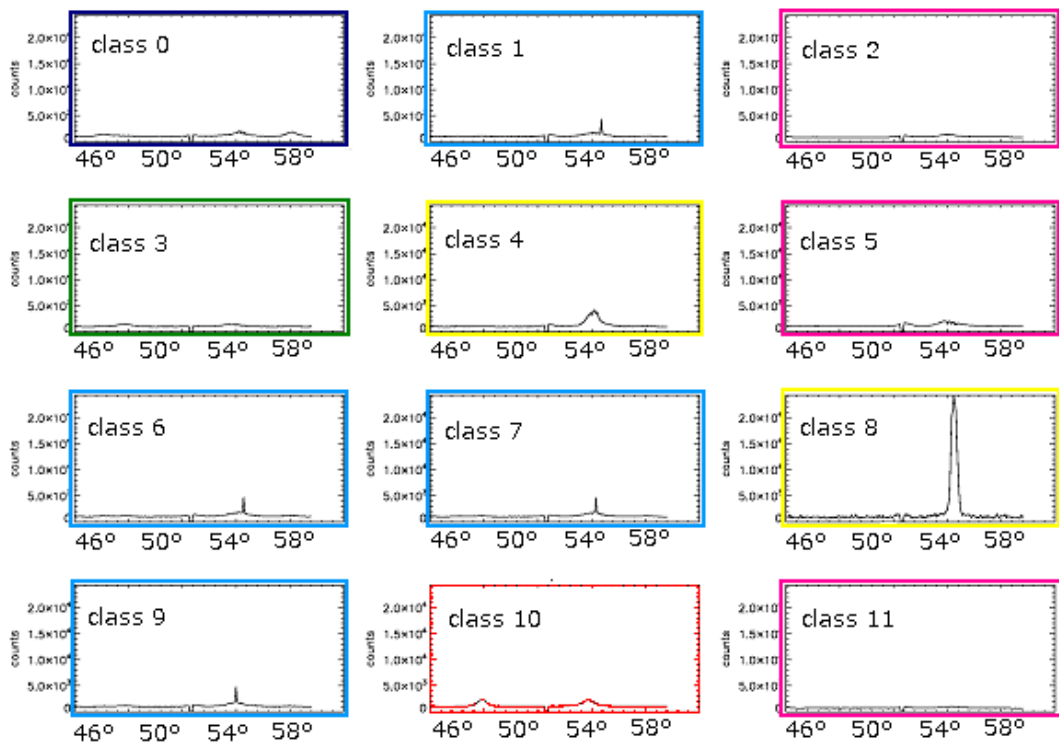


Figure 4.18: All twelve spectra from classification of the MAXIM-measurement for the U-6wt%Mo/Al specimen, each spectrum represents one class in Fig. 4.17

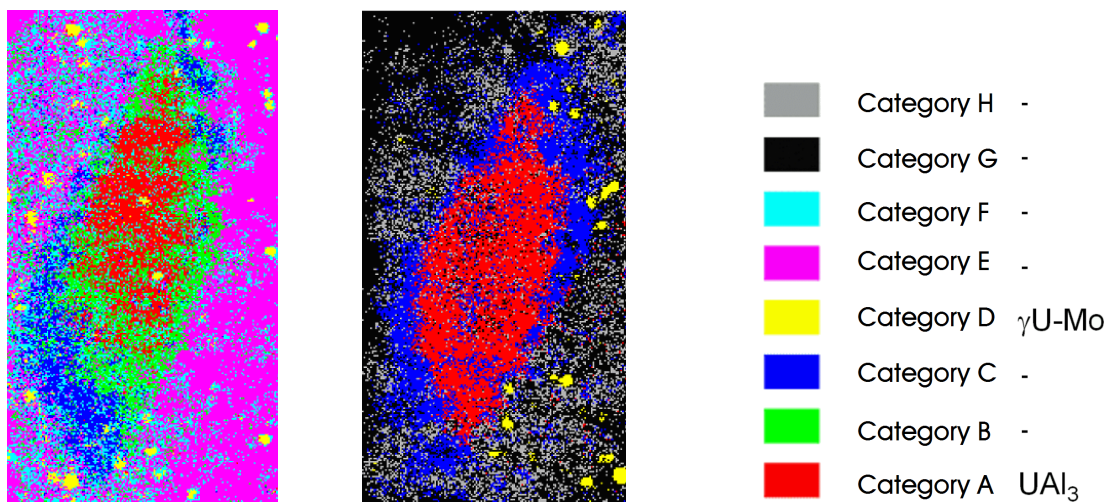


Figure 4.19: Map of reduced classified phases for the U-6wt%Mo/Al (left hand side) and the U-10wt%Mo/Al (middle) specimen

Chapter 5

Discussion

In this chapter I would like to discuss heavy ion irradiation as a method of simulating in-pile irradiation. Therefore I compare both methods and their PIEs of specimen which were either bombarded with heavy ions or in-pile irradiated. Hereafter the cause of build up of the interdiffusion layer will be discussed. And last but not least, the limits of the heavy ion bombardment will be highlighted.

5.1 Comparison of heavy ion to in-pile irradiation

The comparison of in-pile tests starts with a description of the specimen. This section follows the irradiation conditions. Finally the results of the PIE will be compared.

Specimen preparation

A detailed specimen description for heavy ion bombardment was given in section 3.1 and for in-pile irradiation in section 2.3.2. Since the specimens for heavy ion bombardment were cut out of specimens which have been manufactured for in-pile irradiation, the specimen are equal except for the outer dimension. One could assume that the surface of the polished specimen is oxidized, but EDX showed no evidence of oxygen, and also no uranium oxide was found by diffraction. Nevertheless, during the bombardment with heavy ions a possible oxygen layer on the surface would be sputtered away anyway (compare Fig. 2.6). Therefore oxidation is of no concern.

Irradiation conditions

Already in section 3.3 irradiation conditions for heavy ion bombardment were described. It was also pointed out that all conditions are as close as possible to in-pile irradiation. Therefore only three relevant parameters will be compared to in-pile irradiation in this section.

Tab. 5.1 and Tab. 5.2 show three parameters for heavy ion bombardment and French in-pile irradiation experiments¹ [13]. At first, both tables show the effective

¹While the first in-pile experiment (IRIS-I) reached the final burn up, the latter two had to be

Table 5.1: Parameter of heavy ion bombardments

Experiment at	Position 2	Position 3
Effective duration	13 h	4 h
Maximum temperature of the meat	200°C	170°C
Average ion density in the meat	$2.2 \cdot 10^{20}$ ion/cm ³	$5.6 \cdot 10^{20}$ ion/cm ³

Table 5.2: Parameter of French in-pile irradiation experiments [13]

Experiment	IRIS-I	IRIS-II	FUTURE
Effective full power days	240 d	60 d	40 d
Maximum cladding temperature at BOL	75°C	100°C	130°C
Average fission fragment density in the meat	$4 \cdot 10^{21}$ ion/cm ³	$2.4 \cdot 10^{21}$ ion/cm ³	$2 \cdot 10^{21}$ ion/cm ³

duration. For a heavy ion bombardment the effective duration is equal to the beam time on the accelerator. But for in-pile irradiation, reactor breaks have to be taken into account. Additional time for both experiments is necessary for preparation of the irradiation. After the irradiation, in-pile irradiated specimen require a decay time for easier handling and transportation, since the specimen are strongly activated. Consequently in-pile experiments require much more time, man-power, and bureaucracy (since enriched uranium is required), therefore they are also much more costly than a heavy ion bombardment.

The next given value for both types of irradiation is the temperature. While for heavy ion bombardment the meat temperature is given, for in-pile irradiation the cladding temperature is given. Taking Fig. 2.8 part D on page 23 and uncertainties into account, it can be concluded that both temperatures are in a similar range.

The last value (ion density) is the most difficult one to compare. As described in section 3.3 the maximum heavy ion (= fission fragment) density can easily be a factor of 10 higher than the average value due to the high kurtosis of the ion distribution. However, also the fission fragment density will be a factor of two higher in the fuel

stopped before the final burn-up was achieved due to a breakaway swelling of the plates. Therefore the effective duration for irradiation was lower.

grains than in the meat layer, due to the volume loading (approximately 55 vol%). Therefore I can conclude that both are of the same order of magnitude.

Comparison of the PIEs

In order to validate the method, each result of the PIE will be compared individually for heavy ion bombarded specimen and in-pile irradiated specimen.

Optical microscopy

Fig. 5.1 shows on the left hand side an optical image of a heavy ion bombarded U-6wt%Mo/Al specimen (irradiated to a fluence of $1 \cdot 10^{17}$ ion per cm^2). On the right hand side an optical image of an in-pile irradiated specimen is shown [41]. Both images show spherical U-Mo particles surrounded by an interdiffusion layer and the aluminum matrix. In both images all three phases are separated by distinct borders. The thickness of the interdiffusion layer is between 20 and 30 μm . Compared with the simulation in section 2.3, this value is slightly higher. Differences between the two images are the color of the fuel particles and the roughness of the surface. The reason for the differences is that the image for the heavy ion irradiated specimen was taken immediately after the irradiation. This means that on the one hand there was no treatment like polishing, and on the other hand there was almost no time for oxidation, therefore the fuel has no black color.

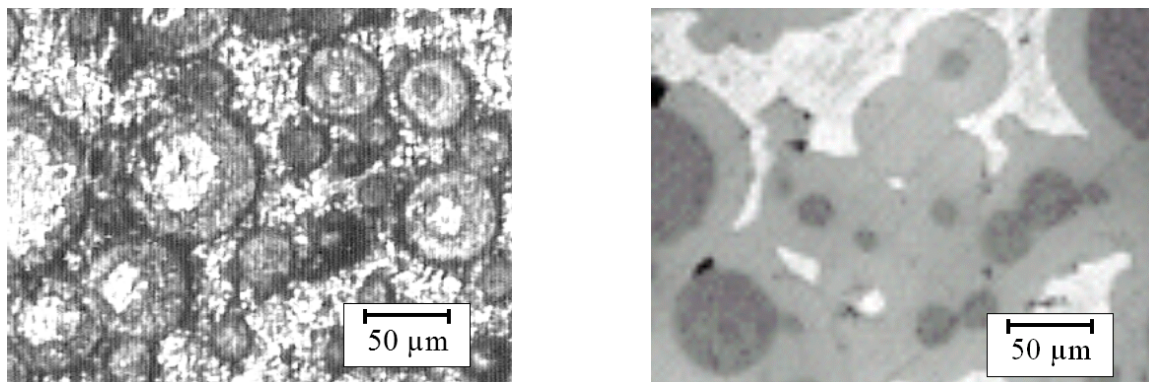


Figure 5.1: *Left hand side:* Heavy ions irradiated U-Mo/Al specimen *Right hand side:* In-pile irradiated U-Mo/Al specimen - taken from [41]

Scanning electron microscopy

Like the optical images, the SEM-images of the heavy ion and the in-pile irradiated specimens are similar. Both images are shown in Fig. 5.2. Differences occur especially on the fuel particles. On the heavy ion irradiated fuel particle are ripples, they are an irradiation effect, which is for instance described by [36] for U_3Si fuel. For the in-pile irradiated specimen small cracks are shown in the fuel particles. Reasons for these cracks are, for instance, fission gases, which can not be simulated by a heavy ion bombardment.

While the thickness of the interdiffusion layer around a fuel particle is for in-pile irradiated specimen more or less constant, for heavy ion bombarded specimen, the thickness depends on the direction of the irradiation. As described in section 3.3 at position B in Fig. 5.2 (left hand side) a simulation of in-pile irradiation is possible. Here the thickness of the interdiffusion layer is reduced (approximately $10 \mu m$), presumably due to the lower penetration depth of the heavy ions into the fuel particle.

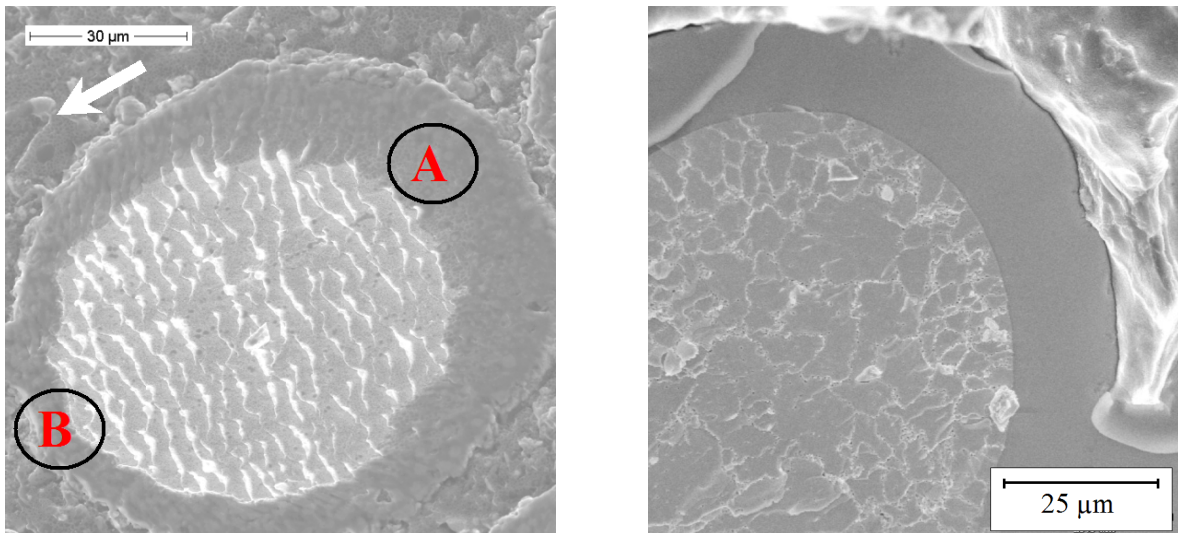


Figure 5.2: *left hand side*: Heavy ion irradiated U-Mo/Al specimen, the arrow marks the direction of the incoming heavy ion beam, and the position A and B corresponds to Fig. 3.7. *right hand side*: in-pile irradiated U-Mo/Al specimen - taken from [41]

Energy dispersive X-ray analysis

For in-pile irradiated specimens the chemical composition of the interdiffusion layer has been identified as $(U-Mo)Al_x$, where x ranges from 3 to 4.4 [29, 51, 50]. Even $x = 7$ was reported in [52]. For heavy ion irradiated specimen however, the parameter x depends on the position in the interdiffusion layer, but is in the range between 2 and 4. The reason for the lower aluminum content (this means that the uranium content is higher as for in-pile irradiated specimens) could be the missing burn-up of the uranium during heavy ion bombardment as compared to in-pile irradiation.

Diffraction measurements

In the year 2006 neutron powder diffraction measurements of in-pile irradiated and non-irradiated low-enriched U-Mo/Al dispersion fuel were reported in [53]. The measurements revealed that new crystalline reaction products are formed under in-pile irradiation (UAl₃). Tab. 5.3 shows the quantitative and qualitative composition of the specimens. Further, the table shows that there were UO₂ and uranium in the α -phase present before the in-pile irradiation took place. After the irradiation these phases have disappeared.

However, the post in-pile irradiation data can be compared with Tab. 4.3 on page 42. Now, one can recognize that after the irradiation the quantities of the phases vary, but qualitative they are equal. In both cases five crystalline phases are evidenced: Al, γ UMo, UAl₂, UAl₃, and UAl₄. Hereby UAl₃ is the dominant new phase. The difference in the quantity of each phase could be due to the different burn-up/fluence and temperature during irradiation. Also, one has to take into account that X-rays can reach deeper into the specimen than heavy ions - compare Tab. 4.2 and the irradiation angle of the heavy ion beam and the X-ray beam. Therefore irradiated and non-irradiated layers are examined at once by X-ray diffraction on heavy ion bombarded specimens. This is not the case for in-pile irradiated specimens, since here the whole specimen is irradiated. Therefore a diffraction measurement can be accomplished in Debye-Scherrer Geometry (transmission). Here neutrons can penetrate completely through the specimen, and only irradiated fuel or fresh is examined in one measurement.

In conclusion, both ways of irradiation of the specimens (in-pile and with heavy ion) leads to the same qualitative composition.

Table 5.3: Phase abundance of fresh fuel and in-pile irradiated specimen, examined with neutron diffraction by [53], appropriate data for heavy ion bombarded specimen are presented in Tab. 4.3 on page 42

Phase	Al wt%	γ UMo wt%	UO ₂ wt%	α U wt%	UAl ₂ wt%	UAl ₃ wt%	UAl ₄ wt%
Specimen							
U-10wt%Mo/Al (non-irradiated)	36.5	60	1.5	2	-	-	-
U-10wt%Mo/Al (non-irradiated)	27	67	3	4	-	-	-
U-10wt%Mo/Al (irradiated)	8	24	-	-	1	63	4

Annotation: Since α -Uranium and UO_2 disappear under in-pile irradiation condition, but the metastable γ -phase of the U-Mo alloy is still remaining, the local temperature in the meat must exceed 600°C significantly, compare Fig. 1.3. Only in such a high temperature region the γ -phase exist as a stable phase. Nevertheless, all phases will be destroyed due to the high number of displacements, but the γ -phase will be retained in such a high temperature region. Since such a high temperature can not be reached according to the simulations in section 2.2.4 and section 2.3, the thermal conductivity and diffusivity seems to be overestimated, especially for in-pile irradiated fuel. A more precise discussion will be later on page 58 in the frame of the electronic thermal spike model as an explanation for the growth of the IDL.

5.2 Cause and prediction of the interdiffusion layer

Section 5.1 has shown that the physical properties of the radiation damages by heavy ion bombardment and in-pile irradiation are very similar. Especially the interdiffusion layer occurs in both types with similar properties. Now this section will describe possible causes of this layer. A model for prediction of the interdiffusion layer thickness based on the causes will be given.

Up to now, the new layer between the fuel grains and the matrix was denoted as “interdiffusion layer”. This is reasonable, because a mixture of elements took place, e.g. a transport phenomena. This name implies a diffusion process as the driving force and one might assume that all diffusion processes can be described by Ficks first and second law. Both are given by Eq. 5.1 and Eq. 5.2.

$$j = -D \cdot \nabla C \quad (5.1)$$

$$\frac{\partial C}{\partial t} = -div j = D \cdot \nabla^2 C \quad (5.2)$$

That means, the particle flux j is proportional to a diffusion coefficient D and to the gradient in a concentration C (First Ficks law). Taking the equation of continuity into account, the second Ficks law follows. Both equation are based on a statistical random walk concept and describe simple diffusion mechanism (vacancy or interstitial diffusion). Therefore the diffusion coefficient D depends only on lattice parameters and the temperature T (see Eq. 5.3).

$$D = g_l \cdot a^2 \cdot \nu_0 \cdot \exp\left(-\frac{H_M}{k_B \cdot T}\right) \quad (5.3)$$

With g_l as lattice factor of the order of 1, a is the lattice constant, ν_0 is the vibration frequency of the diffusing particle (roughly 10^{13} s^{-1}) and H_M is the activation energy of migration (in common crystals about 0.5 - 5 eV)[24].

For more complicated mechanism as described above, Ficks law cannot be applied without suitable correction. Such modifications have to be done for radiation induced diffusion. Therefore possible causes of particle mixing will be discussed, dealing with correction of Ficks law:

- **Thermal diffusion**

Fig. 4.1 (optical image) and Fig. 4.5 (SEM-image) showed only in the bombarded area an interdiffusion layer. Nevertheless, due to the high thermal conductivity of the specimen (especially of the aluminum matrix), the same temperature in the bombarded and non-bombarded area can be assumed. But no interdiffusion layer is observed in the non-bombarded area. This knowledge alone is sufficient to exclude a thermal diffusion as an important cause for the interdiffusion layer. Furthermore many thermal diffusion tests have been carried out worldwide [40, 42, 43] at very high temperatures, because thermal diffusion obeys an

Arrhenius law. Also several days of annealing are required.

On the one hand it is difficult to compare the obtained data with burn-up values of in-pile irradiated fuel, and on the other hand a decomposition of the metastable γ -phase has been observed due to the high temperature. Also the thermal diffusion exhibits an IDL consisting of a layer system with three different, and separated phases. These properties are in contrast to the in-pile irradiated specimens. Therefore I exclude a thermal activated diffusion process as the main cause for the interdiffusion layer.

- **Electronic thermal spike model**

The electronic thermal spike model was described in section 2.2.4 in the frame of temperature considerations. In spite of the lack of important data like the thermal diffusivity D_e , a local melting along the trace is not likely for fresh fuel. Furthermore Fig. 2.7 implies a maximum local temperature increase of about 100-200 K (in the lattice). This temperature increase would not be sufficient to reach the γ -phase region of the U-Mo alloy. However, during the bombardment with heavy ions or in-pile irradiation, parameters - like the thermal diffusivity or conductivity - will change. This is reasonable, since the defect concentration increases during burn-up and the mobility of free electrons and phonons is hampered, which carry the "heat" in solid bodies. Assuming a decrease in the thermal diffusivity and conductivity due to the very high defect concentration, the local temperature can rise up to the γ -phase region. Since the specimen is quenched to the global temperature of the specimen immediately after each single bombardment, the γ -phase is conserved or even restored. This model could explain why no α -uranium was observed after the in-pile irradiation or heavy ion bombardment (compare Tab. 5.3), in spite of its existence before irradiation. Therefore I assume that a dramatic decrease in the thermal diffusivity occurred during irradiation, but as a cause for mixing of elements it should be excluded.

- **Direct collision**

On page 15 it was shown that in average $1 \cdot 10^5$ displacements per fission fragment take place. These displacements take place at the end of each projectile history - mainly in the last micrometer. This means for a fluence of 10^{17} ion per cm^2 that each atom in a thin layer of $1 \mu\text{m}$ thickness must be moved approximately $2 \cdot 10^3$ times in average (see Eq. 5.4). Hereby an atom density of $4.9 \cdot 10^{22}$ atoms per cm^3 for U-6wt%Mo and $6.0 \cdot 10^{22}$ atoms per cm^3 for aluminum was assumed.

$$\frac{\text{displacements}}{\text{target atom}} = \frac{\text{displacements per projectile} \cdot \text{fluence}}{\text{number of target atoms}} \approx 2 \cdot 10^3 \quad (5.4)$$

Furthermore each recoiled atom acquires up to 100 eV, which is sufficient for moving a range of 15 \AA . This means that a single atom can move a distance of $3 \mu\text{m}$. Since this distance is three times the thickness in which displacements are possible, a heavy ion bombardment under an inclined angle is important. Taking uncertainties and a movement of atoms in both directions (uranium and

molybdenum into aluminum and vice versa) into account,
direct collision contribute significantly to the growth of the interdiffusion layer.

- **Coulomb explosion**

This model starts with a high ionized area along the trace of the projectile. For the case in which the resulting positive potential can not be compensated due to the hampered mobility of vacancies or electrons (because they are trapped), a repulse of the ionized atoms is possible. This phenomena is called Coulomb explosion. A necessary condition for a Coulomb explosion is [24]:

$$\frac{q_i^2(t) \cdot e^2}{\epsilon \cdot a_0^4} > \frac{E}{10} \quad (5.5)$$

Where $q_i(t)$ is the mean level of ionization, E is the elastic modulus, and a_0 is the Bohr-radius. Furthermore, the time of neutralization must exceed the time of diffusion of the target ions (10^{-14} - 10^{-13} s). Consequentially it follows that the density of the free electrons in an insulator or semiconductor (without electrical field) is:

$$n_e < \frac{e \cdot n_a}{\pi \cdot a_0 \cdot \mu_e \cdot k_B \cdot T \cdot t} \quad (5.6)$$

Hereby n_a means the number of ionizations per atom layer and μ_e the mobility of the electrons. In metals a rapid neutralization is expected due to the return of the electron gas (plasma oscillation).

The time for neutralization of a mean excitation corresponds to the inverse plasma frequency ω_p :

$$t < \frac{1}{\omega_p} \quad (5.7)$$

Since the plasma frequency in metals is of the order of 10^{15} s⁻¹,
a Coulomb explosion can be excluded in metals.

The only possible cause for the build up of the IDL seems to be caused by direct collisions. All other possibilities are unlikely. In order to test this model an irradiation has been carried out at an angle between heavy ion beam and the surface of the specimen of $\alpha = 45^\circ$, this means 15° steeper than in the other presented bombardments). Therefore displacements occur deeper in the meat layer and not on the surface. All other parameters were maintained, this means that an irradiation by iodine took place at approximately 200°C. At a fluence of $1 \cdot 10^{17}$ ion per cm² no IDL was visible with an optical microscope and the bombardment was continued up to a final fluence of $5 \cdot 10^{17}$ ion per cm². SEM images of this specimen are shown in Fig. 5.3. The images show no IDL on the surface of the specimen, but ripples on the fuel particles. EDX-measurement, carried out at the encircled numbers in the Fig. 5.3 right hand side, revealed also no mixture of elements (i.e. no IDL visible on the surface).

Consequently I conclude that displacements are the driving force for the build up of the IDL. Therefore the thickness of the IDL depends on the number of displacements

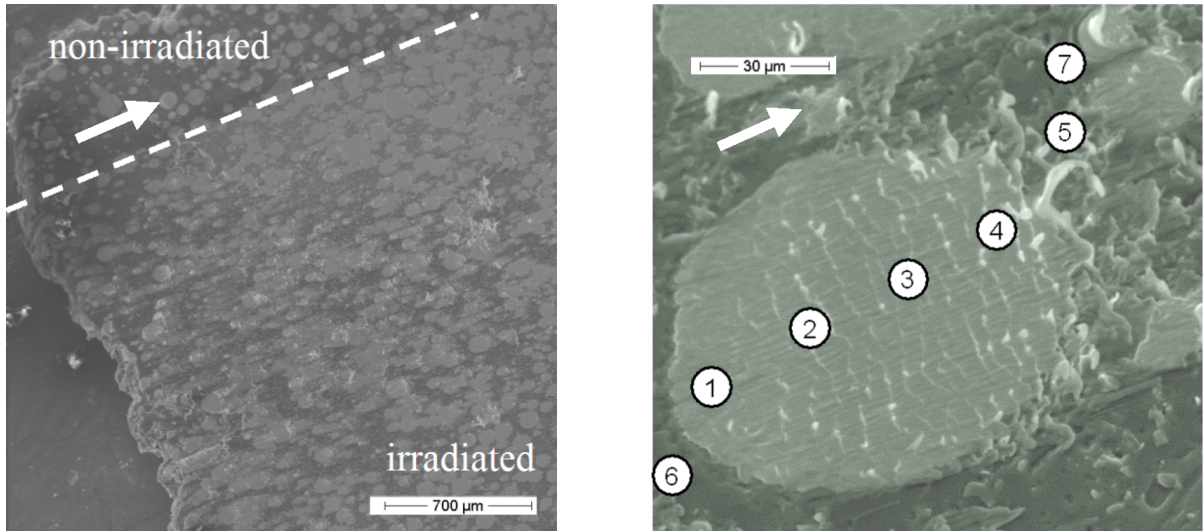


Figure 5.3: SEM images of an U-6wt%Mo/al specimen partly irradiated under 45° with two different magnifications, the encircled numbers on the right hand side indicate positions where EDX-measurements have been carried out.

per target atom and the range of the recoiled target atoms. Hereby the number of displacements per target atom is the number of displacements per projectile multiplied with the fluence and divided by the effective thickness of the region where displacements are likely to occur (FWHM of the recoiled ion distribution times $\sin \alpha$) and the atom density. A weak temperature dependence is due to the temperature dependence of the displacement energy, which affects the number of displacements per projectile. Since much more displacements take place in the fuel particles than in the aluminum matrix (for instance ≈ 177.000 to ≈ 60.000 as shown in section 2.5 on page 15) per projectile, the IDL growth is favored in the direction from the fuel particle into the aluminum matrix and particularly pronounced in the direction of the irradiation, see Fig. 5.4. This figure shows also position A and B, known from Fig. 3.7 and Fig. 5.2.

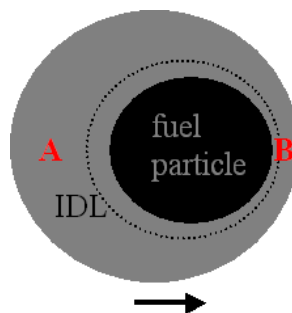


Figure 5.4: Sketch of an irradiated fuel particle. The dotted line shows the interface between the fuel particle and the matrix before the heavy ion bombardment took place.

In order to compare heavy ion bombarded specimens with in-pile irradiated specimens, the geometry, e.g. the variation of the fission fragment density, has to be taken

into account. An expression for the growth rate of the IDL was found by Hofman for U_3Si_2/Al and $U-Mo/Al$ fuel. The thickness of the IDL y is expressed as [15]:

$$y(cm) = \sqrt{5.07 \cdot 10^{-26} \cdot FFD \cdot e^{-\frac{65420}{R \cdot T}}} \quad (5.8)$$

Hereby FFD denotes the fission density in the fuel particles itself (fission rate \dot{f} · time t).

Using equation 5.8 and assuming a specimen, which was irradiated at 200° C and has an IDL thickness of 20 μm , as shown in chapter 4, this would correspond to a FFD of $2 \cdot 10^{22}$ fission per cm^3 (calculated with Eq. 5.8). Such a burn-up value is not possible with LEU specimen, since the fission density would be much greater than the ^{235}U atom density. However, this value corresponds to a heavy ion bombardment to a fluence of $1 \cdot 10^{17}$ ion per cm^2 .

5.3 Limits of heavy ion irradiation

In this section I would like to discuss the limits of the heavy ion irradiation of U-Mo/Al fuel. In particular two different limits have to be observed. The first limitation is caused by the difference between in-pile irradiation and heavy ion bombardment (limits of the method). For instance fission gases can not be simulated by a bombardment with iodine. The second limit will deal with the limit of the U-Mo/Al fuel under bombardment condition. Since the resistance against this kind of irradiation is a basic requirement of nuclear fuels, this limit will mark an upper limit for in-pile irradiations.

5.3.1 Limits of the method

Although only 0.5% percent of fission fragments are ^{135}I [49], ^{127}I simulates the radiation damage caused by fission fragment quite well as described in chapter 2. More complicated is the fact that some fission fragments are gases. For instance the fission of 1g ^{235}U releases 28 cm³ of fission gases, this leads to an enormous pressure inside the fuel [20]. Even a bombardment with noble gases would not simulate this pressure; since the bombardment takes place only on the surface, that means the noble gases would be released during the bombardment. Therefore the limits, which are caused by fission gases (very important for instance in U_3Si fuel), can not be investigated with this method.

Besides the radiation damages, which are caused by neutron-, β -, or γ -radiation, the burn-up effect has to be taken into account. This means the disappearance of uranium atoms. However, this effect could be quite well simulated, since sputtering of atoms takes place. It seems to be even overcompensated (compare Fig. 2.6), but in the discussion of the EDX-measurements, it was shown that the burn-up can presumably not be simulated due to sputtering (see section 5.1).

5.3.2 Limits of the UMo/Al fuel

Nevertheless, since the heavy ion bombarded specimen (and especially the interdiffusion layer) consists of binary alloys like UAl_3 which are already used in reactor fuels, there is no hint of an abnormal swelling of the U-Mo/Al fuel. But during the heavy-ion bombardment one of the specimens (U-6 wt% Mo/Al) was broken into at least four pieces. Fig. 5.5 shows an light-optical microscope image of one part of this specimen. Like the other specimens, it was irradiated by iodine, but the energy of the projectile was reduced to 80 MeV and the flux increased to $2.3 \cdot 10^{12}$ ions/s in order to reach higher deposition rates and to find the limits of the instrument, at which the specimen can be irradiated.

While a maximum temperature of less than 100°C was measured - much lower than for the others due to a better water-cooled specimen holder - the irradiated area was similar in size (0.9 x 3 mm²). After only 14 min, which corresponds to a fluence of 7.2

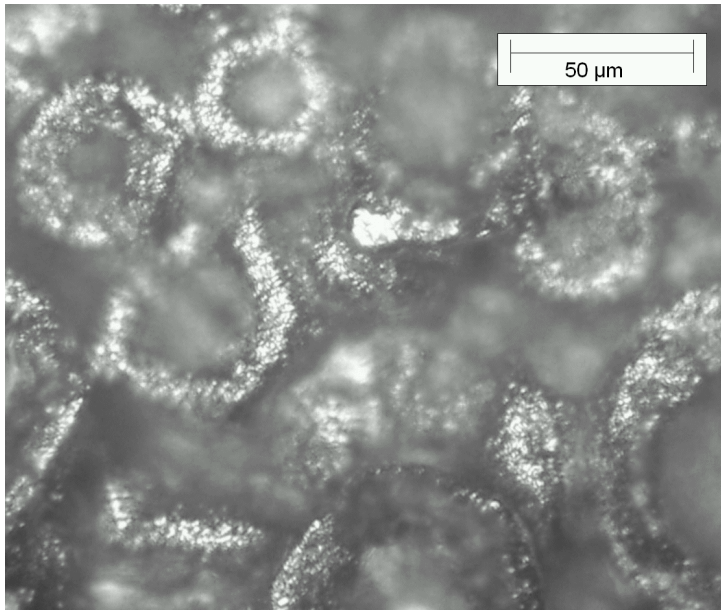


Figure 5.5: Optical image of a destroyed (over-irradiated) U-6wt%Mo/Al specimen.

· 10^{16} ion/cm², bombardment had to be stopped because the specimen was broken.

Optical microscopy of the broken parts revealed that there was a new protruding phase around each spherical fuel particle (instead of the IDL). These local elevations around the spherical fuel particles could be caused by either a volume increase of the interdiffusion layer, the fuel particles or a combination of both. As a reason for the swelling a transformation from crystalline to amorphous could be taken into account, because amorphous materials swell significantly under irradiation [36]. A first hint of such a transition was found in the XRD-pattern of the irradiated U-10 wt% Mo specimen which shows an amorphous hump under small angles (not shown in Fig. 4.13, since the origin of the hump is not absolutely clear, since a hump was also found for the non-irradiated specimen). Also the formation of ripples on the U-Mo particles indicates an amorphous surface. Such a transition from crystalline to amorphous was also discovered for U₃Si fuel for ion and in-pile irradiation [35]. The data are shown in Appendix A. Here the transition to amorphous can be delayed by annealing. This behavior can explain, why the specimen was destroyed at low and not at high temperature.

A further examination of the broken U-Mo/Al specimen may be difficult, since only small pieces are available for X-ray diffraction measurements, which could prove an amorphous phase. This model could show the reason for the abnormal swelling of the in-pile irradiated fuel plates.

Chapter 6

Summary

This thesis has introduced a new technique for testing U-Mo/Al dispersion fuels out of pile. Hereby the radiation damages caused by fission fragments are simulated by swift heavy ions. Also this technique avoids an activation of the specimen, which makes the handling much easier, and simulates days of in-pile irradiation in minutes, which saves time and money.

A theoretical background was given, followed by a description of the experimental set-up and bombardment conditions. Afterward the results of the PIEs are presented and compared to those of in-pile irradiated specimen. Hereby this thesis has concluded that the reason for the growth of the unfavorable interdiffusion layer in U-Mo/Al dispersion fuel is irradiation induced diffusion. This kind of diffusion is caused by fission fragments, and is marginally temperature dependent. Furthermore it was shown that the properties of the heavy ion bombarded specimen and in-pile irradiated specimen are not only comparable, even a similar irradiation failure has been reported. Therefore this technique should be standard, like annealing, before an in-pile irradiation test of new nuclear fuel candidates takes place.

Annotation:

Other promising nuclear fuel candidates were tested in a collaboration between CERCA, TUM and CEA. Specimens were manufactured at CERCA, heavy ion bombarded by TUM, and PIEs will be carried out at CEA-Cadarache. Since the PIEs are still underway, they are not mentioned in this thesis. Because first results of the PIEs are encouraging, the collaboration has still scheduled further bombardments with heavy ions. As soon as the results are available, they will be published.

Chapter 7

Outlook

Here two different outlooks will be presented: On the one hand the aspect of heavy ion bombardments and on the other hand that of a fuel which satisfies the requirement of a conversion of the FRM II reactor.

7.1 Outlook for heavy ion irradiation

Since this heavy ion bombardment is a new technique to examine nuclear fuels, it offers a great variety of opportunities. For instance different isotopes could be used for bombardment with various energies or irradiation angles. Also the temperature of the specimen can be varied. The interdiffusion should be monitored in situ with an optical microscope during bombardment in order to measure diffusion coefficients. Also further examinations of the specimens are much easier, for instance the measurement of the thermal conductivity, diffusivity and heat capacity of the bombarded specimen¹. All this data will allow us to obtain a further insight into nuclear fuel, which is necessary for finding its limits.

7.2 Outlook for a fuel for conversion of the FRM II

Due to the breakaway swelling observed at miniplates from Argonne National Laboratory and French full size plates during in-pile irradiation, U-Mo/Al dispersion fuel seems to be an unrealistic option for the conversion of the FRM II reactor from HEU (93 wt% enriched) to MEU (≤ 50 wt% enriched). Other possible options must be taken into account. At the moment three possibilities appear realistic:

- **Suppression of the interdiffusion layer**

Annealing experiments have shown that a thermal diffusion of the uranium into

¹As mentioned on page 58 a significant decrease in the thermal conductivity during irradiation is reasonable. A diploma thesis is underway to measure the thermal conductivity before and after the irradiation of the specimen, data will be published presumably in December 2006.

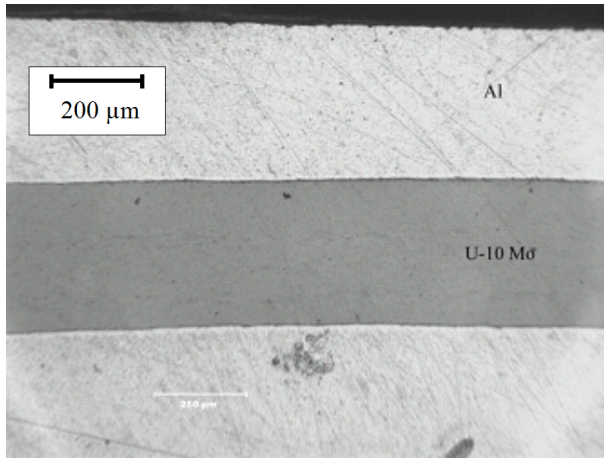


Figure 7.1: Optical image of an in-pile irradiated monolithic U-10wt%Mo specimen [41]

the aluminum can be reduced by additives like Si. Also heavy ion bombardment, showed similar results. At the moment, an addition of 2 wt% Si into the aluminum matrix seems to be a good choice. Another option is to replace the aluminum matrix by magnesium, which forms no intermetallic compound with uranium or to coat² the U-Mo particles. Unfortunately coating would reduce the volume fraction of fuel in the meat significantly and is therefore not favored.

- **Monolithic fuel**

Here a thin uranium-molybdenum foil is welded between two aluminum claddings. Since no aluminum is present in the meat layer, which is equal to the fuel in this case, no interdiffusion of U-Mo and aluminum in the meat is possible. The RERTR-team has irradiated two of these specimen in the frame of an irradiation program called RERTR 4. The meat layer was U-10wt%Mo, that means a uranium density of 15.2g U per cm³. The thickness of the round meat layer was 0.3 mm and the diameter 12 mm [45]. Both specimen were irradiated to a final burn up of approximately 80%. Specimens contained uranium with an enrichment of approximately 20 wt% in ²³⁵U .

Fig. 7.1 shows an optical image of one of the specimen (meat layer in the middle and on the top and bottom the cladding layer). The figure shows no break away swelling of the plate. Further the image shows even no interdiffusion between the aluminum cladding and the meat layer.

Since this irradiation test indicates a very good in-pile irradiation behavior, further tests are underway (named RERTR 6 and 7). At the moment the main challenge of this kind of fuel is the fabrication of the U-Mo foil and the welding of the foil with the cladding - both are required on industrial scale [46, 47]. Also a thickness profile of the meat layer (like it is required for the FRM II reactor, see Tab. 1.1.) causes difficulties. Nevertheless, due to the very high uranium density and the promising in-pile behavior, this kind of fuel is of great interest

²The minimum thickness of the coating is the penetration depth of fission fragments, this means that at least 5μm are required.

and further examination will be carried out.

- **U₃Si₂/Al dispersion fuel with higher density**

In case that U-Mo is not available, the performance limits of fuels which are still qualified should be reconsidered. Although only U-Mo/Al dispersion fuel will satisfy our density requirements (as shown in chapter 1), other fuel types would also allow a decrease in the enrichment.

In-pile irradiation tests of U₃Si₂/Al aiming to find the performance limits were carried out in the BR2 reactor [44]. The uranium densities were higher than the maximum qualified uranium density of 4.8gU per cm³, that means 5.1 and 6.1gU per cm³ respectively. The irradiation conditions covered the requirements of the FRM II reactor, that means a heat flux of 520 W per cm², and a cladding surface temperature of 180-200° C. The irradiation program was stopped after the second cycle, based on visual inspection and wet sipping tests of the elements. The plates showed degradations on the aluminum cladding and the release of fission products. The maximum burn up in ²³⁵U was 29% and 25%. PIE showed that the failure of the plates is entirely related to the corrosion of the aluminum cladding, which has caused temperatures to rise well beyond the calculated values. In all stages the fuel grains have retained their integrity and, apart from the formation of an interaction phase with the aluminum matrix, they do not seem to demonstrate deleterious changes in their physical properties. Since this irradiation test does not show the performance limits of U₃Si₂, further tests are necessary.

Each option has the potential of overcoming the drawbacks of U-Mo/Al dispersion fuel, but each option requires further costly and time-consuming in-pile irradiation tests. Therefore it seems to be unrealistic, to expect to obtain a fully qualified fuel, which fulfills the requirements for a conversion of the FRM II reactor before the end of the year 2010. To save time, heavy ion bombardment of specimen should be used for selecting the most promising candidates.

Appendix A

Heavy ion bombarded U_3Si

A study of literature revealed that as early as 1971, Walker bombarded U_3Si with 2 MeV Argon ions in order to simulate fission fragments [35]. He concluded: "Bombardment of U_3Si with 2 MeV argon ions produces a change in the ordered tetragonal cell through a disordered cubic to an amorphous structure ... the amorphous modification, however, transforms to the tetragonal phase at 290°C, this temperature being independent of ion fluence and of some compositional variations ... For bombardments carried out above 250°C the amorphous modification was not detected ...". Furthermore Walker concluded that there is a generally good correlation between observations made on the ion bombarded specimens and those on neutron irradiated material for U_3Si fuel [35].

The published diffraction patterns are shown in Fig. A.1 (diffraction pattern for in-pile irradiated U_3Si fuel for different burn-ups), Fig. A.2 (diffraction pattern of U_3Si fuel and different treatments, including ion bombardments), and Fig. A.3 (diffraction pattern of a heavy ion irradiated specimen and after several annealing steps). The figures show on the one hand the excellent simulation of in-pile irradiation by heavy ion bombardment and on the other hand they show that a transformation from crystalline to amorphous can be suppressed or the crystalline phase can be retained by annealing.

Assuming that this model is also applicable for U-Mo fuel, the effect of the overirradiated specimen could be explained. Since the specimen were very cold when irradiated, and consequently a transition into an amorphous state is more likely.

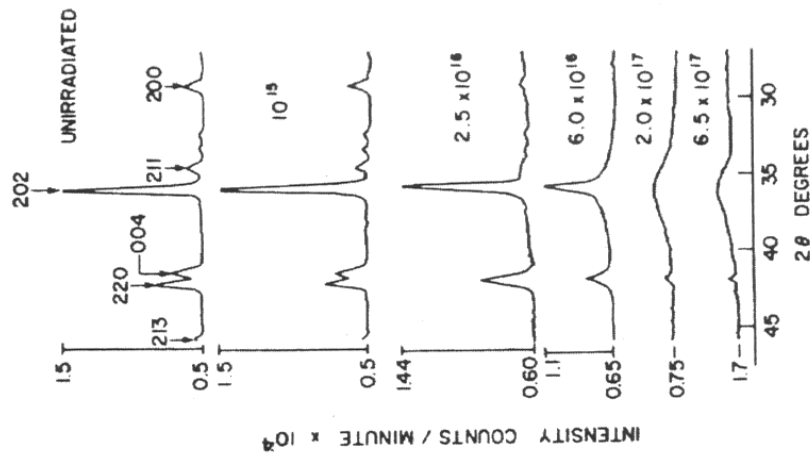


Figure A.1: X-ray diffraction patterns for irradiated U_3Si . Numbers indicate exposure in fission/cm³ - taken from [35]

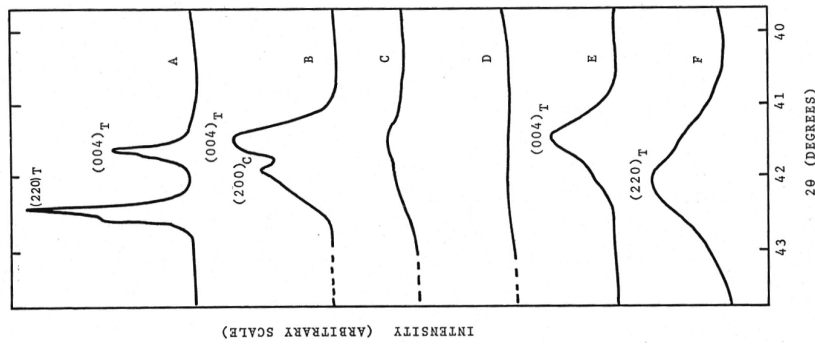


Figure A.2: Appearance of $(220)_T(004)_T$ doublet of U_3Si after various treatments. (A) Annealed and electropolished. (B) Argon-ion bombarded to $2.5 \cdot 10^{13}$ ions/cm², and (C) Argon-ion bombarded to $1 \cdot 10^{14}$ ions/cm², (D) Argon-ion bombarded to $5 \cdot 10^{14}$ ions/cm² (E) Diamond polished. (F) Abreaded by filing. Taken from [35]

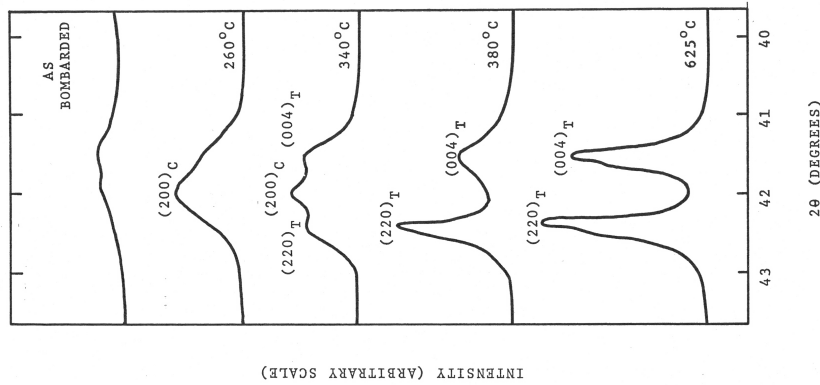


Figure A.3: Appearance of the $(220)_T$ and $(004)_T$ doublet after argon bombardment to a fluence of 10^{14} ions/cm² and after annealing at various temperatures - taken from [35]

Appendix B

Simulations for the FRM II irradiation test

In section 2.3 simulations of U-Mo/Al dispersion fuel, which were carried out with the MAIA-code, were presented. These simulations of full size plates, which are irradiated in the research program for the new fuel of the FRM II, were done before the irradiation was scheduled, and therefore the maximum heat flux was assumed as constant. In the meantime, the real heat flux became available and simulations have been carried out with the real heat flux. These simulations will be presented and discussed in this section.

As mentioned in the chapter 2.3, plates are still under irradiation, therefore the power history is not fixed up to the end of the irradiation. The irradiation can also be stopped before the final burn-up is reached or even prolonged in order to reach a higher burn-up. For instance the irradiation of the plate UMo8001 was stopped after 34 effective full power days (EFPD) due to a handling mistake.

However, the scheduled heat flux and the fission density in the fuel particles for the irradiation test (UMo8001, UMo8002, UMo8501, and 8503) versus the irradiation time in effective full power days (EFPD) are shown in Fig. B.1 and Fig. B.2.

Compared to Fig. 2.8, where a constant heat flux of 300 Watt per cm^2 was assumed, the irradiation requires a bit more time for the same fission density due to a lower average heat flux. The heat flux varies during the irradiation, since the plates are in different position of the reactor core and they have varying adjacent irradiation devices, fuel plates or control rods. Also the reactor power and therefore the neutron flux vary.

The temperature development in the plates (center line temperature) during the irradiation is shown in Fig. B.3. Due to a lower heat flux, the average temperature in the plates is lower, but in the maximum it reaches also up to 160°C . The reason for the temperature increase is - as described in chapter 2.3 - the decrease of the thermal conductivity of the meat.

Fig. B.4 shows the swelling of the plates versus EFPD. One can see that the swelling starts at different burn-ups (due to different as-fabricated porosities), but with almost the same slope. However, first swelling measurements indicated, that the swelling starts a bit earlier than in the simulation, but with the same slope. Uncertainties or local variation in the as-fabricated porosity are possible reasons.

In conclusion: For the simulation and their results, there is no significant difference for a constant or the real heat flux, but knowledge about the as-fabricated porosity is important for the start of the plate swelling. For further discussion of the simulation, at least the thickness measurement has to be awaited.

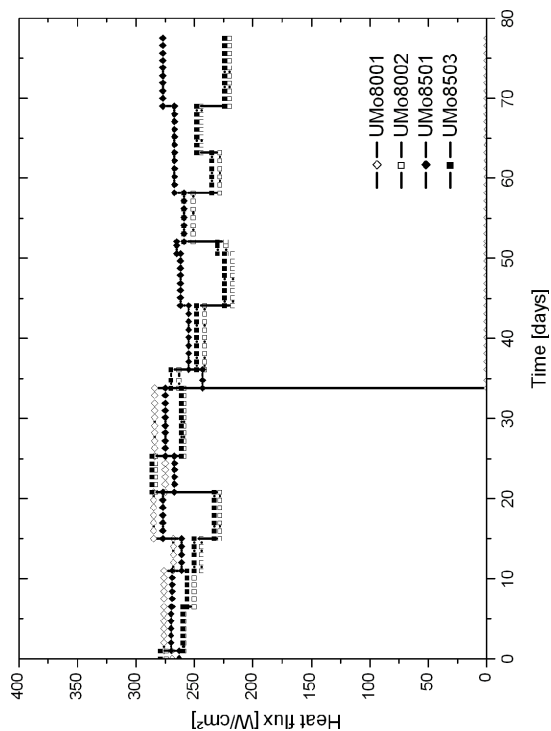


Figure B.1: Power history of the fuel plates

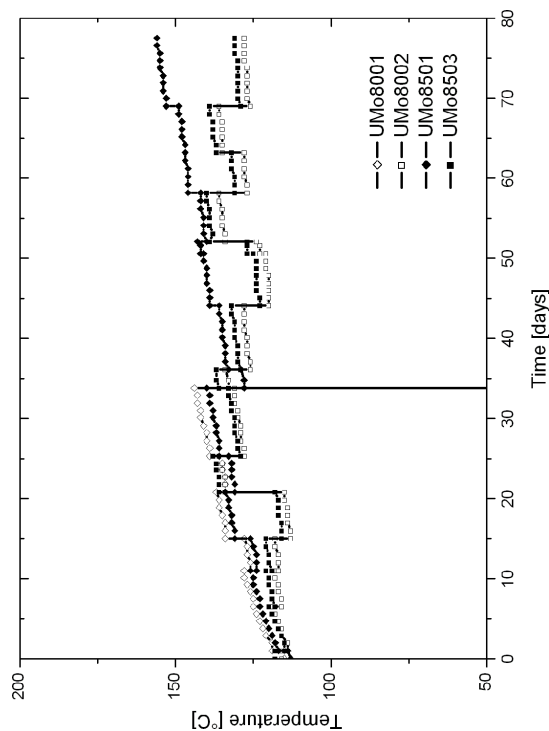


Figure B.3: Calculated center line temperature

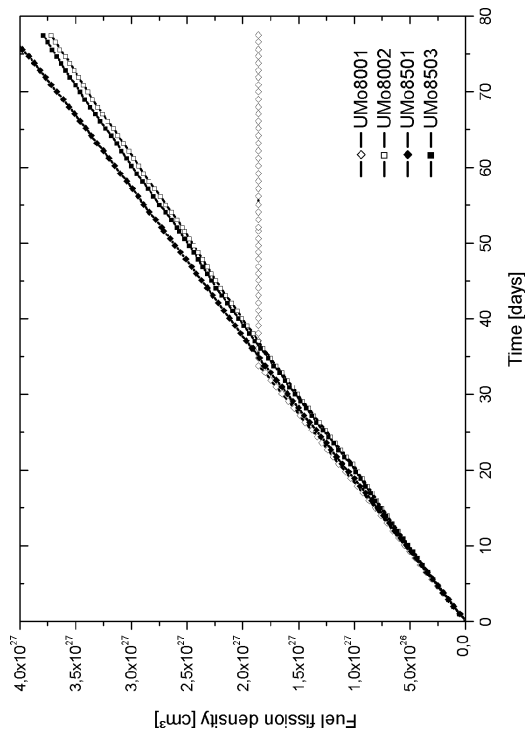


Figure B.2: Fuel fission density versus EFPD

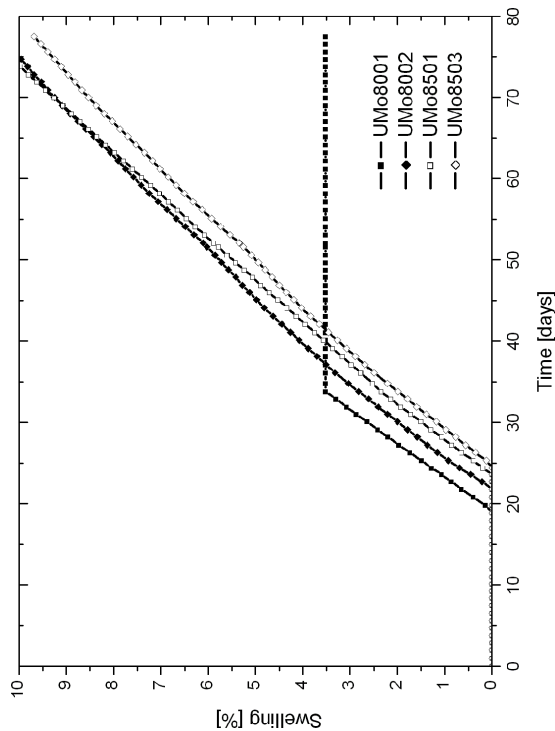


Figure B.4: Calculated swelling

Appendix C

Maxim data for the U-10wt%Mo/Al specimen

This chapter relates to section 4.3.2. Here the MAXIM data for the U-10wt%Mo/Al specimen will be presented.

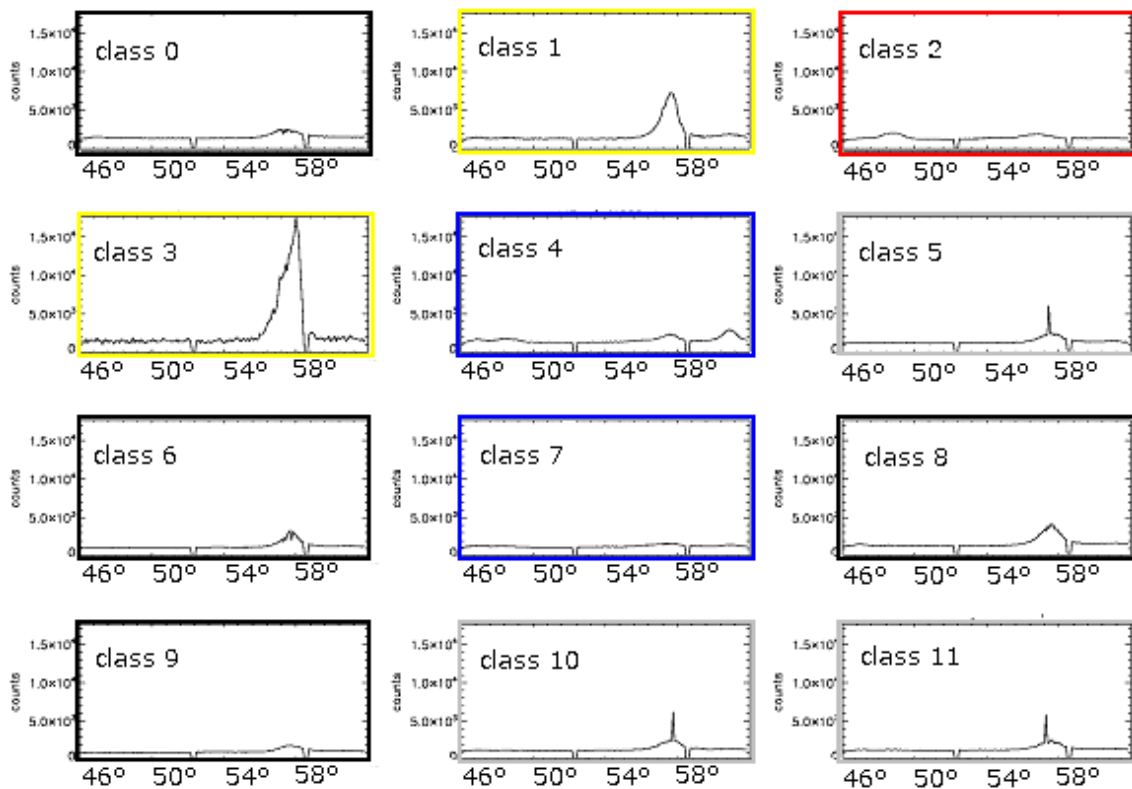


Figure C.1: All twelve spectra from classification of the MAXIM-measurement for the U-10wt%Mo/Al specimen, each spectrum represents one class in Fig. C.1

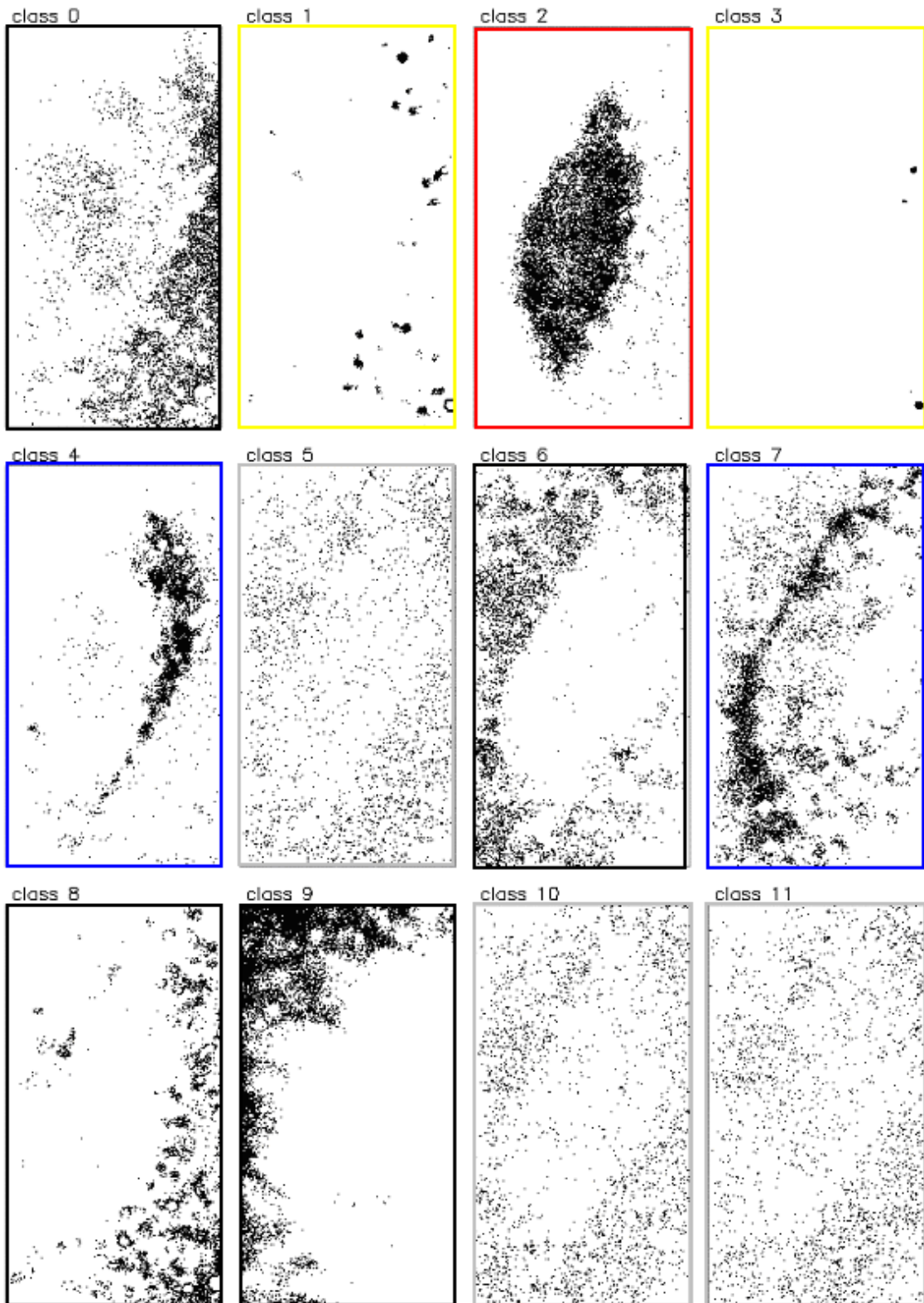


Figure C.2: Two dimensional maps of classes of specimen U-10wt%Mo/Al.

Acknowledgment

This thesis would have been impossible without the support of many people, most of whom are good friends now. Therefore I would like to thank everybody who supported this work. My special thank goes to:

- First of all I would like to thank my adviser **Prof. Dr. P. Böni**, who constantly helped me ... and finally he convinced me that physics is great! I fully agree with you! Thank you for the fruitful discussions!
- Perhaps, even more thanks should go to **Prof. Dr. W. Petry**, since he supported me from the beginning and financed all my ideas. Surprisingly he always had time for discussion - although he was always busy because of his job - However, he showed me several times why he is the scientific director of the FRM II! Thank you very much!
- Of course I have to thank the father of the FRM II reactor - **Prof. Dr. K. Böning**. Presumably due to his retirement he always had time to discuss and to answer my questions and to guide me in many ways. Thanks a million!
- **Dr. R. Grossmann** - he made all the handling (import and export) and preparation of uranium possible. Many people warned me that any business with uranium would be impossible in Germany - he demonstrated the opposite!
- **The team of the accelerator** - This huge family showed me team work at its best and I am reluctant to mention single persons. Nevertheless, I would like to name the people who introduced me to this special team, were always interested in my progress and helped immediately: **Prof. Dr. G. Dollinger** and **Dr. A. Bergmeier**. However, I would like to point out that only the team of the accelerator made successful irradiations possible.
- **Dr. J. Schneider** - In his friendly way he introduced me to diffractometers and encouraged me in this field.
- **Dr. C. Morkel** - for the professional introduction into the measurement of thermal properties and the bureaucracy with EURATOM.
- **Dr. A. Röhrmoser** - Indeed, I learned a lot from you. I am glad to have known you.

- Hard working students, who helped me a lot: **Chr. Bogenberger, R. Härtle, and W. Schnell**
- **R. Jungwirth** - for measuring thermal properties of fresh and heavy ion bombarded U-Mo/Al dispersion fuel
- **Prof. Dr. C. Pfeiderer** - he advised and motivated R. Jungwirth (and me) always and made the measurements of thermal properties possible - thank you very much!
- **W. Schmid and D. Hohl** - for the realisation of the perfect device
- **The French U-Mo group** - Our many meetings lead to particularly friendly and fruitful discussion. Discussion with **C. Jarousse** and **J. Noirot** were specially successful!
- **The RERTR-team** - in spite of many political differences, they introduced me in an absolutely friendly manner into the U-Mo fuel and provided me with much data. I would especially like to thank **G. Hofman, A. Travelli and N. Hannan**.
- **D. Moses** - he showed me the history of many fuel types and provided me with a general overview of the nuclear fuel business.
- **FRM II Workshop (especially Mr. Herzog and Mr. Tessaro)** - every request were completed in time! Many thanks!
- **A. Lümke** - for the help at the SEM,
- **V. Marelle** - for the help with all the MAIA-simulations
- the “**Kristalllabor**” at the University of Technology München - for all the technical aid during polishing of the specimen.
- The administrators of the computer network (**J. Pulz and C. Herbster**)
- M. O’Leary-Hunter für die kompetente, schnelle und trotzdem liebevolle Englisch-Korrektur dieser Arbeit!
- **Rebekka Vollmer** - for being my girlfriend and bearing with me!
- All my relatives - **especially my parents, my sister Conny and my brother Tony!**
- and last but not least my friends: **Dr. N. Wiele, Dr. T. Asthalter, Dr. M. Goldammer & Dipl. soz. C. Bieber!**

Own publications and patent

- **Heavy ion irradiation of U-Mo/Al dispersion fuel**
N. Wieschalla, K. Böning, W. Petry, A. Röhrmoser, P. Böni, A. Bergmaier, G. Dollinger, R. Grossmann, J. Schneider
27th RERTR - Reduced Enrichment for Research and Test Reactors (RERTR) Program, Boston USA 2005
- **Heavy ion irradiation of U-Mo/Al dispersion fuel**
N. Wieschalla, K. Böning, W. Petry, A. Röhrmoser, P. Böni, A. Bergmaier, G. Dollinger, R. Grossmann, J. Schneider
Journal of nuclear materials
Volume 357, Issues 1-3, 15 October 2006, Pages 191-197
2006
- **Heavy ion irradiation as a method to discriminate research reactor fuels**
H. Palancher, P. Martin, C. Sabathier, S. Dubois, C. Valot, N. Wieschalla, W. Petry, A. Röhrmoser, C. Jarousse, M. Grasse, R. Tucoulou
10th RRFM - International Topical Meeting on Research Reactor Fuel Management, Sofia, Bulgaria 2006
- **Reduced Enrichment Program for the FRM II**
A. Röhrmoser, W. Petry, K. Böning, N. Wieschalla
Reduced Enrichment for Research and Test Reactors - International Conference, Vienna, Austria, 2004
- **Increasing Depletion**
A. Röhrmoser, W. Petry, K. Böning, N. Wieschalla
Nuclear Engineering - International Magazine
December 2004
- **patent**
Deutschen Patentamt
AZ: 10 2005 055 692.2
issued 23.11.2005

- **Testing the shielding of the monochromator of Mira by Monte Carlo Method**
Nico Wieschalla, Florian Grünauer, Robert Georgii
TU München, Department of Physics, Institute E21
annual report 2003
- **Minimization of the background radiation of a sample environment**
Nico Wieschalla, Florian Grünauer, Jürgen Peters
TU München, Department of Physics, Institute E21
annual report 2003
- **New high density fuel for the FRM II**
A. Röhrmoser, W. Petry, K. Böning, N. Wieschalla
TU München, Department of Physics, Institute E21
annual report 2004
- **Heavy Ion Irradiation of U-Mo/Al Dispersion fuel**
N. Wieschalla A. Bergmaier, P. Böni, K. Böning, W. Petry, A. Röhrmoser
TU München, Department of Physics, Institute E21
annual report 2005
- **Heavy Ion Irradiation of U-Mo/Al Dispersion fuel**
N. Wieschalla A. Bergmaier, P. Böni, K. Böning, W. Petry, A. Röhrmoser
Munich Tandem accelerator
annual report 2005

Bibliography

- [1] **J. Matos**
private communication
Reduced Enrichment for Research and Test Reactors-Group
2004
- [2] **R.W. Cahn, P. Haasen, E.J. Kramer**
Materials Science and Technology, Volume 10A
VCH Verlagsgesellschaft mbH; Germany
1994
- [3] **R.W. Cahn, P. Haasen, E.J. Kramer**
Materials Science and Technology, Volume 10B
VCH Verlagsgesellschaft mbH; Germany
1994
- [4] **Homepage of the Reduced Enrichment for Research and Test Reactors - Team**
www.rertr.anl.gov
- [5] **Homepage of "Forschungsneutronenquelle Heinz Maier-Leibnitz" (FRM II)**
www.frm2.tum.de
- [6] **Homepage of Areva NP**
www.framatome-anp.com
- [7] **Homepage of the THTR-300 reactor**
www.thtr.de/
- [8] **Wikipedia - on-line free encyclopedia**
<http://en.wikipedia.org>
- [9] **K. Böning, W. Petry, A. Röhrmoser, Chr. Morkel**
Conversion of the FRM II
Transaction of the RRFM 2004, Munich, Germany
2004
- [10] **W. Petry**
Neutron Research and Application at FRM II

- Transaction of the RRFM 2004, Munich, Germany
2004
- [11] **A. Röhrmoser, W. Petry, K. Böning, N. Wieschalla**
Reduced Enrichment Program for the FRM II
Reduced Enrichment for Research and Test Reactors - International Conference, Vienna, Austria
2004
- [12] **A. Röhrmoser, W. Petry, K. Böning, N. Wieschalla**
Increasing Depletion
Nuclear Engineering - International Magazine
December 2004
- [13] **P. Lemoine, J.L. Snelgrove, N. Arkhangelsky, L. Alvarez**
UMo Dispersion fuel results and status of qualification programs
8th RRFM - International Topical Meeting on Research Reactor Fuel Management, München, Germany
2004
- [14] **J.L. Snelgrove, G.L. Hofman, C.L. Trybus and T.C. Wiencek**
Development of very-high-density fuels by the RERTR Program
19th RERTR - Reduced Enrichment for Research and Test Reactors (RERTR) Program; Seoul
1996
- [15] **G. L. Hofman, M. K. Meyer, J. L. Snelgrove, M. L. Dietz, R. V. Strain, and K-H. Kim**
Initial assessment of radiation behavior of very-high-density low-enriched-uranium fuels
International Meeting on Reduced Enrichment for Research and Test Reactors (RERTR) Budapest, Hungary
1999
- [16] **Homepage of: Research Reactor Fuel Management**
www.euronuclear.org/meetings/rrfm2006/index.htm
- [17] **T.B. Massalski**
Binary Alloy Phase Diagrams, Second Edition
ASM Internat.
- [18] **D.R. Olander**
Fundamental Aspects of Nuclear Reactor Fuel Elements
National Technical Information Service
U.S. Department of Commerce
Springfield, Virginia 22161
1976

- [19] **E. Fermi**
Nuclear Physics
Midway Reprint
Revised Edition: 1950
- [20] **D. Emendörfer, K.H. Höcker**
Theorie der Kernreaktoren
Wissenschaftsverlag Berlin
ISBN 3-411-01599-3
1982
- [21] **D. Smidt**
Reaktortechnik I/II
G. Braun-Verlag, Karlsruhe, Germany
1976
- [22] **B. Povh, K. Rith, C. Scholz, F. Zetsche**
Teilchen und Kerne
Springer-Verlag, Germany
1994
- [23] **N. Wieschalla**
Optimierung von Messinstrumenten mit der Monte Carlo Methode am FRM II
Diplomarbeit
TU München - Physik Department - Lehrstuhl E21
2003
- [24] **F. Staufenbiel**
Elektronentemperaturen im Zentrum von Ionenspuren in Metallen
Doktorarbeit
TU Berlin - Fakultät II - Mathematik und Naturwissenschaften
2004
- [25] **Z.G. Wang, Ch. Dufour, E. Paumier, M. Toulemonde**
J. Phys.: Condensed Matter
6 (1994) 6733-6750
1994
- [26] **S.T. Konobeevsky, N.F. Pravdyk, V.I. Kutaitsev**
Effect of Irradiation on Structure and Properties of Fissionable Materials
Proceedings of the first United Nations International Conference on the Peaceful
Uses of Atomic Energy, Volume 7
Geneva, Switzerland
1955
- [27] **J.F. Ziegler, J.P. Biersack**
SRIM - the stopping and range of ions in matter

computer code
version srin-2003.26

- [28] **V. Marelle, F.Huet, P. Lemoine**
Thermo-mechanical modeling of U-Mo fuels with MAIA
Transaction of the RRFM 2004, Munich, Germany
2004
- [29] **G.L. Hofman, M.R. Finlay, Y.S. Kim**
Post-irradiation analysis of Low Enriched U-Mo/Al Dispersion Fuel Miniplate Tests, RERTR 4 & 5
RERTR-Meeting, Vienna
2004
- [30] **M.J. Berger, J.H. Hubbell, S.M. Seltzer, J. Chang, J.S. Coursey, R. Sukumar, and D.S. Zucker**
XCOM
Photon Cross Sections Database
2005
- [31] **M. Mirandou, S. Aricó, L. Gribaudo, S. Balart**
Out of pile diffusion studies between U-7wt%Mo and Al-Si alloys
27th RERTR - Reduced Enrichment for Research and Test Reactors (RERTR) Program; Boston
2005
- [32] **J.M. Park, H.J. Ryu, G.G.Lee, H.S.Kim, Y.S. Kim, C.K. Kim**
Phase stability and diffusion characteristics of U-Mo-X (X=Si, Al, Zr) Alloys
27th RERTR - Reduced Enrichment for Research and Test Reactors (RERTR) Program; Boston
2005
- [33] **C.K. Gupta**
Materials in nuclear energy applications -volume 1
CRC Press Inc.
1989
- [34] **C.K. Gupta**
Materials in nuclear energy applications -volume 2
CRC Press Inc.
1989
- [35] **D.G. Walker, P.A. Morel**
X-ray diffraction studies of ion-bombarded U₃Si
Journal of nuclear materials 39, p. 49-58
1971

- [36] **M.D. Hou, S. Klaumünzer**
Heavy ion-induced deformation of radiation-amorphized U_3Si
Nuclear Instruments and Methods in Physics Research B 209, p. 149-153
2003
- [37] **T. Wroblewski et al.**
Experimental station G3 at DESY
Rev. Sci. Instrumentation 66, 3560
1995
- [38] **T. Wroblewski et al.**
Experimental station G3 at DESY
Nucl. Instrumentation Methods, A428, 570
1999
- [39] **Ki Hwan Kim, Don Bae Lee, Chnag Kyu Kim, Il Jyun Kuk, Gerard L. Hofman**
Development of high-loading U-Mo alloy fuel by centrifugal atomization
27th RERTR - Reduced Enrichment for Research and Test Reactors (RERTR)
Program; Seoul, Korea
1996
- [40] **M. I. Mirandou, S. N. Balart, M. Ortiz, M. S. Granovsky**
Reaction layer in U- 7wt%Mo /Al diffusion couples
25th RERTR - Reduced Enrichment for Research and Test Reactors (RERTR)
Program, Chicago USA
2003
- [41] **G.L. Hofman, Y.S. Kim, M.R. Finlay, J.L. Snelgrove, S.L. Hayes, M.K. Meyer, and C.R. Clark**
Recent observations at the postirradiation examination of low-enriched U-Mo miniplates irradiated to high burnup
25th RERTR - Reduced Enrichment for Research and Test Reactors (RERTR)
Program, Chicago USA
2003
- [42] **Mirandou M., Granovsky M., Ortiz M., Balart S., Aricó S. and Gribaud L.**
Reaction layer between U-7wt%Mo and Al alloys in chemical diffusion couples.
25th RERTR - Reduced Enrichment for Research and Test Reactors (RERTR)
Program, Vienna, Austria
2004
- [43] **S. Dubois, F. Mazaudier, J.P. Pron, P. Martin, J.C. Dumas, F. Huet, H. Noël**
Out of pile Frensch research program on the UMo/Al system: first results

- 9th International Topical meeting on research reactor fuel management, Budapest, Hungary
2005
- [44] **S. van den Berghe, A. Leenaers, E. Koonen, P. Jacquet, L. Sannen, C. Jarousse, B. Guigon, A. Ballagny**
Microstructure of U_3Si_2 fuel plates submitted to a high heat flux
8th RRFM - International Topical Meeting on Research Reactor Fuel Management, München, Germany
2003
- [45] **S. L. Hayes, C. R. Clark, J. R. Stuart and M. K. Meyer T. C. Wiencek, J. L. Snelgrove and G. L. Hofman**
Irradiation testing of intermediate and high-density U-Mo alloy dispersion fuels to high burnup
22nd RERTR - Reduced Enrichment for Research and Test Reactors (RERTR) Program, Las Vegas USA
2000
- [46] **C.R. Clark, N.P. Hallinan, J.F. Jue, D.D. Keiser, J.M. Weight**
Monolithic fuel fabrication process development
10th RRFM - International Topical Meeting on Research Reactor Fuel Management, Sofia, Bulgaria
2006
- [47] **C. Jarousse, P.Lemoine, W. Petry**
Monolithic UMo full size prototypes plates manufacturing development status as of April 2006
10th RRFM - International Topical Meeting on Research Reactor Fuel Management, Sofia, Bulgaria
2006
- [48] **H. Palancher, P. Martin, C. Sabathier, S. Dubois, C. Valot, N. Wiseschalla, W. Petry, A. Röhrmoser, C. Jarousse, M. Grasse, R. Tucoulou**
Heavy ion irradiation as a method to discriminate research reactor fuels
10th RRFM - International Topical Meeting on Research Reactor Fuel Management, Sofia, Bulgaria
2006
- [49] **K. Schreckenbach**
Reaktorphysik und neue Konzepte in der Kerntechnik
Lecture notes
2005/2006
- [50] **D.F. Sears et al.**
Development, Irradiation Testing and PIE of U-Mo Fuel at AECL

Reduced Enrichment for Research and Test Reactors - International Conference, Vienna, Austria
2004

- [51] **A. Leenaers et al.**
Post Irradiation Examination of Uranium -7wt% Molybdenum Atomized Dispersion Fuel
Journal of nuclear materials, 355 (2004), 39-47
2004
- [52] **F. Huet et al.**
Post Irradiation Examination on U-Mo Full size plates -IRIS2 Experiment
9th International Topical meeting on research reactor fuel management, Budapest, Hungary
2005
- [53] **K.T. Conlon, D.F. Sears**
Neutron powder diffraction of irradiated low-enriched uranium-molybdenum dispersion fuel
10th RRFM - International Topical Meeting on Research Reactor Fuel Management, Sofia, Bulgaria
2006
- [54] **P. Sacristan**
private communication
CEA-Saclay, Paris, France
2004
- [55] **Hyperphysics**
<http://hyperphysics.phy-astr.gsu.edu/hbase/nucene/fisfrag.html>
- [56] **Homepage of the Munich Tandem Accelerator**
www.bl.physik.uni-muenchen.de
- [57] **Homepage of DESY**
<http://www.desy.de/html/home/index.html>
- [58] **Homepage of the experimental station G3 at Hasylab**
www-hasylab.desy.de/facility/experimental_stations/G3/G3.htm
- [59] **Webelements**
www.webelements.com